Torque Magnetometry and Transport Study on Topological Superconductors and Semimetals

by

Tomoya Asaba

A dissertation submitted in partial fulfillment
of the requirements for the degree of
Doctor of Philosophy
(Physics)
in The University of Michigan
2018

Doctoral Committee:

Associate Professor Lu Li, Chair
Professor Cagliyan Kurdak
Professor Zetian Mi
Associate Professor Vanessa Sih
Associate Professor Kai Sun

tasaba@umich.edu
ORCID iD: 0000-0003-4631-9589

ACKNOWLEDGEMENTS

First and foremost, I am grateful to my advisor Professor Lu Li for his excellent supervision. In graduate life, I learned physics and research, including how to write a paper and proposal, how to collaborate and discuss with other groups, and how to manage the lab. I also learned how to survive in the US from him, such as dealing with VISA, expressing my opinion and speaking fluent English. Not only he is a fantastic physicist and mentor, but he is also very exemplary in two ways. Firstly, he is very sociable. I was genuinely impressed by the number of his friends in this field and how active he is during conferences. This lead me to attend more than four summer schools to make a social connection to follow his path. Also, he is generous, patient and encouraging. Whenever the experimental result was not what I expected, he explained the result by fancy physics, encouraging me to refine and continue the experiment. Most of the interesting findings in this thesis were obtained this way. It is indeed my honor to be mentored by him.

I would like to thank Professor Yew San Hor, Zetian Mi, Chang-Beom Eom, Young Lee, David Mandrus and Dr. Jiaqiang Yan for providing high-quality samples, and Professor Kai Sun, Liang Fu and Yi Li for theoretical support.

I am grateful to my dissertation committee, Professor Lu Li, Zetian Mi, Kai Sun, Vanessa Sih, and Cagliyan Kurdak.

I appreciate the former postdoc of our lab, Dr. Gang Li for teaching everything. As he is a skilled experimentalist, I learned most of the experimental tools and data analyzing techniques from him. Moreover, the most important thing I learned from

him is how to enjoy my life. In particular, it was him who told me how beautiful the mountains are in the US, leading me to work in Los Alamos, a beautiful mountain area as well as a great research place.

I also appreciate the current postdoc of our lab, Dr. Ziji Xiang for his physical insight. Whenever I ask questions about physics, he has an answer or opinion that I greatly benefited from. Furthermore, his strategy of career path greatly helped me decide the next step of my career I choose.

My research was strongly supported by the fantastic lab members. In particular, Benjamin Lawson was my not only a great colleague but also as a close friend. He taught me most of the fascinating US cultures and styles, and also I learned from him how to be active, positive and sociable. I also would like to thank the other lab members, Colin Tinsman, Fan Yu and Lu Chen for not only helpful supports and discussions but also private advice. Although worked together for just half a year, I also greatly appreciate Peng Cai, who was my first friend in the US and introduced Ben to me. Without him, I could not have had any friends during graduate life.

Outside the lab, I also learned a lot of physics and techniques from Dr. John Singleton, Professor Yuji Matsuda, Dr. Ju-Hyun Park, Dr. Yun Suk Eo and Dr. Tian Liang. I would also appreciate Dr. Singleton and Professor Matsuda for the research collaboration.

I greatly appreciate the Nakajima Foundation for the prestigious scholarship, generously covering my tuition and stipend for five years. Without this scholarship, I could not have finished this long path in Michigan.

Lastly, I would like to thank my family for love and any support during graduate life, which prevented me from feeling alone and frustrated.

TABLE OF CONTENTS

LIST OF FIGURES

Figure

LIST OF APPENDICES

Appendix

LIST OF ABBREVIATIONS

NMR Nuclear magnetic resonance

ARPES angle-resolved photoemission spectroscopy

TI topological insulator

TSC topological superconductor

2D two-dimensional

3D three-dimensional

STM scanning tunneling microscopy

SdH Shubnikov de Haas

MBE molecular beam epitaxy

TRI time-reversal-invariant

dHvA de Haas-van Alphen

ZBCP zero-bias conductance peak

RSB rotational symmetry breaking

TEM transmission electron microscopy

SPM scanning probe microscopy

XPS X-ray photoelectron spectroscopy

EDX energy dispersive X-ray spectroscopy

MR magnetoresistance

WAL weak anti-localization

TMD transition metal dichalcogenides

SOC spin-orbit coupling

FFT Fast Fourier transform

PDO proximity detector oscillator

ABSTRACT

Recently, the topological features of materials have been intensively focused on not only due to its fundamental physical interest, but also its application to dissipationless devices and quantum computing. In this study, I investigated three materials with different topological classes: $Nb_xBi_2Se_3$, thin film WTe_2 and $LaNiO_3$ grown on $LaAlO_3$.

$Nb_xBi_2Se_3$ is a candidate of topological superconductors, which may host Majorana fermions that could be used for topological quantum computing. In the superconducting state of $Nb_xBi_2Se_3$, by torque magnetometry technique, I observed the in-plane angular dependence of susceptibility and supercurrent shows the two-fold symmetry although the crystal structure is trigonal. This in-plane rotational symmetry breaking is called the nematic superconducting state. On the other hand, in the normal state, the angular dependence of susceptibility follows six-fold symmetry, indicating that the nematicity occurs only in the superconducting state. However, de Haas-van Alphen study shows that the in-plane Fermi surface is also anisotropic. This would nail down the origin of the nematic order.

Next, the bulk WTe_2 is a type-II Weyl semimetal. However, when a thin film of WTe_2 is grown on a sapphire substrate, it becomes superconducting. Moreover, there are a few exotic superconducting features in this system. First, the in-plane upper critical field H_{c2} is more than 10 times larger than the Pauli limit H_p, indicating the

Ising superconductivity in this system. Furthermore, the critical temperature T_c is enhanced by the in-plane magnetic field at both around $T = T_c$ and $T = 0$. This result may be associated with the unique T_d crystal structure of this system, which also relates to the Weyl nature.

Lastly, when $LaNiO_3$ thin films are grown on $LaAlO_3$ (111), the emergence of Dirac physics, as well as the multiferroic feature, is predicted due to the buckled honeycomb structure in (111) plane. We first observed the ferromagnetic state as predicted by many groups. This result is important not only because it gives further guidance to improve the theoretical modeling, but also because the ferromagnetic state can be coupled to the ferroelectricity for potential spintronics applications. Moreover, our results are consistent with the existence of a gapped Dirac point predicted by the theory. These results would be a significant step forward in the realization of a strongly correlated topological phase by geometrical engineering of buckled honeycomb lattice.

These results will help further understand the exotic features of topological materials. In particular, the combination of topology and correlation or superconductivity is quite a new field. The observation of nematic superconductivity, field-enhanced T_c and magnetic Dirac physics would be a hallmark for this field.

CHAPTER I

Introduction to topological materials

In mathematics, two shapes have the same topological class if they can be deformed continuously into each other. In quantum condensed matter physics, when the wavefunction cannot be adiabatically connected to the atomic limit, the material is called topological, or topologically non-trivial. After the theoretical discovery of topological insulator, topological materials have been focused on very intensively. They can be classified using an integer number, which is topological invariant named Chern number, as explained in detail in this chapter.

In this study, I focused on four types of important topological classes: topological insulators, topological superconductors, Weyl semimetals and Dirac semimetals. Thus, I described the details of these topological classes in each section of this chapter.

1.1 Topological insulators

1.1.1 Overview

In physics, non-trivial topological nature was recognized in quantum Hall systems [1] and superfluid helium 3 [2] since 1980s. However, the study of topological materials become explosively popular after the theoretical discovery of the two-dimensional (2D)topological insulator (TI), or quantum spin Hall insulator in 2005

[3], then followed by three-dimensional (3D) extension [4, 5]. They are characterized by the topological invariant, or Z_2 index.

The significance of TIs is the existence of gapless edge or surface state. For example, while the bulk of 3D TI is an insulator with a gap between the valence and conduction band, there is a gapless surface state which is conductive (in other words, metallic) and its conductivity is quantized. Furthermore, the energy dispersion of the surface state is cone-like, which cross-section linear instead of the classical parabolic bands. It is called the Dirac cone, and the crossing point of the cone is called Dirac point. Fig. 1.1 shows the first direct visualization of Dirac dispersion from the surface state in prototypical TI Bi_2Te_3 [6].

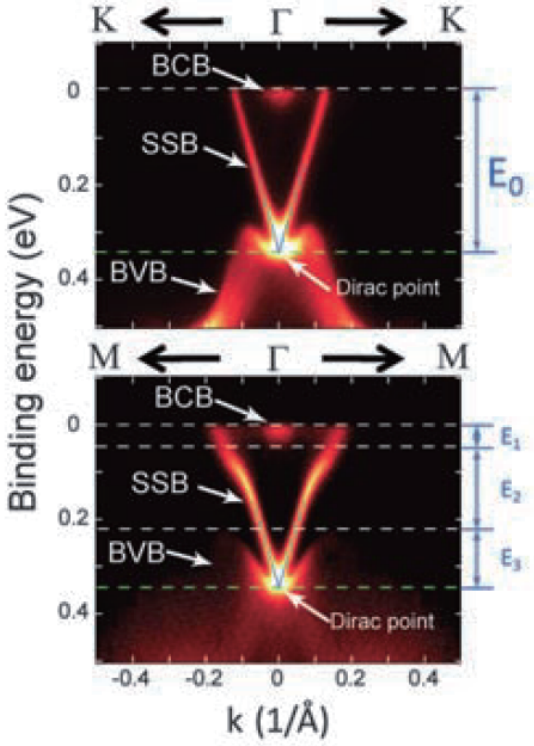

Figure 1.1: **Zero-bias conductance peak measured by point contact spectroscopy in Cu-doped Bi_2Se_3.** (a) Point-contact spectrum at different temperatures. (b) Narrower range of (a). (c) The magnetic field dependence of point-contact spectrum at T = 0.35 K. Adapted from ref.[6].

The first experimental realization of two-dimensional TIs was discovered in the

HgTe/CdTe quantum well structure in 2007[7], followed by InAs/GaSb/AlSb quantum well [8]. For three-dimensional TIs, the first experimental observation was confirmed in $Bi_{1-x}Sb_x$ system in 2008[9].

1.1.2 Dirac equation in the continuous limit

As explained later, topological insulators, topological superconductors, Dirac semimetals and Weyl semimetals are all related to the Dirac equation. Thus, the Dirac equation would be a good starting point.

In the following few sections, I briefly walk through the explanation of topological materials based on modified Dirac equation in Ref. [10].

We start from the Schroedinger equation

$$-\frac{\hbar^2}{2m}\nabla^2\Psi = i\hbar\frac{\partial}{\partial t}\Psi. \tag{1.1}$$

This is obtained by non-relativistic kinetic energy $E^2 = P^2/2m$. In a relativistic generalization, the energy and momentum relation is given by

$$E^2 = m^2c^4 + p^2c^2. \tag{1.2}$$

Combining Eq. (1.1) and Eq. (1.2), we obtain the Klein-Gordon equation

$$\left(-\frac{1}{c^2}\frac{\partial^2}{\partial t^2} + \nabla^2\right)\Psi = \frac{m^2c^2}{\hbar}\Psi. \tag{1.3}$$

Dirac thought that Eq.(1.3) could be further "factorized" by the equation

$$i\hbar\frac{\partial}{\partial t}\Psi = \left[-i\hbar c\left(\alpha_x\frac{\partial}{\partial x} + \alpha_y\frac{\partial}{\partial y} + \alpha_z\frac{\partial}{\partial z}\right) + \beta mc^2\right]\Psi = \left(c\alpha\cdot p + \beta mc^2\right)\Psi. \tag{1.4}$$

Eq. (1.4) is called Dirac equation. Taking the square of both sides of Eq. (1.4)

and comparing with Eq. (1.3), we obtain

$$\alpha_i^2 = \beta^2 = 1 \tag{1.5}$$

$$\alpha_i \alpha_j = -\alpha_j \alpha_i \tag{1.6}$$

$$\alpha_i \beta = -\beta \alpha_i \tag{1.7}$$

where α and β are called Dirac matrices. Simple complex numbers cannot satisfy the condition above. Thus, α and β need to be in the matrix form. For one and two dimensions, the Pauli matrices satisfy the condition above,

$$\sigma_x = \begin{pmatrix} 0 & 1 \\ 1 & 0 \end{pmatrix}, \sigma_y = \begin{pmatrix} 0 & -i \\ i & 0 \end{pmatrix}, \sigma_z = \begin{pmatrix} 1 & 0 \\ 0 & -1 \end{pmatrix}. \tag{1.8}$$

In three dimensions, Dirac matrices can be represented by

$$\alpha_i = \begin{pmatrix} 0 & \sigma_i \\ \sigma_i & 0 \end{pmatrix}, \beta = \begin{pmatrix} \sigma_0 & 0 \\ 0 & -\sigma_0 \end{pmatrix} \tag{1.9}$$

where σ_0 is an identity matrix in two dimensions.

In one dimension, Dirac equation (1.4) becomes

$$E\Psi = \left(-ic\hbar\partial_x \sigma_x + mc^2 \sigma_z\right) \Psi. \tag{1.10}$$

by choosing $\alpha_1 = \sigma_x$ and $\beta = \sigma_z$. This equation can be solved by assuming that the wave function Ψ has the form

$$\Psi = \begin{pmatrix} \psi_1 \\ \psi_2 \end{pmatrix} e^{-\lambda x}. \tag{1.11}$$

Solving the secular equation, the energy eigenvalue can be obtained.

However, this equation is topologically trivial and cannot describe the physics in topological materials. In order to apply it to the solid state physics, we introduce an additional quadratic term $-Bp^2$ to Eq. (1.4)[10],

$$\mathcal{H} = v\alpha \cdot p + \left(mv^2 - Bp^2\right)\beta. \tag{1.12}$$

Here c is also replaced by v. Assume that the semi-infinite material with the boundary at x=0 (e.g., chain for 1D, plane for 2D).

In one dimension, similar to Eq. (1.10), the equation is given by [10]

$$E\Psi = \left[-iv\hbar\partial_x\sigma_x + \left(mv^2 + B\hbar^2\partial_x^2\right)\sigma_z\right]\Psi. \tag{1.13}$$

Since a Dirac cone has zero energy solution, we focus on the zero energy mode. Then, from Eq. (1.13) we have

$$iv\hbar\partial_x\sigma_x\Psi = \left(mv^2 + B\hbar^2\partial_x^2\right)\sigma_z\Psi. \tag{1.14}$$

Multiplying σ_x from the left hand side, Eq. 1.14 becomes

$$\hbar\partial_x\Psi = -\frac{1}{v\hbar}\left(mv^2 + B\hbar^2\partial_x^2\right)\sigma_y\Psi. \tag{1.15}$$

Here, Ψ has to be an eigen fuction of σ_y, $\sigma_y\Psi = \eta\Psi$ where $\eta = \pm 1$. Thus, assuming $\Psi \propto e^{-\lambda x}$, we obtain the secular equation

$$B\hbar^2\lambda^2 - \eta v\hbar\lambda + mv^2 = 0. \tag{1.16}$$

The solution is

$$\lambda_\pm = \frac{v\left(\eta \pm \sqrt{1 - 4mB}\right)}{2B\hbar}. \tag{1.17}$$

Since the boundary condition for the wave function is given by

$$\Psi(x=0) = \Psi(x=\infty) = 0, \tag{1.18}$$

$\lambda_\pm$ has to be positive. Therefore, $\eta = sgn(B)$ (sgn is a sign function) and $mB > 0$ is required. In this condition, the wave function for the zero energy state is given by

$$\Psi(x) = C \begin{pmatrix} sgn(B) \\ i \end{pmatrix} \left(e^{-\lambda_+ x} - e^{-\lambda_- x} \right). \tag{1.19}$$

Eq.(1.19) can be also represented by the four-component as

$$\Psi(x)_1 = C \begin{pmatrix} sgn(B) \\ 0 \\ 0 \\ i \end{pmatrix} \left(e^{-\lambda_+ x} - e^{-\lambda_- x} \right) \tag{1.20}$$

and

$$\Psi(x)_2 = C \begin{pmatrix} 0 \\ sgn(B) \\ i \\ 0 \end{pmatrix} \left(e^{-\lambda_+ x} - e^{-\lambda_- x} \right). \tag{1.21}$$

In two dimension, modified Dirac Hamiltonian is given by [10]

$$\begin{aligned} \mathcal{H} = & \quad v\alpha_x p_x + v\alpha_y p_y + (mv^2 - Bp^2)\,\beta \\ & = v \begin{pmatrix} 0 & \sigma_x \\ \sigma_x & 0 \end{pmatrix} p_x + v \begin{pmatrix} 0 & \sigma_y \\ \sigma_y & 0 \end{pmatrix} p_y + (mv^2 - Bp^2) \begin{pmatrix} 0 & \sigma_z \\ \sigma_z & 0 \end{pmatrix}, \end{aligned} \tag{1.22}$$

which could be solved similarly to one dimensional case.

1.1.3 Dirac equation in the lattice model and time reversal invariant

In this section, we introduce a lattice model to argue the parity of the energy dispersion which distinguishes the topological state from non-topological one. The continuous model discussed in the previous section is the long wavelength limit of the lattice model, which has a periodic structure. To construct the lattice model, we can simply replace k_i and k_i^2 by [10]

$$k_i \to \frac{1}{a}\sin k_i a, k_i^2 \to \frac{2}{a^2}\sin^2\frac{k_i a}{2}. \tag{1.23}$$

Note that the lattice model is equivalent to the continuous model in the long wavelength limit $k_i a \to 0$. Using this replacement, we show that whether the system is topological or not can be judged by the parity.

First, we define the unitary Hermitian parity operator P by

$$\boldsymbol{PxP = -x, PpP = -p, P\alpha_i P = -\alpha_i, P\beta P = \beta.} \tag{1.24}$$

The Dirac equation is invariant with parity P operation.

In one dimension, using replacement (1.23) to the Dirac equation, we obtain

$$H = A\sin k_x a\alpha_x + \left(\Delta - 4B\sin^2\frac{k_x a}{2}\right)\beta. \tag{1.25}$$

Eigenvalues and the occupied states are given by

$$E_\pm = \pm\sqrt{A^2\sin^2 k_x a + \left(\Delta - 4B\sin^2\frac{k_x a}{2}\right)^2} \tag{1.26}$$

and

$$\Psi_1 = \begin{pmatrix} -\frac{A\sin k_x a}{\sqrt{2E_+\left(E_+ + \Delta - 4B\sin^2\frac{k_x a}{2}\right)}} \\ 0 \\ 0 \\ -\frac{E_+ + \Delta - 4B\sin^2\frac{k_x a}{2}}{\sqrt{2E_+\left(E_+ + \Delta - 4B\sin^2\frac{k_x a}{2}\right)}} \end{pmatrix} \tag{1.27}$$

$$\Psi_2 = \Theta\Psi_1 \tag{1.28}$$

where $\Theta = -i\sigma_y K$ is a time reversal operator and K is the complex conjugation.

The Hamiltonian is invariant with parity operation P as described by

$$PH(k)P = H(-k). \tag{1.29}$$

However, in certain points Γ_i, it also satisfies

$$PH(\Gamma_i)P = H(-\Gamma_i) = H(\Gamma_i). \tag{1.30}$$

In this case, Γ_i is called time-reversal-invariant (TRI) momenta.

In one dimension, there are two TRI momenta $\Gamma_1 = 0$ and $\Gamma_2 = \frac{\pi}{a}$. Now, the eigenvalue of the parity operator P of $|\Psi_1\rangle$ at TRI momenta is given by

$$\delta|_{ka=0} = \langle\Psi_1|P|\Psi_1\rangle = sgn(-\Delta), \delta|_{ka=\pi} = \langle\Psi_1|P|\Psi_1\rangle = sgn(-\Delta + 4B). \tag{1.31}$$

Therefore, the parity switches the sign at $\Delta = 0$ and $\Delta = 4B$. The Z_2 index ν is given by the product of eigenvalues of the parity at all TRI momenta,

$$(-1)^\nu = \delta|_{ka=0}\delta|_{ka=\pi} = sgn(-\Delta)sgn(-\Delta + 4B), \tag{1.32}$$

which becomes topologically nontrivial when $0 < \Delta^2 < 4\Delta B$ and $\nu = 1$.

1.1.4 Topological index by time reversal symmetry

When the system has time reversal symmetry, the Hamiltonian satisfies

$$H(-k) = \Theta H(K)\Theta^{-1} \tag{1.33}$$

where time reversal operator $\Theta = -i\sigma_y K$ and K is the complex conjugation. When a point Γ_i satisfies $-\Gamma_i = \Gamma_i + \boldsymbol{G}$ where $\boldsymbol{G}$ is a reciprocal lattice, it also satisfies

$$H(\Gamma_i) = \Theta H(\Gamma_i)\Theta^{-1}. \tag{1.34}$$

In this case, Γ_i is called time reversal invariant momenta. Thus, each eigenstates has at least two degeneracy, called the Kramers degeneracy. There are also at least two energy bands $E_{2n-1}(K)$ and $E_{2n}(K)$ where $E_{2n-1}(-k) = E_{2n}(k)$. This pair is called Kramers pair.

Here assume that the system is one dimensional and their are 2N energy bands that contains N Kramers pairs. Int this case, Γ_i is found at $k = 0, \pi$ and the Kramers pairs satisfy

$$|u_n^I\rangle(-k) = -e^{i\chi_{k,n}}\Theta\,|u_n^{II}\rangle(k) \tag{1.35}$$

$$|u_n^{II}\rangle(-k) = e^{i\chi_{k,n}}\Theta\,|u_n^{I}\rangle(k) \tag{1.36}$$

as $\Theta^2 = -1$, where I or II denote the Kramers pair. Using this, the charge polarization

for band I is given by [5]

$$\begin{aligned} P^I &= \int_{BZ} \frac{dk}{2\pi} A_k^I \\ &= \int_0^{\pi} \frac{dk}{2\pi} A_k^I + \int_{-\pi}^{0} \frac{dk}{2\pi} A_k^I \\ &= \int_0^{\pi} \frac{dk}{2\pi} A_k - \frac{1}{2\pi} \sum_n (\chi_{\pi,n} - \chi_{0,n}) \end{aligned} \tag{1.37}$$

where $A_k^{I,II}$ is the summation of the Berry connection $A_k^{I,II} = \sum_n A_k^{n,I,II}$.

Here we define a (2N$\times$ 2N) matrix w which elements are

$$w_{mn}(k) = \langle u_m(-k)|\Theta|u_n(k)\rangle \,. \tag{1.38}$$

Then, most of the terms are zero except for

$$\langle u_m^I(-k)|\Theta|u_n^{II}(k)\rangle = -e^{i\chi_{k,n}} \tag{1.39}$$

$$\langle u_m^{II}(-k)|\Theta|u_n^I(k)\rangle = e^{i\chi_{k,n}} \tag{1.40}$$

which are off-diagonal. The matrix is antisymmetric at $k = 0, \pi$ and its Pfaffian satisfies

$$\ln \frac{Pf[w(\pi)]}{Pf[w(0)]} = i \sum_n (\chi_{\pi,n} - \chi_{0,n}). \tag{1.41}$$

Substiuting Eq. (1.41) to Eq. (1.37), we obtain [5]

$$P^I = \frac{1}{2\pi} \left[\int_0^{\pi} dk A_k + i \ln \frac{Pf[w(\pi)]}{Pf[w(0)]} \right]. \tag{1.42}$$

The time reversal polarization P_θ is therefore given by

$$\begin{aligned} P_\theta &= P^I - P^{II} \\ &= \frac{1}{2\pi}\left[\int_0^\pi dk A_k - \int_{-\pi}^0 dk A_k + 2i \ln \frac{Pf[w(\pi)]}{Pf[w(0)]}\right] \\ &= \frac{1}{2\pi i}\left[\ln \frac{\det(w(\pi))}{\det(w(0))} - 2\ln \frac{Pf[w(\pi)]}{Pf[w(0)]}\right] \end{aligned} \tag{1.43}$$

which provides

$$(-1)^{P_\theta} = \frac{\sqrt{\det w(0)}}{Pf(w(0))}\frac{\sqrt{\det w(\pi)}}{Pf(w(\pi))}. \tag{1.44}$$

This is the topological invariant in one dimension.

In general case, topological invariant is expressed as

$$(-1)^\nu = \prod_i \frac{\sqrt{\det(w(\Gamma_i))}}{Pf(w(\Gamma_i))}. \tag{1.45}$$

1.2 Topological superconductors

Right after the classification of TIs, the concept of non-trivial topological properties was extended to fully gapped superconductors that could possess a gapless surface state. This new class of matter is called topological superconductor (TSC)s.

1.2.1 Dirac equation in complex p-wave superconductor

First, we start with the standard BCS model. In BCS theory, the two-body interaction Hamiltonian is given by [11]

$$H = \sum_k \left(\xi_k c_k^\dagger c_k + \frac{1}{2} V c_k^\dagger c_{-k}^\dagger c_{-k} c_k\right). \tag{1.46}$$

Taking the mean field approximation, the second term can be replaced by

$$c_k^\dagger c_{-k}^\dagger c_{-k} c_k \approx \langle c_k^\dagger c_{-k}^\dagger \rangle c_{-k} c_k + c_k^\dagger c_{-k}^\dagger \langle c_{-k} c_k \rangle - \langle c_k^\dagger c_{-k}^\dagger \rangle \langle c_{-k} c_k \rangle \tag{1.47}$$

and Eq.(1.46) can be rewritten as

$$\begin{aligned} H_{MF} &= \sum_k \xi_k c_k^\dagger c_k + \frac{1}{2} \sum_k \left(\Delta^* c_{-k} c_k + \Delta c_k^\dagger c_{-k}^\dagger \right) + V^{-1} |\Delta|^2 \\ &= \frac{1}{2} \sum_k (c_k^\dagger c_{-k}) \begin{pmatrix} \xi_k & \Delta \\ \Delta^* & -\xi_k \end{pmatrix} \begin{pmatrix} c_k \\ c_{-k}^\dagger \end{pmatrix} + V^{-1} |\Delta|^2, \end{aligned} \tag{1.48}$$

where $\Delta = V \langle c_{-k} c_k \rangle$. Diagonalizing the matrix which is called Bogoliubov-de Gennes Hamiltonian, we obtain $E_k = \sqrt{\xi_k^2 + |\Delta|^2}$.

For an s-wave superconductor with even parity, it is topologically trivial. For an odd-parity p-wave superconductor, on the other hand, since it cannot be adiabatically changed to the even parity it is very likely a topological superconductor. Below we see how the quasiparticle band can be topological.

In a complex p-wave superconductor, for small k, Δ_k has the form

$$\Delta_k = \Delta(k_x \pm i k_y). \tag{1.49}$$

Substituting Eq.(1.49), the matrix in Eq.(1.48) becomes

$$\begin{pmatrix} \xi_k & \Delta(k_x \pm i k_y) \\ \Delta^*(k_x \mp i k_y) & -\xi_k \end{pmatrix} = \Delta k_x \sigma_x \mp \Delta k_y \sigma_y + \xi_k \sigma_z, \tag{1.50}$$

which exactly has the form of Dirac equation (1.4). Note that this energy dispersion is not for electrons but rather for the quasiparticles. Thus, the edge state is also not a simple gapless Dirac cone, but a gapless state for quasiparticles, which is called

Majorana fermion as shown in the next section.

1.2.2 Majorana excitation in topological superconductors

Majorana fermion is a particle which antiparticle is itself. Majorana fermion operator γ satisfies

$$\gamma_i^\dagger = \gamma_i. \tag{1.51}$$

Also, as as a fermion, it satisfies

$$\gamma_i \gamma_j^\dagger + \gamma_j^\dagger \gamma_i = \delta_{ij}. \tag{1.52}$$

1.2.3 Kitaev model

A simple model to predict Majorana fermions in materials was proposed by Kitaev [12]. The Kitaev model is a spinless p-wave superconductor in one-dimensional lattice. The Hamiltonian is given by

$$H = -\mu \sum_{i=1}^{N} c_i^\dagger c_i - \frac{1}{2} \sum_{i=1}^{N-1} \left(t c_i^\dagger c_{i+1} - \Delta c_i c_{i+1} + h.c. \right), \tag{1.53}$$

where μ,t and Δ are chemical potential, hopping amplitude and superconducting order parameter, respectively. Here we think about the special case where μ=0 and t=Δ. In this case, the Hamiltonian is given by

$$H = -\frac{t}{2} \sum_{i=1}^{N-1} \left(c_i - c_i^\dagger \right) \left(c_{i+1} + c_{i+1}^\dagger \right) = -it \sum_{i=1}^{N-1} \gamma_{B,i} \gamma_{A,i+1}, \tag{1.54}$$

where

$$\gamma_{B,i} = \frac{i}{\sqrt{2}} \left(c_i - c_i^\dagger \right) \tag{1.55}$$

$$\gamma_{A,i1} = \frac{1}{\sqrt{2}} \left(c_i + c_i^\dagger \right). \tag{1.56}$$

γ_A and γ_B are Majorana fermions and satisfy Eq.(1.51). This means that two nearest Majorana fermions on a lattice site couple to each other. To further clarify this coupling, a new fermion operator

$$d_i = \frac{1}{\sqrt{2}} \left(\gamma_{A,i+1} + i\gamma_{B,i} \right) \tag{1.57}$$

is introduced to obtain

$$H = t \sum_{i=1}^{N-1} \left(d_i^\dagger d_i - \frac{1}{2} \right). \tag{1.58}$$

Here we realize that $\gamma_{A,1}$ and $\gamma_{B,N}$ are not included in the Hamiltonian. Indeed, an operator $f = \frac{1}{\sqrt{2}} \left(\gamma_{A,1} + i\gamma_{B,N} \right)$ has zero energy. This is called Majorana zero mode, and can be potentially used for error-tolerant topological quantum computing.

1.2.4 Topological superconductivity with time-reversal symmetry and odd parity

One of the promising playgrounds is odd-parity superconductors. As shown by Fu in 2010 [13], sufficient criteria for a TSC is (a) odd parity paring symmetry with a full superconducting gap and (b) the Fermi surface in the normal state enclosed the odd number of TRI momenta in the Brillouin zone, if the material is a TRI superconductor with inversion symmetry. This indicates that a topological superconductor nature could be judged just from the normal state Fermi surface, which is much easier than knowing the topology of quasiparticle structure.

The proof in [13] is following. We start from the Bogoliubov-de Gennes Hamiltonian $H(k)$ in Eq. (1.48) with chemical potential μ,

$$H(k) \;=\; \begin{pmatrix} H_0(k) - \mu & \Delta(k) \\ \Delta^*(k) & -H_0(k) + \mu \end{pmatrix} = (H_0(k) - \mu)\tau_z + \Delta\tau_x. \tag{1.59}$$

Given the parity operator $\Pi = P \otimes \tau_z$, the Hamiltonian is invariant under Π

(i.e. $\Pi H(k)\Pi = H(-k)$), since $PH_0(k)P^{-1} = H_0(-k)$ and $P\Delta(k)P^{-1} = -\Delta(-k)$ by definition of odd parity. At TRI momenta Γ_i, the Hamiltonian satisfies $[\Pi, H(\Gamma)] = 0$, thus the eigenstates of the Hamiltonian $|psi_n(\Gamma_i)\rangle$ is also the eigenstates of Π with the eigenvalue $\xi_n(\Gamma_i) = \pm 1$:

$$\Pi \left|psi_n(\Gamma_i)\right\rangle = \xi_n(\Gamma_i) \left|\psi_n(\Gamma_i)\right\rangle . \tag{1.60}$$

In this case, the Z_2 invariant ν has a simpler form [5] as

$$(-1)^\nu = \prod_{i,m} \xi_{2m}(\Gamma_i). \tag{1.61}$$

In general, the Fermi surface is not close to Γ_i. In this case, with assuming weak coupling, $H(\Gamma_i) \approx H_0(\Gamma_i)$ since $\Delta(\Gamma_i)$ is much smaller than $H_0(k) - \mu$. Thus, the eigenfunction $\psi_n(\Gamma_i) \approx u_n(\Gamma_i)$ where $u_n(\Gamma_i)$ is the eigenstates of $H_0(k)$. This gives the equation

$$\xi_m(\Gamma_i) = p_m(\Gamma_i)\tau_m(\Gamma_i) \tag{1.62}$$

where $p = \pm 1$ and $\tau = \pm 1$ are the eigenvalues of the inversion operator P and the particle-hole operator τ_z, respectively. Here $\tau_m(\Gamma_i) = 1$ if the band is occupied and $\tau_m(\Gamma_i) = -1$ if the band is unoccupied. In other words, $\tau_m(\Gamma_i) = -sgn(\epsilon_m(\Gamma_i) - \mu)$. Therefore, Eq. (1.61) results in

$$(-1)^\nu = \prod_{i,m} p_{2m}(\Gamma_i) sgn(\mu - \epsilon_m(\Gamma_i)) = \prod_{i,m} (-1)^{N(\Gamma_i)} \tag{1.63}$$

where $N(\Gamma_i)$ is the number of Γ_i outside the Fermi surface and unoccupied. Here we use $\prod_{i,m} p_{2m}(\Gamma_i) = \det[P] = 1$.

The result indicates that the topological invariant $\mu = 1$ if $N(\Gamma_i$ is odd. Given that the number of total Γ_i is even in the Brillouin zone, this indicates the condition

(b) mentioned above, and the proof is therefore given.

1.2.5 Topological superconductor candidates

In this section, I briefly describe the topological superconductor candidate materials and their current progress. In sharp contrast to other topological materials such as TIs, Dirac and Weyl semimetals, the existence of TSCs has not yet been confirmed. This is mainly due to the fact that not electrons but quasiparticles form a nontopological band in TSCs.

As shown in the section above, spinless p-wave superconductor possesses Majorana fermions on its end (1D) or edge (2D). Also, one of the superfluid phase (phase B) in helium 3 is known to be a 3D topological superfluid which possessed Majorana fermion on its surface.

There are three candidates of TSCs so far that have been studied intensively: Sr_2RuO_4, UPt_3 and doped Bi_2Se_3. For doped Bi_2Se_3, I will explain in detail in the latter chapter.

A superconductor Sr_2RuO_4 was discovered in 1994 [14]. Sr_2RuO_4 was initially focused on because it has the same layered structure as high T_c superconductors. The direct evidence of spin-triplet pairing was observed by Nuclear magnetic resonance (NMR) Knight shift, which does not drop across T_c [15]. Also, the muon spin rotation (μSR) measurement show that there is an internal magnetic field in the superconducting state, which means that time-reversal symmetry is broken [16]. Combining these results, Sr_2RuO_4 is believed to be p-wave superconductor with a chirality, or in short a chiral p-wave superconductor.

A heavy fermion superconductor UPt_3 was discovered in 1984 [17] with superconducting $T_c = 0.54$ K and antiferromagnetic transition $T_N = 6$ K. In addition, under magnetic fields the superconducting state has three phases, all of which are likely to be spin-triplet. UPt_3 is another material that is believed to have odd parity super-

conducting pairing. In contrast to Sr_2RuO_4, the superconducting pairing in UPt_3 is thought to be f-wave. Recently the theory proposed the possibility of topological Weyl superconductivity in UPt_3 [18].

While the superconducting state of Sr_2RuO_4 and UPt_3 has been mainly focused to argue the topological superconducting nature, the argument of doped Bi_2Se_3 also involves a lot of normal state information as discussed later.

More detailed information on topological superconductor candidates can be found in the review papers [19, 20].

1.3 Dirac semimetals

1.3.1 4×4 Hamiltonian matrix to describe Dirac and Weyl semimetals

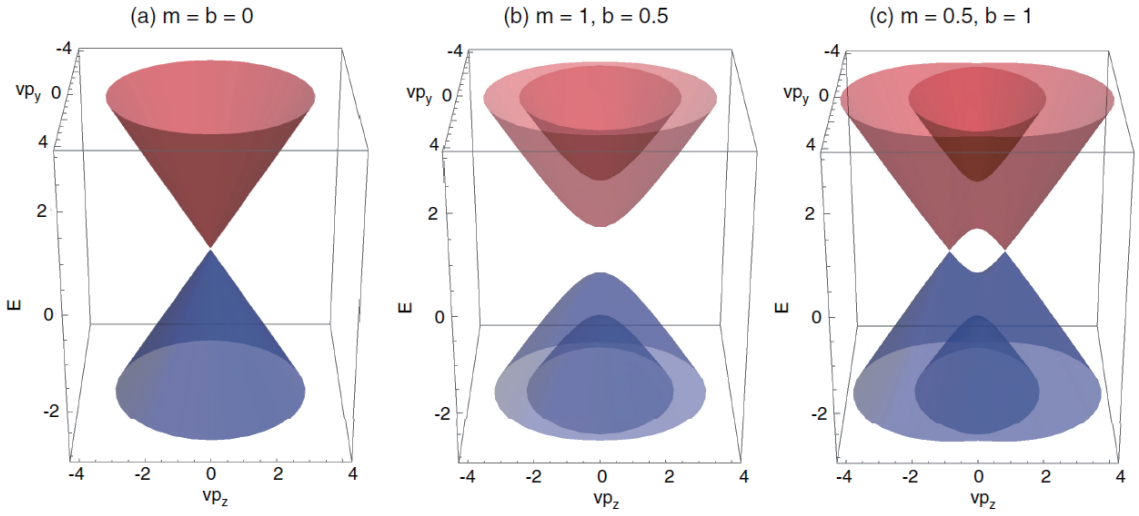

Figure 1.2: **Energy dispersion given by 4×4 Hamiltonian in Eq.** (1.65). The spectra is shown in $E_{s\mu}(k = 0, k_y, k_z)$ plane. (a) m=b=0 (Dirac semimetal) (b) m=1, b=0.5 (magnetic insulator) (c) m=0.5, b=1 (Weyl semimetal) Adapted from [21].

Dirac and Weyl semimetals are similar concepts. Indeed, in condensed matter physics, Dirac semimetal is the special case of Weyl semimetal. In this section, we

examine 4×4 Hamiltonian matrix to intuitively understand the difference between them [22].

Consider a 4×4 Hamiltonian [21]

$$\begin{aligned} H &= v\tau_x(\sigma \cdot k) + m\tau_z + b\sigma_z \\ &= \begin{pmatrix} m\mathbf{1} + b\sigma_z & v\sigma \cdot k \\ v\sigma \cdot k & -m\mathbf{1} \end{pmatrix} \end{aligned} \tag{1.64}$$

where σ_i and τ_i are Pauli matrices for spins and pseudospins, m is mass and b is the intrinsic magnetic field along z direction. Diagonalizing the Hamiltonian, we obtain four energy bands

$$E_{s\mu}(k) = s\sqrt{m^2 + b^2 + v^2k^2 + \mu 2b\sqrt{v^2k_z^2 + m^2}} \tag{1.65}$$

where $s = \pm 1$ and $\mu = \pm 1$. When $m = b = 0$, the Hamiltonian is reduced to that in the Dirac equation Eq. (1.4), resulting in the linear dispersion shown in Fig. 1.2 (a).

If the time reversal symmetry is present but inversion symmetry is not, only at TRI momenta there is a Kramers degeneracy. Also, if there is no time reversal but inversion symmetry, the bands are non-degenerate. If both of symmetry exist, the bands are doubly degenerate and Dirac point is fourfold degenerate. This is exactly what happens in Fig. 1.2 (a). If one of the symmetry is broken, this degeneracy disappears. For example, in Eq. (1.64), non-zero b corresponds to the internal magnetic field which breaks the time-reversal symmetry. In this case, the Dirac cone splits into two opposite handedness Weyl nodes as shown in Fig. 1.2 (c).

1.3.2 Nature of Dirac semimetals

Indeed, the Dirac semimetals do not show as exotic features as Weyl semimetals explained in the next section.

While a Dirac semimetal is the special case of a Weyl semimetal, the Chern number around the Dirac point is zero because it is a superposition of two Weyl nodes with opposite Chern number. Thus, the degeneracy in the Dirac point is not topologically protected. On the other hand, the Chern number is ± 1 for Weyl nodes, which is non-trivial. Thus, the Fermi arcs expected in Weyl semimetals may not exist in Dirac semimetals (described in the Weyl semimetal section).

Also, the chiral anomaly could be faint. In Weyl semimetals, two Weyl nodes are well separated in momentum space, so the scattering rate between nodes is small. However, In Dirac semimetals, the two points degenerate. Under a magnetic field, the degenerate Weyl nodes could split apart, but in general, the separation is not large enough to make the scattering rate small. Thus, the effect of a chiral anomaly in Dirac semimetals is weak.

1.3.3 Energy band of graphene: 2D Dirac semimetal

Graphene is the best example of two-dimensional Dirac semimetals. From the tight binding model, the Hamiltonian of graphene is given by

$$\mathcal{H} = \sum_k c^\dagger(k) H(k) c(k) \tag{1.66}$$

$$H(k) = \begin{pmatrix} 0 & f(k) \\ f^*(k) & 0 \end{pmatrix} \tag{1.67}$$

$$f(k) = t \sum_n e^{ik\cdot\delta_n}, \tag{1.68}$$

where $H(k)$ is a Bloch Hamiltonian and t is a hopping integral, δ_n is the positions of

nearest neighbor atoms from an atom. For graphene, δ_n is given by$\delta_1 = a\,(1,0)\,, \delta_2 = a\left(-\frac{1}{2}, \frac{\sqrt{3}}{2}\right), \delta_3 = a\left(-\frac{1}{2}, \frac{-\sqrt{3}}{2}\right)$. Therefore, we obtain

$$f(k) = t\left(e^{ik_x a} + 2e^{-ik_x a/2}\cos\frac{k_y a\sqrt{3}}{2}\right). \tag{1.69}$$

Eigenvalues are given by

$$\epsilon_{\pm}(k) = \pm\,|f(k)| = \pm t\sqrt{3 + 2\cos\sqrt{3}k_y a + 4\cos\frac{\sqrt{3}k_y a}{2}\cos\frac{3k_x a}{2}}. \tag{1.70}$$

The spectrum is shown in Fig.1.3. There are two Dirac points at $K = \frac{2\pi}{3a}\left(1, \frac{1}{\sqrt{3}}\right), K' = \frac{2\pi}{3a}\left(1, -\frac{1}{\sqrt{3}}\right)$, where two bands touch to each other. Expanding around K point, we obtain

$$\begin{aligned} f(K+k) &= t\textstyle\sum_n e^{i(K+k)\cdot\delta_n} \\ &\approxeq t\textstyle\sum_n e^{iK\cdot\delta_n}(1 + ik\delta_n) \\ &= ikt\textstyle\sum_n \delta_n e^{iK\cdot\delta_n} \\ &= \tfrac{3}{2}tae^{i\frac{\pi}{6}}(k_x - ik_y). \end{aligned} \tag{1.71}$$

Therefore, Bloch Hamiltonian is given by

$$\begin{aligned} H(K+k) &= \begin{pmatrix} 0 & f(K+k) \\ f^*(K+k) & 0 \end{pmatrix} \\ &= \begin{pmatrix} 0 & \frac{3}{2}tae^{i\frac{\pi}{6}}(k_x - ik_y) \\ \frac{3}{2}tae^{-i\frac{\pi}{6}}(k_x + ik_y) & 0 \end{pmatrix}. \end{aligned} \tag{1.72}$$

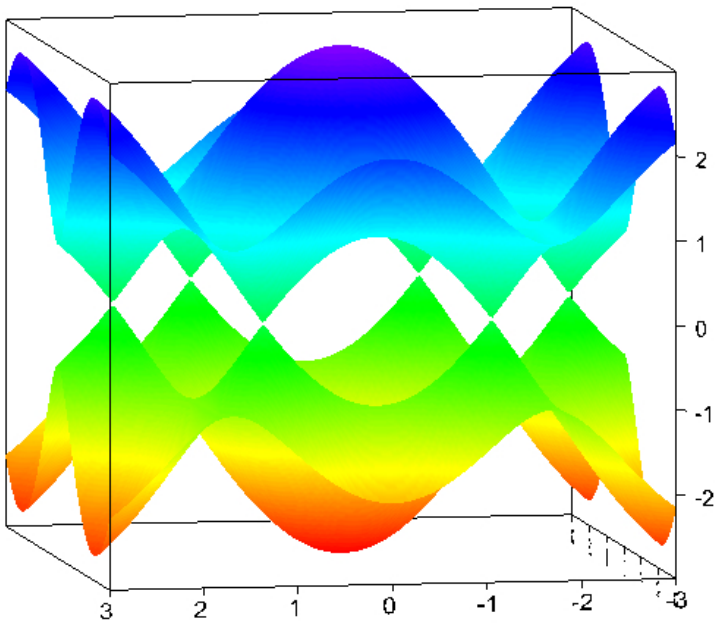

Figure 1.3: **Energy dispersion of graphene .**

Without the phase term, this Hamiltonian has the form $H(K+k) = \hbar v_f k \cdot \sigma$ which is exactly the massless Dirac equation in Eq. (1.4). Thus, around the K point the system follows the two-dimensional Dirac physics.

1.3.4 3D Dirac semimetals

As mentioned before, Dirac semimetals emerge at the phase boundary between a band insulator and a topological insulator. This case has been observed in $TlBi(Se_{1-x}S_x)_2$ and $(Bi_{1-x}In_x)_2Se_3$. In $TlBi(Se_{1-x}S_x)_2$, $TlBiS_2$ is topologically trivial and $TlBiSe_2$ is non-trivial. Topological phase transition happens at X=0.5 [23, 24]. For $(Bi_{1-x}In_x)_2Se_3$,

the topological phase transition occurs at around x=0.05 [25]. However, those examples require fine tuning of stoichiometric ratio.

Another route to realize Dirac semimetals is to take advantage of crystal symmetry. As a natural crystal, Cd_3As_2 and Na_3Bi are proposed to be Dirac semimetals [26, 27]. Soon after the prediction, the existence of Dirac cone has been confirmed by angle-resolved photoemission spectroscopy (ARPES) [28, 29].

For further details, referring to a recent review article [30] would be helpful.

1.4 Weyl semimetals

1.4.1 Weyl equation

Weyl fermion was first proposed by Weyl in 1929 as a solution to Weyl equation [31]. Assuming the mass $m = 0$ in Eq. (1.4), we obtain

$$i\hbar\frac{\partial}{\partial t}\Psi_{\pm} == c\alpha \cdot p\Psi_{\pm}. \tag{1.73}$$

where $\Psi_{\pm} = \Psi_1 \pm \Psi_2$. The Hamiltonian and energy dispersion are $H = \pm cp \cdot \sigma$ and $E_{\pm}(p) = \pm cp$. This means that the propagation vector and their spin is parallel or anti-parallel in Weyl fermions, and this nature is called chirality.

1.4.2 Nature of Weyl semimetals

As discussed in the Dirac semimetal section, Weyl nodes appear when one of time reversal or inversion symmetry is broken. Instead of zero Chern number in Dirac point, Weyl nodes pair has the opposite Chern number $\pm$ 1. Since the Chern number is non-trivial, there are a few topological features expected for Weyl semimetals.

The first topological feature is Fermi arc observed in the surface. This is the consequence of the bulk-edge correspondence, and when the Fermi level E_F=0, the surface state is a line connecting two Weyl nodes projected to the surface (which

is called Fermi arc). When the Fermi level is shifted, the Fermi arc still exists and connects two bands around the Weyl nodes. The existence of Fermi arc in the surface of Weyl semimetal was confirmed by ARPES as mentioned in the next section.

Another important feature of Weyl semimetal is the chiral anomaly. When a magnetic field and electric field is applied parallel to the Weyl semimetal, the electrons can be pumped between opposite Weyl nodes, resulting in the number change of particles with each chirality, i.e., a chiral anomaly. The chiral anomaly leads to the negative magnetoresistance (MR) which is proportional to $E \cdot B$.

1.4.3 Realization of Weyl semimetals

To have Weyl semimetals rather than Dirac semimetals, one of time reversal or inversion symmetry has to be broken. Various Weyl semimetal without inversion symmetry is recently proposed and confirmed. In 2015, TaAs type materials (TaAs, TaP, NbAs, NbP) are predicted to be Weyl semimetals [32, 33], soon followed by experimental confirmation [34, 35, 36].

The Weyl semimetals without time reversal symmetry are more difficult to find. Weyl nodes have not been confirmed experimentally, but there are several candidates such as iridates[37], half-Heusler compounds[38] and Mn_3X (X=Sn, Ge) [39, 40]. Further experiments are required to confirm the magnetic Weyl semimetal.

CHAPTER II

Experimental setup

2.1 Measurement techniques

2.1.1 Torque magnetometry

Torque magnetometry is a very powerful tool that measures the magnetic properties of materials. When a magnetic field H is applied to the sample, generally the direction of sample magnetization is slightly different from the magnetic field direction. Since the free energy with respect to the external field H is given by

$$\mathcal{F} = \mu_0 V \vec{M} \cdot \vec{H}, \tag{2.1}$$

the free energy is minimized when two vectors are parallel, resulting in generating torque to align them. This magnetic torque is given by the derivative of $\mathcal{F}$ with respect to the magnetic field tilt angle ϕ:

$$\vec{\tau} = \mu_0 V \vec{M} \times \vec{H} = \mu_0 V (M_z H_x - M_x H_z)\hat{y}, \tag{2.2}$$

where V is the volume of the sample, $\vec{H}$ is the external magnetic field, and $\vec{M}$ is the magnetization of the sample. When the sample is paramagnetic or diamagnetic and

not saturating, the magnetization can be described by $M{=}\chi H$, and 2.2 simplifies to

$$\vec{\tau} = \mu_0 V(\chi_z H_z H_x - \chi_x H_x H_z)\hat{y} = \mu_0 V \Delta\chi H^2 sin\theta cos\theta \hat{y}, \tag{2.3}$$

where $\Delta\chi = \chi_z - \chi_x$. Thus, torque is only sensitive to the anisotropy. Since most of the noise signal is isotropic, torque can be free from background signals. Also note that, for non-saturating paramagnetic or diamagnetic materials, the torque response is a function of H^2 and sin 2θ.

Among methods for measuring magnetic properties of samples, torque magnetometry is the most sensitive to the quantum oscillation. Also, it can be easily combined with a rotator, very high magnetic fields (up to 45 T for the capacitive cantilever, 100 T for piezoresistive) and very low temperatures (down to 10 mK).

Usually, magnetic torque is measured by detecting the deflection of the cantilever on which the sample is mounted. In particular, capacitive and piezoresistive cantilevers are most often used. For capacitive cantilevers, the sample is mounted on the metallic cantilever and magnetic torque is tracked by measuring the capacitance change between the cantilever and metallic plate beneath it. On the other hand, piezoresistive cantilevers use the piezoresistive effect: when there is a tension applied to the cantilever, its resistance becomes larger. Thus, magnetic torque can be measured by tracking the resistance change.

Advantages and disadvantages of these methods are following. The biggest advantage of a capacitive cantilever is that magnetic response from the cantilever itself is negligible since the capacitance mostly depends on the gap size between the cantilever and the metallic plate. Due to magnetoresistance, piezoresistive cantilevers suffer from large background signal under high magnetic fields. Also, the sample size could be much larger for capacitive cantilevers, resulting in much easier sample mounting. Furthermore, due to the dissipation, piezoresistive cantilevers cannot be

used under high vacuum and low temperature below 2 K. The biggest disadvantage of capacitive cantilevers is that, however, it requires two coaxial cables to measure one cantilever. This is because of the 1000 times larger capacitance from the twisted pairs. Also, the eigenfrequency of capacitive cantilevers is around 1 kHz, which is orders of magnitude smaller than that of piezoresistive one. This makes capacitive cantilever difficult to be used in pulsed magnetic fields.

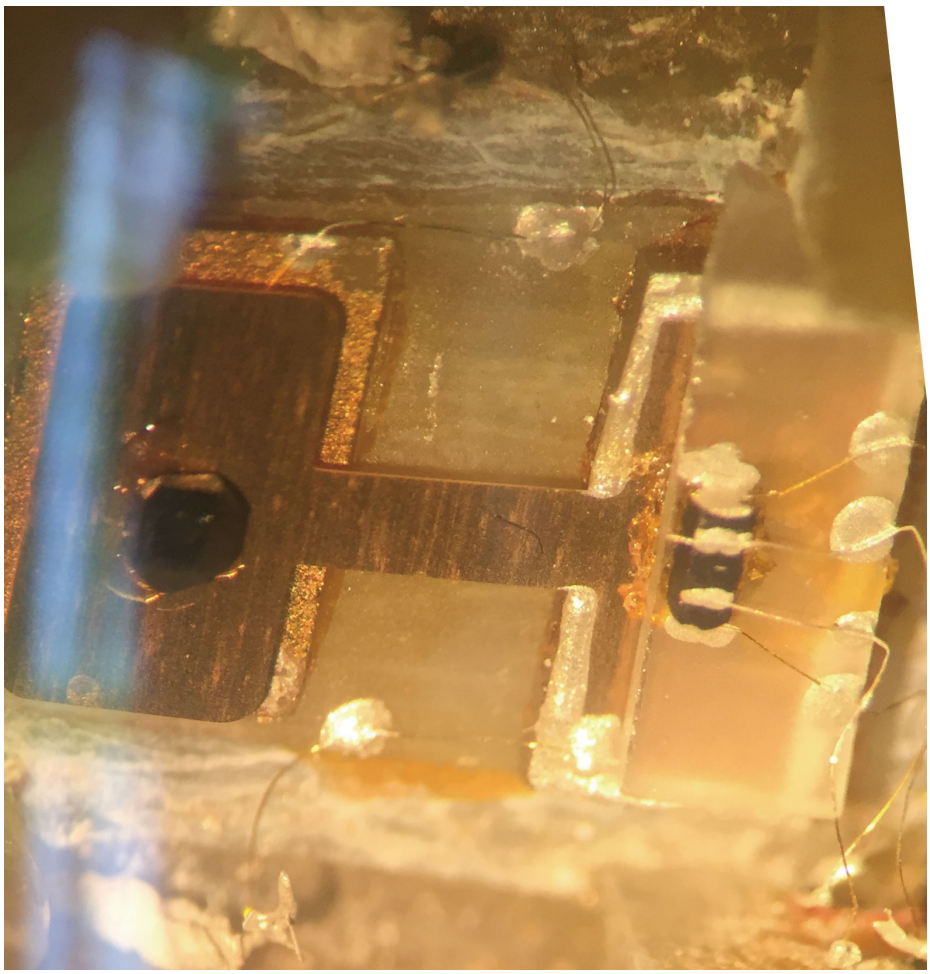

Figure 2.1: **Typical capacitive cantilever setup with a transport sample.**

In this study, we used the capacitive cantilever. Typical cantilever setup is shown in Fig. 2.1. The substrate and spacer are made of sapphire. We use 25 μm brass, 75 μm Kapton with a metallic coating and 25 or 75 μm Be/Cu for cantilevers. The cantilever and gold film are connected to the inner coaxial wire by 25 μm gold wires.

The typical gap size between the cantilever and the gold film is 250 μm, resulting in a zero field capacitance C_0 of 0.5 - 1 pF. The capacitance change was tracked with a digital capacitance bridge Andeen-Hagerling AH2700A. Typical parameters are 7 kHz and 15 V excitation, 7 averaging times.

The capacitance of the cantilever is given by

$$C_0 = \epsilon_0 \frac{A}{d} \tag{2.4}$$

where A is the area of the cantilever head and d is the gap between the cantilever and gold film. When a magnetic field is applied, a torque is generated and the cantilever is deflected. The deflection can be measured by tracking the capacitance change

$$\Delta C = C - C_0 \tag{2.5}$$

where $C = \epsilon_0 \frac{A}{d+\Delta d}$ and Δd is the change of the gap size.

For small Δd, by Hooke's Las, we can assume that the torque $\tau = k\Delta$d, where k is a spring constant of the cantilever. Also, (2.5) can be approximated as

$$\Delta C = \epsilon_0 \frac{A}{d} - \epsilon_0 \frac{A}{d+\Delta d} \approxeq C_0 \frac{\Delta d}{d}. \tag{2.6}$$

Thus, the capacitance change is proportional to the torque.

The spring constant of the cantilever is calibrated by the gravitational response or Lorenz force. When the cantilever is rotated with respect to the vertical direction, the capacitance change due to the gravitational effect is given by

$$\Delta C = mglsin\theta = k\Delta d \tag{2.7}$$

where m is the sample of the mass, g is gravitational acceleration, l is the length

between the root of the cantilever and the sample and θ is the angle between the cantilever arm direction and the vertical direction. Similarly, the spring constant can be calibrated by attaching a gold wire on to the cantilever perpendicular to the arm with applied current and magnetic field. The Lorenz force effect is given by

$$\Delta C = IlBsin\theta = k\Delta d \tag{2.8}$$

where I is the current on the wire, B is the magnetic field and θ is the angle between the cantilever arm and the magnetic field. Note that, in the usual case, the field is always perpendicular to the current.

2.1.2 Electronic transport

Electronic transport measurements are the fundamental techniques to probe the electronic properties of the sample. For the most basic properties, the longitudinal resistivity ρ_{xx} and the transverse resistivity ρ_{xy} (or the Hall effect) are often measured.

Most of the case, we use the standard 4-wire technique to perform the transport measurement. Typically four parallel gold wires are attached to the sample by silver paste. The other end is connected to the socket pins or the twisted pairs on the probe also by silver paste. We typically use Keithley 6220 as a current source, and the voltage across the sample is detected by the Stanford Researach SR830 lock-in amplifier. The typical frequency for the measurement is around 13 Hz to confirm the D.C. limit.

The schematic diagram of the transport measurement is shown in Fig. 2.2. For the ideal measurement, the sample shape is regular and has the uniform dimension of thickness t and width w with well defined sample surfaces. In this case, the longitudinal resistivity $\rho_{xx}$is given by

$$\rho_{xx} = \frac{V_{xx}tw}{Il} \tag{2.9}$$

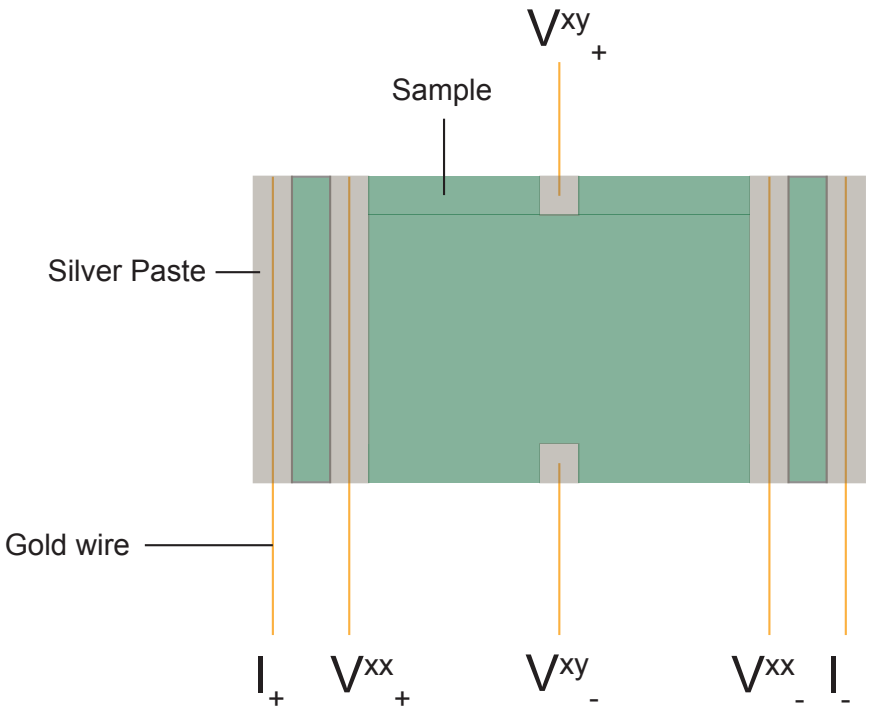

Figure 2.2: **Typical 4-wire transport measurement setup.**

where V is the detected voltage, I is the applied current and l is the sample thickness. Similarly, the transverse resistivity ρ_{xy} is given by

$$\rho_{xy} = \frac{V_{xy}t}{I}. \tag{2.10}$$

Another way to obtain the resistivity, the Van der Pauw method was also used as the schematic is shown in Fig. 2.3. To measure ρ_{xx}, the left configuration can be used. For the square configuration, the resistivity is obtained by

$$\rho_{xx} = \frac{\pi V t}{I \log 2}. \tag{2.11}$$

ρ_{xy} can be measured in the right configuration of Fig. 2.3, and it is the same as Eq. (2.10).

The biggest advantage of this method is that it only requires 4 wires to measure

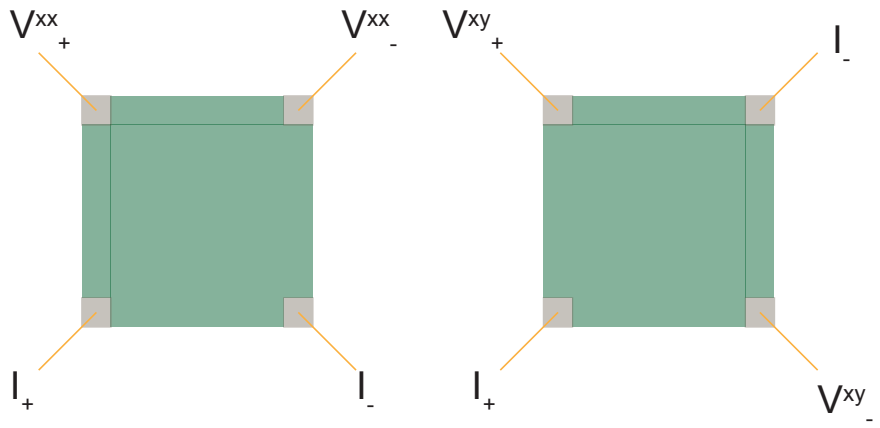

Figure 2.3: **Van der Pauw setup.**

both of ρ_{xx} and ρ_{xy}. Also, under magnetic fields, flipping the current and voltage leads act as if reversing the sign of the magnetic field. Thus, the ρ_{xy} signal can be symmetrized without sweeping the magnetic field to the other direction.

CHAPTER III

Rotational symmetry breaking in the superconducting state of $Nb_xBi_2Se_3$

3.1 Background

Doped Bismuth Selenide (Bi_2Se_3) is one of the most promising candidates for topological superconductors since the bulk superconducting state could lead to the proximity effect on the topological surface state, resulting in the topological superconducting state. In this section, I described in detail what has been observed and proposed in doped Bi_2Se_3 series.

3.1.1 Cu-doped Bi_2Se_3

3.1.1.1 Before nematic order

Cu-doped Bi_2Se_3 ($Cu_xBi_2Se_3$) is the first doped TI that was found to be superconducting [41], with T_c up to 4 K. The crystal structure is shown in Fig.3.1, adapted from ref. [41]. The unit cell consists of five atomic layers of Bi and Se, with Cu atomic layers are intercalated in between acting as a dopant. Thus, it has almost identical X-ray diffraction pattern as bulk Bi_2Se_3, in which the crystal structure belongs to D_{3d} point group. Since a topological surface state could exist even if more carrier is doped, it would be expected that the bulk superconducting state will lead to the

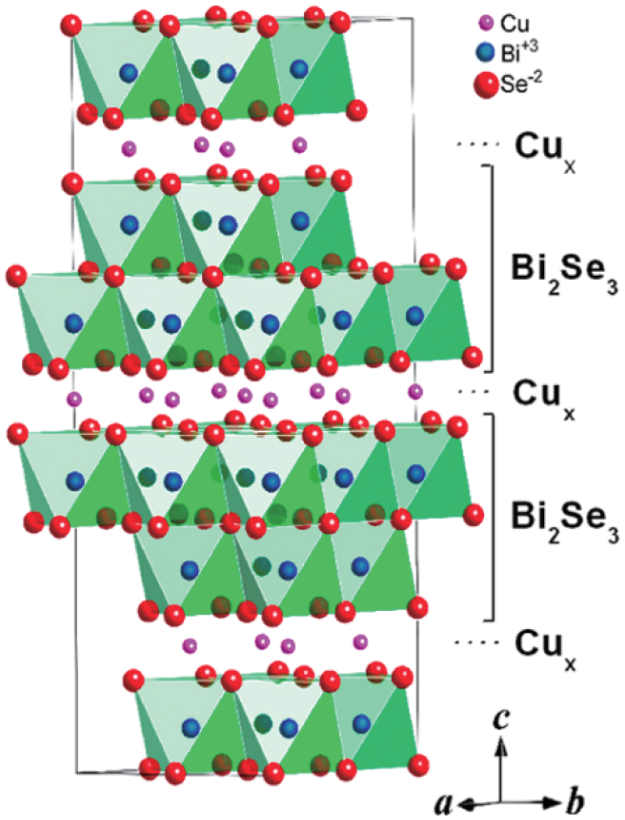

Figure 3.1: **Crystal structure of Cu-doped Bi_2Se_3.** A unit cell consists of five triangular atomic layers of Bi and Se, intercalated by Cu layers in between. Adapted from ref.[41].

proximity effect induced in the topological surface state. Therefore, this system is one of the promising candidates for the topological superconductivity.

The existence of topological surface state is confirmed in the doped Bi_2Se_3 by ARPES experiments [42] as shown in Fig. 3.2. While the chemical potential is much higher than that of the bulk Bi_2Se_3, doping effect did not affect the shape of the band structure. Furthermore, as shown in Fig. 3.2 (f), the shape of the bulk conduction band is best fit by a massive Dirac dispersion model rather a classical parabolic model. Also, A small bend of the band shown in Fig. 3.2 (f) indicates electron-boson interaction, which suggests that the superconducting Cooper pair is formed in the relativistic regime where the chemical potential lies.

It is not straightforward to grow Cu-doped Bi_2Se_3 single crystals. In the first report [41], crystals are grown by a usual melt-growth technique in which all the elements are melt together then slowly cooled down to crystallize. However, the superconducting volume fraction was limited to 30% in this method, because the location of Cu atoms cannot be well controlled, resulting in sitting on Bi sites. Soon after that, an electrochemical method was used to intercalate Cu atoms and achieved a shielding fraction around 50% [43]. Later, single crystals with a similar shielding fraction was obtained by melting method [44] and the combination of melt and electrochemical techniques [45].

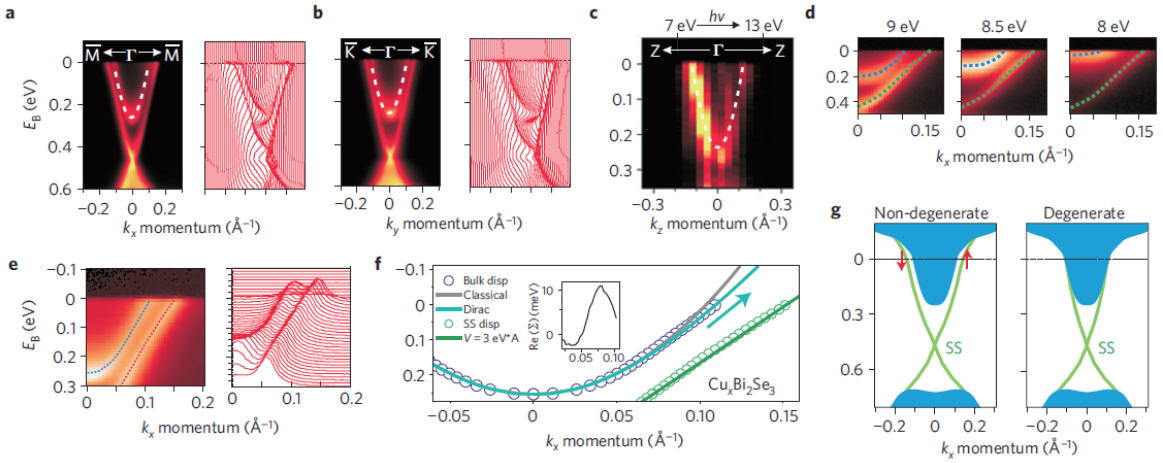

Figure 3.2: **ARPES resluts in Cu-doped Bi_2Se_3.** (a)(b) ARPES data from Γ point towards $\bar{M}$ and $\bar{K}$ points, respectively. (c) Dispersion along the z-axis. (d) Well-split bands between the surface and the bulk. (e)(f) Comparison of classical and Dirac energy dispersion fitting for the bulk band. (g) The Cooper pair is formed with the presence of non-degenerate surface state. Adapted from ref.[42].

Stimulated by the discovery of superconductivity in $Cu_xBi_2Se_3$, an exotic possibility of odd-parity topological superconductivity was proposed for Cu-doped Bi_2Se_3 by Fu and Berg [13]. In this theory, sufficient criterion for a TSC is (a) odd parity paring symmetry with a full superconducting gap and (b) the Fermi surface in the normal state enclosed the odd number of TRI momenta in the Brillouin zone, if the material

is a TRI superconductor with inversion symmetry. The detailed proof is explained in Chapter I. These criteria are very useful for experimentalists, as they could be experimentally proved straightforward. In particular, it is noteworthy that criterion (b) could be checked by probing the band structure in the normal state rather than the superconducting properties.

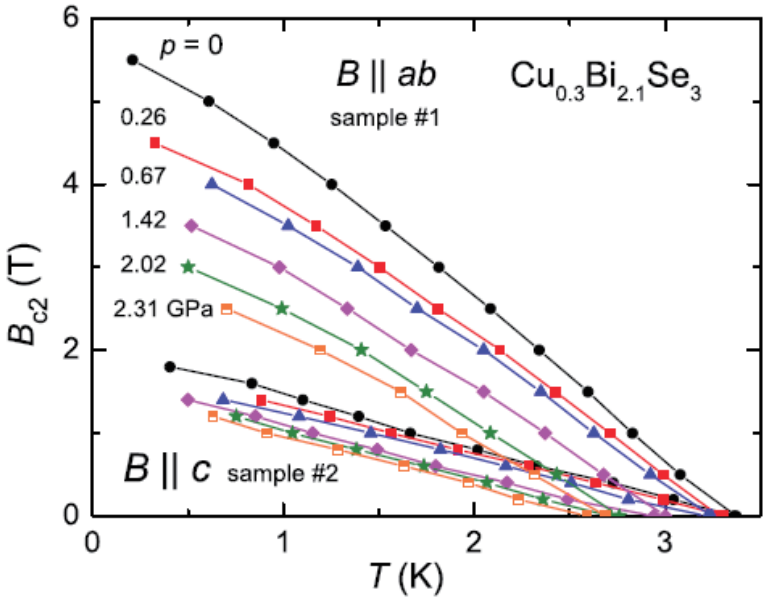

Figure 3.3: **Tempearture dependence of upper critical field H_{c2} at different pressures in Cu-doped Bi_2Se_3.** The theoretical H_{c2} calculated by Pauli and orbital limit is lower than the experimental observation. Adapted from ref.[42].

The search for odd-parity pairing (criterion (a) above) has been controversial. ARPES is the best method to directly observe the superconducting gap symmetry, as used for high-T_c superconductors. However, T_c of 4 K is too low for ARPES to elucidate the gap structure. The pressure study shows the absence of Pauli limit in the upper critical field, indicating the triplet paring [46]. Fig. 3.3 shows the temperature dependence of upper critical field H_{cs} at different pressures. Generally, the upper critical field is limited by two factors: Pauli limit and orbital limit. The Pauli limit H_p originates from the Zeeman energy splitting between spin-up and spin-

down, resulting in breaking the Cooper pair. For a spin-singlet pairing and weak coupling case, H_p =1.84 T_c (T/K). For a spin-triplet pairing, since the electrons in Cooper pairs have the same spin orientation, the Pauli limit is absent. Thus, the absence of Pauli limit indicates the triplet pairing. The detailed discussion is described in Chapter IV. Here H_p = 6.2 T at ambient pressure. Orbital limit H_{orb} is due to the interference of vortex core, which becomes larger at high fields. If both limits are present, the resulting upper critical limit is $H_{c2} = H_{orb}/\sqrt{1+\alpha^2}$, where Maki parameter $\alpha = \sqrt{2}H_{orb}/H_p$ [47]. As a result, the calculated H_{c2} is 3.3 (1.4) T for H‖ab(c) orientation. As this is lower than the observed upper critical field, the authors argued the possibility of p-wave superconductor. However, as discussed in Chap.IV, with strong spin-orbit coupling, H_p could be enhanced by a factor of 2 or more. Thus, discussing the Cooper pairing by the absence of Pauli limit needs special care.

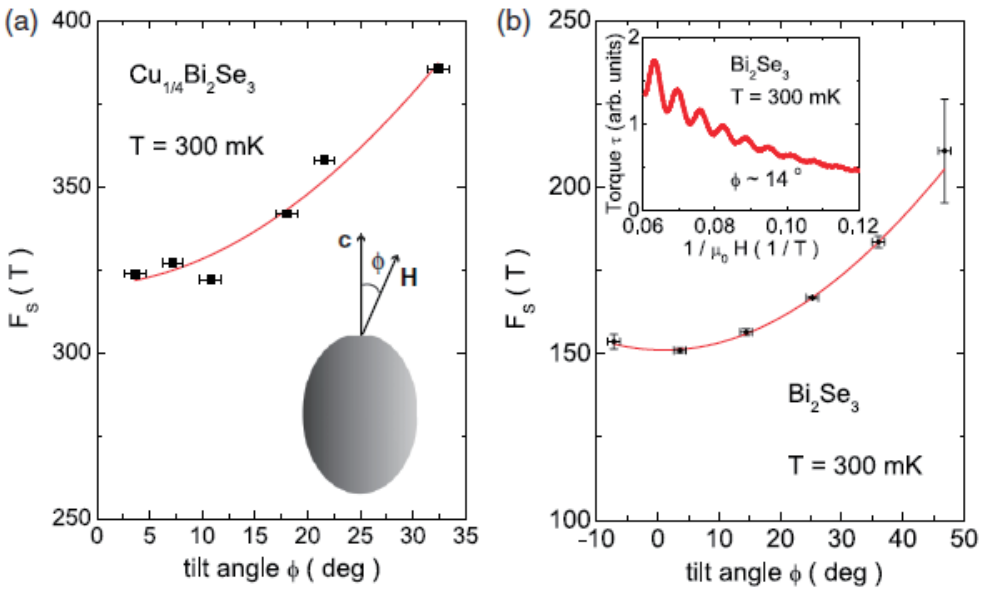

Figure 3.4: **Angular dependence of dHvA quantum oscillations in Cu-doped Bi_2Se_3 and bulk Bi_2Se_3 .** (a) Cu-doped Bi_2Se_3 with higher oscillation frequencies. (inset) The definition of magnetic field orientation. (b) Bulk Bi_2Se_3. (inset) Example torque curve at $T = 0.3$ K. Adapted from ref.[42].

Checking the criterion (b) is more straightforward. Leading experimental tools are quantum oscillation and ARPES. The first ARPES result was reported by Wray *et al.* as mentioned above [42]. One Fermi pocket was observed at Γ point. The first quantum oscillation study on $Cu_xBi_2Se_3$ was reported by our group in 2012 [48]. Fig. 3.4 shows the angular dependence of dHvA quantum oscillation frequencies for Cu-doped and bulk Bi_2Se_3. Due to the doping effect, the bulk conduction Fermi pocket becomes larger, resulting in the larger oscillation frequency in the doped sample. Since only one frequency was resolved, together with ARPES results, there should be only one Fermi pocket at Γ point. Also, the angular dependence can be fit by the ellipsoidal Fermi surface model. If this is the case, the Fermi surface only encloses one TRI momenta, Γ point, thus the criterion (b) is satisfied. As the Fermi surface is ellipsoidal, this case is called 3D topological superconductor. Also, the authors claimed that the calculated Fermi velocity v_F is almost identical between the doped and non-doped samples, indicating the linear Dirac dispersion.

However, in 2013 Lahoud *et al.* reported that the Fermi surface of $Cu_xBi_2Se_3$ could be quasi-2D rather than 3D [49]. The SdH quantum oscillation data is shown in Fig. 3.5. In Fig.3.5 (c) the angular dependence of oscillation frequency for different doping level is plotted. When the doping level is below n $10^{19}/cm^3$, the curve can be well fit by the 3D ellipsoidal model. However, the sample with n≈$10^{20}/cm^3$ rather shows quasi-2D curve. If this is the case, the Fermi surface contains two TRI momenta, Γ and Z points. If so, the system is no longer a 3D TSC, but rather a 2D-like weak TSC. In the same paper, they observed the similar evolution of Fermi surface by ARPES, concluding that the topology of Fermi surface depends on the doping level.

Similar results were reported by our group by dHvA quantum oscillation study[50]. The angular dependence of quantum oscillation is shown in Fig. 3.6. Ellipsoidal fits given by $F(\phi) = F_0(cos^2\phi + \left(\frac{k_F^x}{k_F^z}\right)^2 sin^2\phi)^{-\frac{1}{2}}$ are shown by dashed lines. For many of them, the quantum oscillations were observed up to 90 degrees and the behavior can

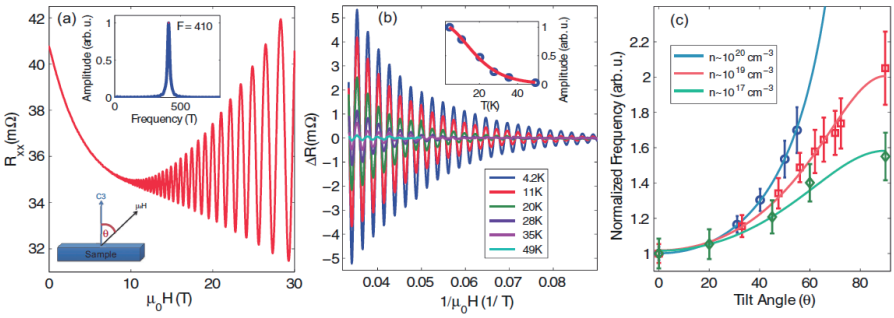

Figure 3.5: **Angular dependence of SdH quantum oscillations up to high angles in Cu-doped Bi_2Se_3.** (a) Example Resistance vs magnetic field curve showing SdH oscillation. (inset) FFT data obtained from the same curve. (b) Temperature dependence of oscillation after background subtraction. (inset) Temperature dependence of FFT amplitude. (c) Angular dependence of oscillation frequencies, indicating the 2D Fermi surface for the highly doped sample. Adapted from ref.[49].

be well explained by the ellipsoidal model. However, for some of them, the quantum oscillation could be observed only up to below 60 degrees, and the calculated k_F^z by the ellipsoidal model is 4.69 nm^{-1} which is larger than the Brillouin zone height of 3.28 nm^{-1}. Thus, it is very likely that the Fermi surface bottom and top are connected and encloses a Γ point.

There is another evidence that suggests the existence of the topological superconducting state. Point-contact spectroscopy measurements showed a zero-bias conductance peak [51] (shown in Fig. 3.7). In Fig. 3.7(a) and (b), within the superconducting gap, dI/dV curves show a clear peak around zero bias. This indicates the signature of Andreev bound states in the surface, which is consistent with the existence of surface Majorana fermions as explained later by theories [52, 53]. This result motivated researchers to further study this system.

However, the scanning tunneling microscopy spectrum [54] is shown in Fig. 3.8. Based on the shape of the spectra, the curve can be well explained by the s-wave BCS model. Moreover, the zero-bias conductance peak observed in the point contact spectroscopy completely vanished in the tunneling spectrum (Fig. 3.8(b) and (d)). The

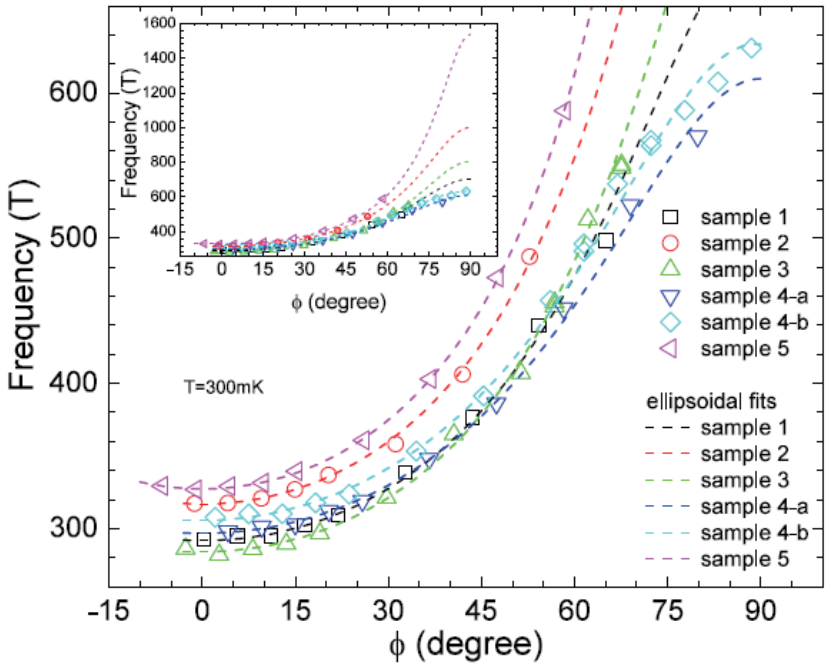

Figure 3.6: **Angular dependence of dHvA quantum oscillations up to high angles in Cu-doped Bi_2Se_3.** Some of the samples with higher doping level show open Fermi surface behavior. Adapted from ref.[50].

zero-bias peak was observed only when the tip is crashed into the sample, resulting from Josephson tunneling as shown in Fig. 3.8 (c).

Very recently, the zero-bias conductance peak (ZBCP) was observed by scanning tunneling microscopy (STM) in Cu-doped Bi_2Se_3 [55]. Fig. 3.9 shows the STM dI/dV spectra at the vortex core center and the surrounding region. The spectra taken along with two cuts (indicated in (a)) are shown in Fig. 3.9 (d) (cut 1)and (e) (cut 2). Green numbers indicate the distance from the vortex core. As shown in red, at around the vortex core the ZBCP was observed, where the ordinary superconducting spectra were observed in the surrounding region. Fig. 3.9 (f) shows the magnetic field dependence of the superconducting gap (surrounding region, blue) and the ZBCP (vortex core, red). The suppression of ZBCP was observed at high fields, which is consistent with the existence of Majorana mode observed in Bi_2Se_3 thin films grown on $NbSe_2$ substrate [56]. Also, the authors reported the nematicity in the superconducting state

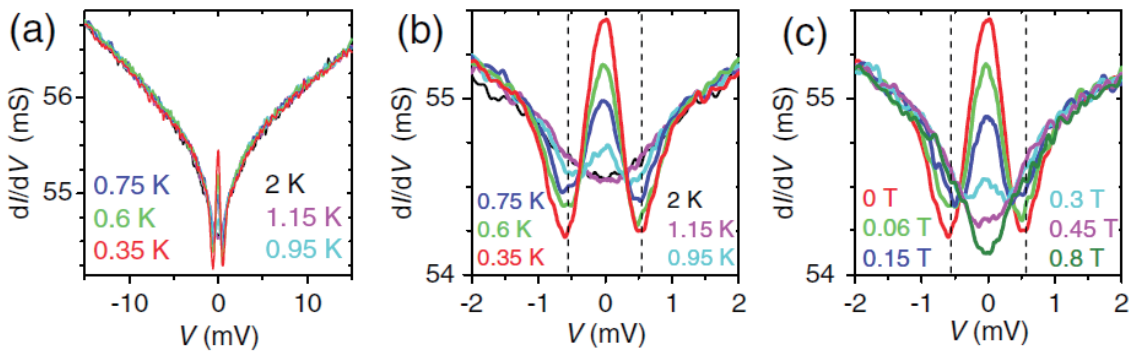

Figure 3.7: **Zero-bias conductance peak measured by point contact spectroscopy in Cu-doped Bi_2Se_3.** (a) Point-contact spectrum at different temperatures. (b) Narrower range of (a). (c) The magnetic field dependence of point-contact spectrum at T = 0.35 K. Adapted from ref.[51].

which is described in detail in the next section.

In addition, recently ZBCP was also observed in Nb-doped Bi_2Se_3 using the Andreev reflection spectroscopy device[57]. These results shed light again on the Majorana mode in doped Bi_2Se_3 series.

3.1.1.2 A nematic superconductivity

More recently, many groups have reported the signature of the exotic feature, a nematic order, in the superconducting state in Cu, Sr and Nb-doped Bi_2Se_3. The first report was Knight shift measurement by NMR [58]. Fig. 3.10 shows the temperature dependence of knight shift drop with the different magnetic field orientation. When the field is applied parallel to a or c-axis, the knight shift drops below T_c, which is consistent with the spin-singlet paring. However, when the field is applied to [110] direction, no Knight shift drop was observed, which indicates the spin-triplet paring. The angular dependence of Knight shift drop in the basal plane is shown in Fig. 3.11. The observed two-fold symmetry in spite of the three-fold symmetric crystal structure indicates the spin-rotational symmetry breaking in the superconducting state. Furthermore, above T_c, the Knight shift becomes temperature-independent,

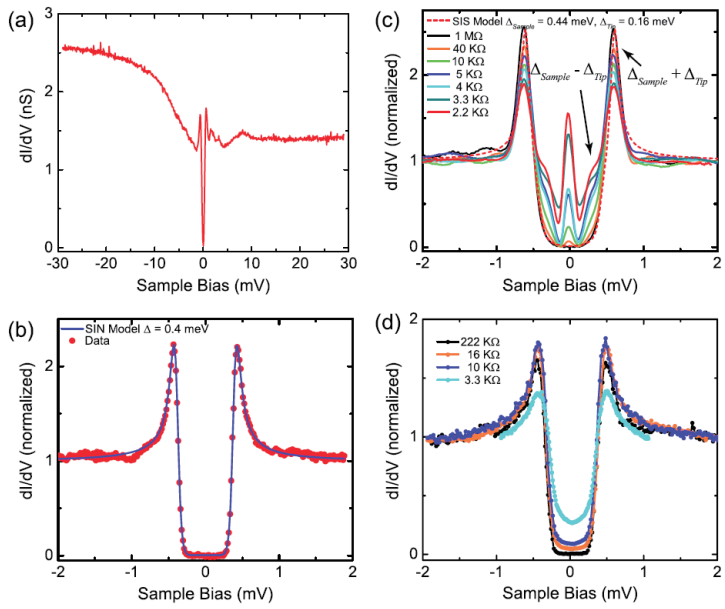

Figure 3.8: **STM spectrum on Cu-doped Bi_2Se_3.** (a) STM spectrum on Cu-doped Bi_2Se_3 with background contribution. (b) Narrower range of (a) showing superconducting gap. (c) STM spectrum with the tunneling tip crashed into the surface of the sample.(d) STM spectrum from another sample with different impedance. Adapted from ref.[54].

indicating that the rotational symmetry is broken only in the superconducting state. The simple interpretation is that the pairing symmetry is spin-triplet odd-parity, but the angular momentum of spin is pinned to certain crystal axis.

Slightly after the Knight shift report, a specific heat measurement of $Cu_xBi_2Se_3$ under magnetic fields was also found to show two-fold rotational symmetry breaking [59]. Fig. 3.12 (top) shows the angular dependence of specific heat change under magnetic fields. At 0.3 T, the system is in the superconducting state, and the specific heat shows clear two-fold symmetry. At 3 T, which is well above the critical field, the specific heat becomes almost independent of magnetic field orientation. Rotational symmetry breaking was also observed in the upper critical field, as shown in Fig. 3.12 (bottom). These results indicate that the superconducting gap function also has two-fold symmetry.

The same rotational symmetry breaking was also observed in similar compounds,

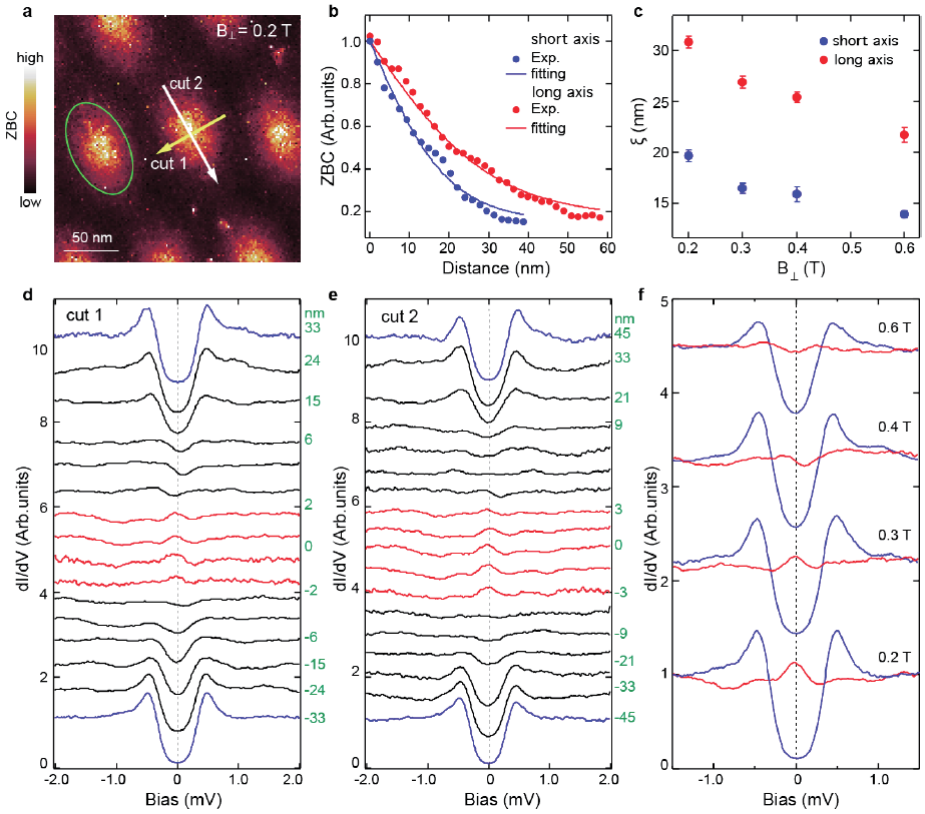

Figure 3.9: **Zero-bias conductance peak measured by STM in Cu-doped Bi_2Se_3.** (a) Vortex core image by STM. (b) Zero-bias conductance as a function of the distance from the vortex center. (c) Field dependence of coherence length ξ. (d)(e) dI/dV spectra with different distance from the vortex core along two different directions shown in (a). (f) Magnetic field dependence of dI/dV spectrum along two directions. Adapted from ref.[55].

as mentioned in the latter sections. In particular, in this study, we focused deeply on Nb-doped Bi_2Se_3. The details of our rotational symmetry breaking measurement as well as its potential origin will be discussed in Chapter **??**.

Also, as mentioned above, Tao *et al.* observed the anisotropic superconducting gap by STM [55]. The dI/dV spectra with different magnetic field orientations are shown in Fig. 3.13(a) (B =0.5 T) and (c) (B = 1.0 T), respectively. As shown, the superconducting gap size is clearly angular-dependent. Angular dependence of the gap size is shown in (b)(d), where two-fold symmetry is observed.

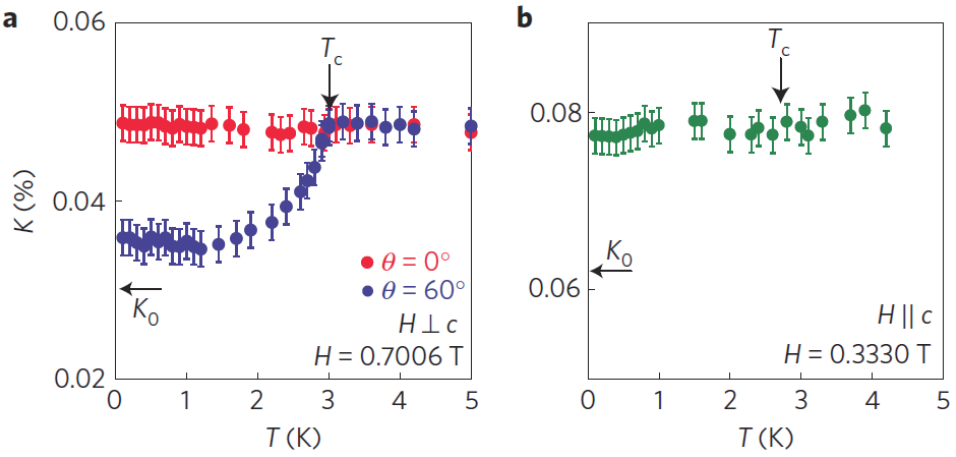

Figure 3.10: **Knight shift in Cu-doped Bi_2Se_3 showing in-plane anisotropy.** (a) Temperature dependence of In-plane Knight shift. (b) Temperature dependence of Knight shift with magnetic field applied parallel to c-axis. Adapted from ref.[58].

Stimulated by the observation of rotational symmetry breaking in the Knight shift [58], Fu further investigated the possible superconducting pairing symmetry in this system [60]. Before this theory, as mentioned in Chap. I, Fu and Berg predicted that the odd parity superconductors with odd TRI momenta possess the topological superconducting state [13]. In the same paper, it is argued that among four possible pairing potentials Δ_1-Δ_4 (table 3.1), only Δ_2 shows the odd parity with a full gap. The pairing potentials Δ_1-Δ_4 also correspond to one the representation of the D_{3d} point group of the crystal structure, so in this case, A_{1u} representation has been intensively focused on.

Table 3.1: Pair pottential proposed for doped Bi_2Se_3. Adapted from [20].

Pair potential	Representation	Parity	Spin	Energy gap
$\Delta_1 = i\Delta_0 s_y$	A_{1g}	Even	Singlet	Isotropic full gap
$\Delta_2 = i\Delta_0 \sigma_y s_z s_y$	A_{1u}	Odd	Triplet	Anisotropic full gap
$\Delta_3 = i\Delta_0 \sigma_z s_y$	A_{2u}	Odd	Singlet	Point nodes at poles, orbital triplet
$\Delta_4 = i\Delta_0 \sigma_y s_x s_y$	E	Odd	Triplet	Point nodes (Δ_{4x}) or gap minima on the equator (Δ_{4y})

Fu's new theory [60] took into account the hexagonal warping term in the Hamilto-

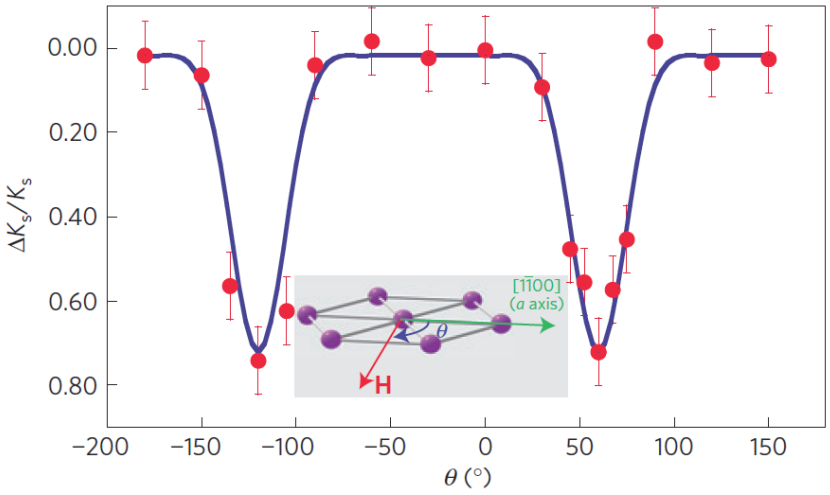

Figure 3.11: **In-plane ngular dependence of Knight shift drop in Cu-doped Bi_2Se_3.** (a) No Knight shift was observed expect for the magnetic field direction parallel to certain crystal axis, showing two-fold symmetry. Adapted from ref.[58].

nian, resulting in the full superconducting gap with spontaneous rotational symmetry breaking in the Δ_4 pairing. This is because, among Δ_1-Δ_4, only Δ_4 is multidimensional and thus could be nematic. We briefly follow Fu's proof in [60] here.

First, consider the model Hamiltonian of $Cu_xBi_2Se_3$ with fully rotationally invariant as

$$H_0 = \sum_k c_k^\dagger \left[v(k_x s_y - k_y s_x)\sigma_x + v_z k_z \sigma_y + m\sigma_x - \mu \right] c_k, \tag{3.1}$$

where the chemical potential μ is in the conduction band due to the Cu doping. Additionally, in the Δ_4 ($=E_u$) pairing, the spin-triplet pair has a in-plane zero-total spin along the direction $n = (n_x, n_y)$, which is defined as a nematic vector. Then, the pair potential V_n is given by $V_n = n_x V_x + n_y V_y$, where $V_x = i\Delta_0(c_{1\uparrow}^\dagger c_{2\uparrow}^\dagger - c_{1\downarrow}^\dagger c_{2\downarrow}^\dagger)$ and $V_y = \Delta_0(c_{1\uparrow}^\dagger c_{2\uparrow}^\dagger + c_{1\downarrow}^\dagger c_{2\downarrow}^\dagger)$.

The superconducting gap $\delta_n(k)$ is obtained by diagonalizing the Hamiltonian $H_{SC} = H_0 + V_n$, resulting in $\delta_n = \Delta\sqrt{\tilde{k}_z^2 + (\tilde{k}\cdot n)^2}$, where $\Delta = \Delta_0\sqrt{1 - m^2/\mu^2}$ and $\tilde{k} = (vk_x, vk_y, v_z k_z)/\sqrt{\mu^2 - m^2}$. Thus, the superconducting gap has two point nodes if $k_z = 0$ and $\tilde{k}$ is perpendicular to n.

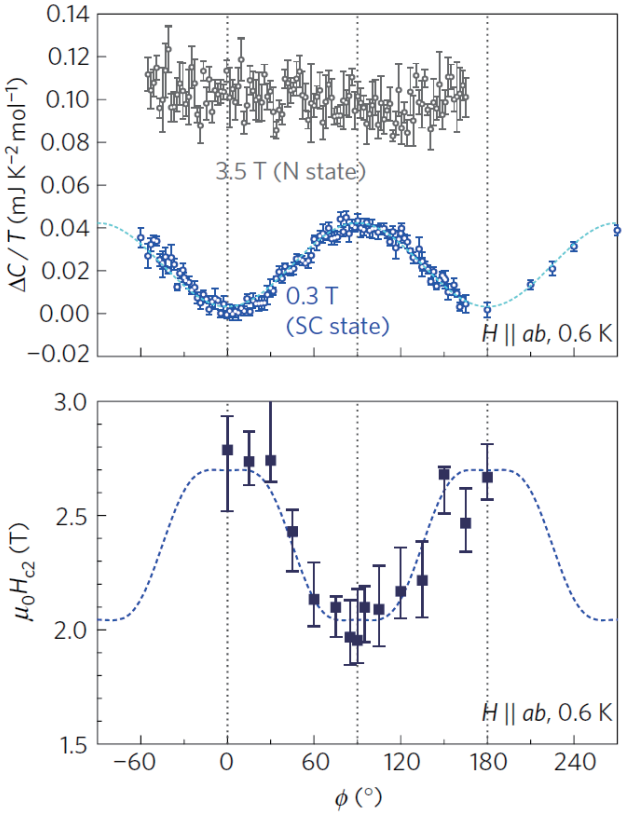

Figure 3.12: **Anisotropy observed in specific heat measurement in Cu-doped Bi_2Se_3.** (top) In-plane angular dependence of specific heat for the normal state and the superconducting state (bottom) In-plane angular dependence of the modulation of the upper critical field H_{c2} determined from specific heat. Adapted from ref.[59].

However, since the Hamiltonian is fully rotationally invariant, it does not reflect the crystal structure of the material. Thus, Fu further added the hexagonal warping term to represent the Hamiltonian in doped Bi_2 Se_3. The new Hamiltonian H is given by

$$H = H_0 + \lambda \sum_k (k_+^3 + k_-^3) c_k^\dagger \sigma_z s_z c_k \tag{3.2}$$

where $k_\pm = k_x \pm i k_y$. After diagonalizing the Hamiltonian $H_{SC} = H + V_n$, we obtain the superconducting gap $\delta_n = \Delta\sqrt{1 - [\tilde{k} \cdot (z \times n)]^2}$, where k satisfies the Fermi surface condition $\mu = \sqrt{m^2 + v^2(k_x^2 + k_y^2) + \lambda^2(k_+^3 + k_-^3)^2 + v_z^2 k_z^2}$. Thus, the super-

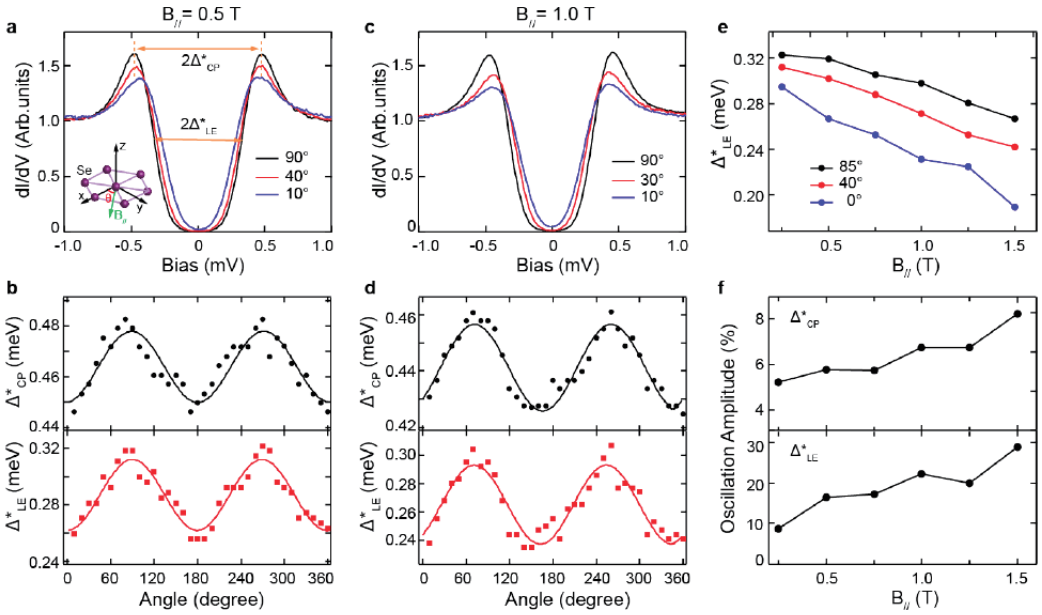

Figure 3.13: **Anisotorpic superconcucting gap observed by STM in Cu-doped Bi_2Se_3.** (a) dI/dV spectra for different magnetic field orientations at H=0.5 T. (b) Angular dependence of the superconducting gap at 0.5 T. (a). (c)(d) The same plot as (a)(b) except for the applied magnetic field of 1 T. (e)Magnetic field dependence of the superconducting gap size with different field orientations.(f) Magnetic field dependence of oscillation amplitudes of the superconduting gap. Adapted from ref.[55].

conducting gap δ_n has a node if

$$1 = |\tilde{k} \cdot (z \times n)| = |n \cdot (\tilde{k} \times z)|. \tag{3.3}$$

For $K_z = 0$, from the Fermi surface condition, this is met only when $k_+^3 + k_-^3 = 0$ (which is satisfied when k is parallel to the crystal axis) and $n \parallel k$.

Now, the Δ_4 pairing splits into two cases. When n vector (or nematic vector) is parallel to the crystal axis, there is point node and the order parameter is called Δ_{4x}. If the nematic vector is parallel to the mirror plane (i.e. perpendicular to the crystal axis), there is no node in the superconducting gap, and the order parameter is called Δ_{4y}.

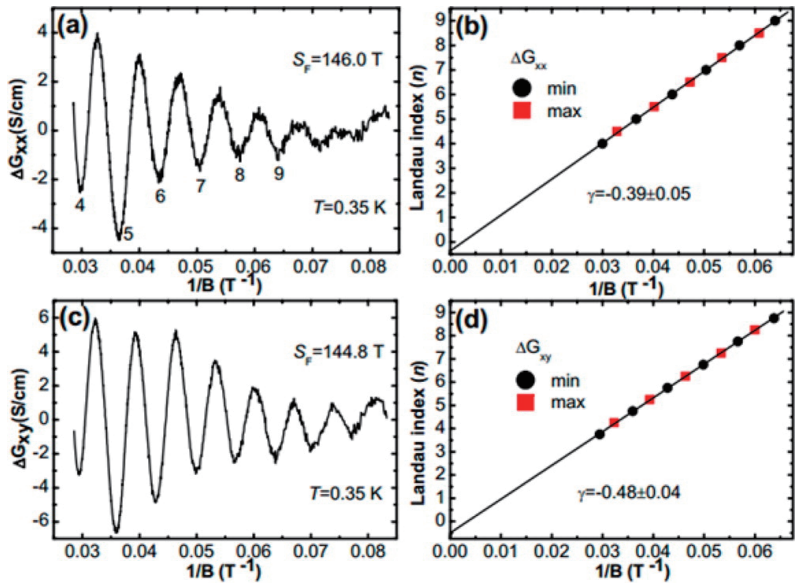

Figure 3.14: **SdH quantum oscillation study on $Sr_xBi_2Se_3$.** (a) Example curve of oscillations in the longitudinal conductance. (b) Landau fan plot obtained from (a), showing Berry phase close to half-integer. (c)(d) The same plot as (a)(b) for the transverse conductance. Adapted from ref. [61]

3.1.2 Sr-doped Bi_2Se_3

Since the discovery of superconducting $Cu_xBi_2Se_3$ in 2010, this system has been studied intensively. However, newer doped Bi_2Se_3 systems, namely Sr- [61] and Nb-Bi_2Se_3, have their own advantages and have been attracting growing interest. First, $Cu_xBi_2Se_3$ is intrinsically not a clean system. The highest volume fraction is 50%, and due to the dirty cleaved surface, it is difficult for STM to fully understand the superconducting nature. Also, the system is known to be air-sensitive, thus preparing and storing the sample always require special care. Since the sample quality highly depends on the growth condition, the nature of $Cu_xBi_2Se_3$ has not been concluded yet.

The first $Sr_xBi_2Se_3$ was reported in 2015 [61], with x= 0.06, T_c = 2.5 K and the superconducting volume fraction of 90%, which is much higher than that of Cu-doped samples and confirms the bulk superconductivity. Later high volume fraction

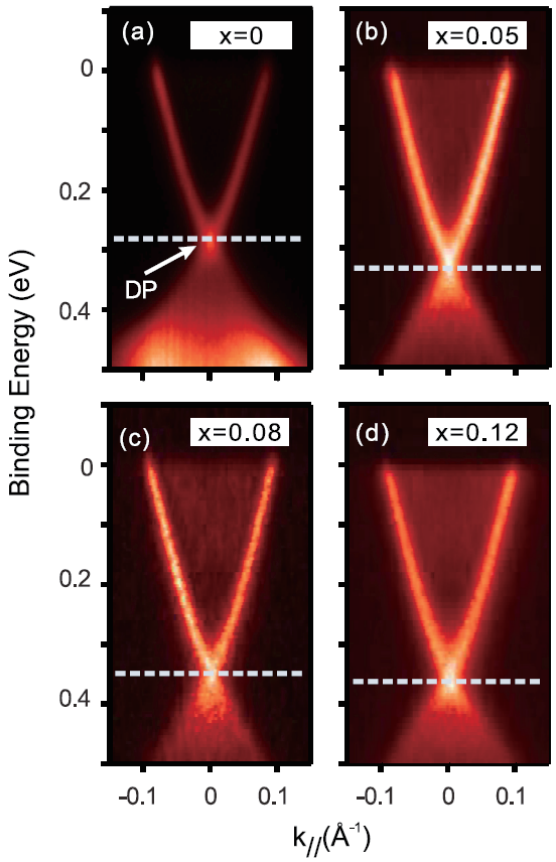

Figure 3.15: **ARPES data on $Sr_xBi_2Se_3$.** (a) Bulk data with doping level x = 0. (b) x= 0.05 (c) x= 0.08 (d) x = 0.12. Adapted from ref. [61]

was also confirmed by muon spin rotation experiments [62]. Slightly higher T_c of 2.9 K was reported when x=0.1 by Shruti et all [63], in which the samples are well characterized by transport and magnetization study. Also, the sample is reported to be more robust against air exposure than Cu-doped one. Thus, it is easier to study the Sr-doped system. Moreover, the carrier density n $\cong 2 \times 10^{19}/\text{cm}^{-3}$ was reported, which is much smaller than that of Cu-doped one [61]. Thus, the Fermi level is closer to the Dirac point, and the effect of topological nature is expected to be stronger.

The topological nature was observed by the half-integer Berry phase extracted from SdH measurement [61], followed by the ARPES [64, 65] that confirmed the existence of the surface state. Fig. 3.14(a)(c) shows the SdH quantum oscillations from longitudinal and transverse conductance after background subtraction at $T =$

0.35 K up to 35 T. The Landau fan plot is shown in Fig. 3.14 (b)(d). The Berry phase γ could be obtained by the linear fitting

$$n = F/B + \gamma \tag{3.4}$$

where F (T) is the frequency of oscillations. From linear fitting, the obtained Berry phase is close to 0.5, indicating the existence of Dirac fermions.

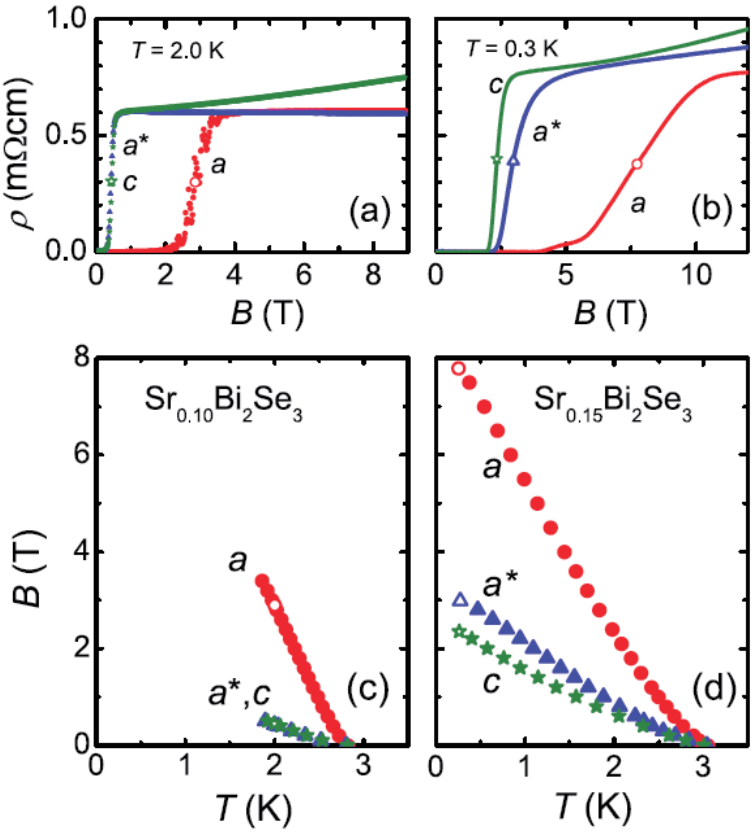

Figure 3.16: **In-plane anisotropy of the upper critical field H_{c2} in $Sr_xBi_2Se_3$.** (a) Magnetic field dependence of resistivity with different field orientation ($H \parallel a, a^*$ and c) at $T = 2$ K. (b) The same plot as (a) at $T = 0.3$ K. (c) Upper critical field vs temperature plot for different field orientations for doping level x = 0.1. (d) The same plot as (c) for x = 0.15. Adapted from ref. [66]

Fig. 3.15 shows the Low energy ARPES spectra with different doping level. The Dirac-like surface state remains from the bulk (a) up to x=0.12 doping (d). The

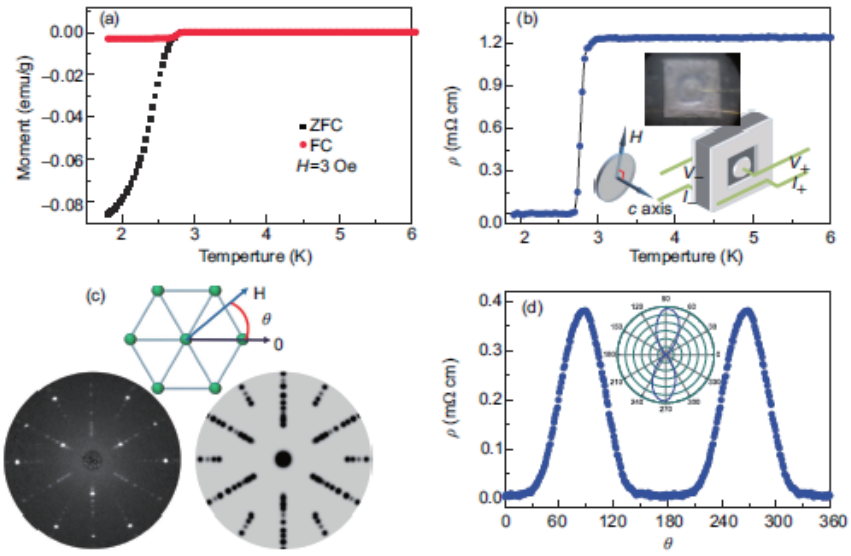

Figure 3.17: **Two-fold symmetry of magnetoresistance in the superconducting state of $Sr_xBi_2Se_3$ with Corbino setu.** (a) Temperature dependence of magnetic susceptibility. (b) The temperature dependence of resistivity showing T_c 2.9 K. (inset) Corbino setup (c) Crystal orientation determined from Laue diffraction pattern. (d) Angular dependence of magnetoresistance in the superconducting state at T = 1.9 K and H = 0.5 T. Adapted from ref. [67]

Dirac point lays at the binding energy of 290 meV below the Fermi level (x=0) and becomes lower at higher doping. This trend is consistent with the bulk carrier density obtained by the Hall measurement [61, 63]

The nematic order was observed in $Sr_xBi_2Se_3$ as well. The first observation of rotational symmetry breaking was reported by measuring the anisotropy of the upper critical field by electronic transport [66]. Fig. 3.16 (c)(d)shows the upper critical field vs temperature with different field orientations. While the critical field value H_{c2} is almost the same when the field is applied parallel to c or a* (which is perpendicular to a) axis, H_{c2} is almost three times larger. Indeed, the anisotropy of critical field H^a_{c2}/H^{a*}_{c2} for other doped Bi_2Se_3 is less than two, which is much smaller than Sr-doped one. This makes $Sr_xBi_2Se_3$ more interesting.

There is a possibility, however, that the anisotropy is induced by the electric field

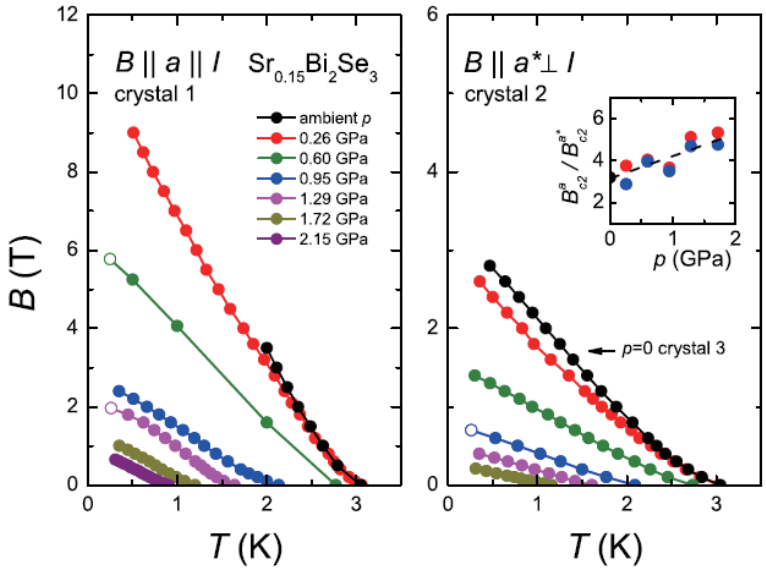

Figure 3.18: **Temperature dependence of upper critical field H_{c2} at different pressures in $Sr_{0.15}Bi_2Se_3$.** (left) Magnetic field is applied parallel to the crystal axis. (right) Magnetic field is applied perpendicular to the crystal axis (parallel to the mirror plane). Adapted from ref. [68].

as it intrinsically breaks the rotational symmetry. To exclude this possibility, Du *et al.* tested the angular dependence of critical field H_{c2} using a Corbino-shape setup [67]. The inset of Fig. 3.17 (b) shows the Corbino ring setup. In this configuration, the electric current flow is isotropic, so the rotational symmetry is not broken by the current. Though, as shown in Fig. 3.17 (d), the strong anisotropy of H_{c2} was still observed. The author also reported, however, that the nematic axis could be either parallel or perpendicular to the crystal axis. Thus, the origin of the nematicity has to be carefully studied.

The large in-plane anisotropy of the upper critical field was observed under pressure as well, further suggesting the multicomponent order parameter [68]. In Fig. 3.18, the critical field vs temperature with different magnetic field orientations is plotted. Indeed, at $T = 0.3$ K, the anisotropy of critical field H^a_{c2}/H^{a*}_{c2} =5 under high pressure (2.2 GPa), which is even enhanced from 3.2 at the ambient pressure.

Prior to this work, the reentrant superconducting state under very high pressure

was reported [69]. The high pressure was achieved by a screw-pressure-type diamond anvil cell. The temperature dependence of resistance under different pressure. is shown in Fig.3.19. At low pressure, the superconductivity is suppressed, but above 6 GPa the sample becomes superconducting again with higher T_c of 5 K, then T_c becomes even higher above 15 GPa. They also tested the X-ray diffraction measurement at high pressure. The ambient rhombohedral phase ($R-3m$) is persistent up to 5.7 GPa, above which a monoclinic phase ($C2/m$) starts to appear followed by the tetragonal phase ($I4/mmm$) above 25 GPa. The similar structural transition from rhombohedral to monoclinic was also observed in the bulk Bi_2Se_3.

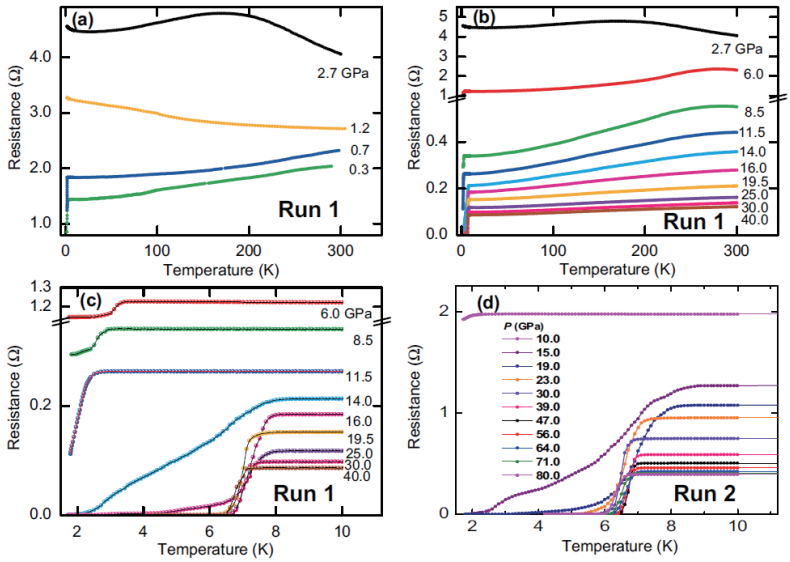

Figure 3.19: **Temperature dependence of resistance at different pressures in $Sr_{0.15}Bi_2Se_3$, showing the reentrant superconducting state.** (a) Low-pressure region. (b) High-pressure region. (c) Narrowed range showin in (b) to show the reentrant superconducting state at high pressures. (d) The second run with the maximum pressure of 80 GPa. Adapted from ref. [69].

However, more recently Manikandan *et al.* reported the pressure study on $SR_xBi_2Se_3$ suggesting the possibility of conventional superconductivity [70], as the pressure dependence of superconductivity is well explained by the conventional superconductors. Also, they did not observe the reentrant superconducting state under high pressure

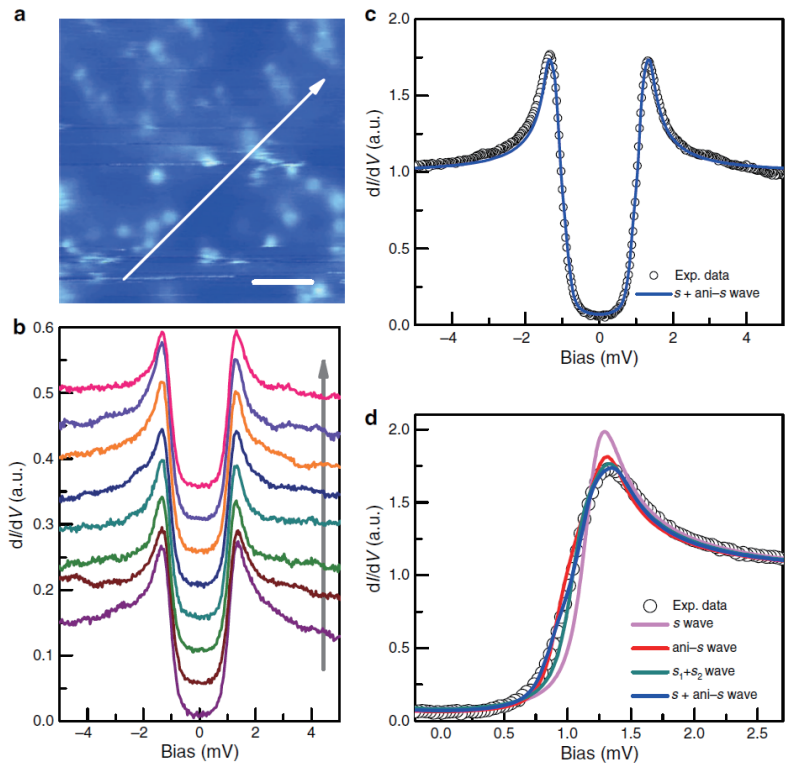

Figure 3.20: **Anisotropic superconducting gap of $Sr_xBi_2Se_3$.** (a) The STM image of $Sr_xBi_2Se_3$. (b) The STM spectra takan along with the arrow indicated in (a). (c) Averaged STM spectrum shown in (b). (d) Fitting of dI/dV spectrum by different modeling types. Adapted from ref. [71].

(up to 8 GPa) observed in ref. [69]. They argue that this is possibly because of the Sr atom concentration difference, but also claims that the hydrostatic pressure result is more reliable than that from diamond anvil cell.

From STM, the superconducting gap is observed to be slightly anisotropic [71]. Fig. 3.20(b) shows the spatially resolved tunneling spectra along the arrowed line shown in (a). The data was taken at $T = 0.4$ K and I_t=102 pA. As shown, the gap structure is slightly anisotropic. The averaged spectrum shown in (b) is plotted in Fig.3.20 (c). From theoretical fitting, the spectra are well fit by the double gaps (s + anisotropic s). This could be the origin of rotational symmetry breaking observed in doped Bi_2Se_3 series rather than the triplet paring. However, the authors also argued that the possibility of two-fold gap functions cannot be ruled out. Also, notably

no zero-bias conductance peak from the surface Andreev bound state was observed, which is consistent with the result from Cu-doped one [54]. This is not consistent with the theoretical prediction for 3D TSCs [52, 53], suggesting that the behavior cannot be explained by bulk TSC theory.

Finally, the thin film of $Sr_xBi_2Se_3$ was grown on $SrTiO_3$ (111) substrate using molecular beam epitaxy (MBE) [72]. Authors report that while the carrier density of the thin film is similar to that of the bulk crystal, no superconductivity was observed, indicating that the superconductivity of bulk samples may arise from the crystal structure of bulk modified by doping.

3.1.3 Nb-doped Bi_2Se_3

While $Nb_xBi_2Se_3$ is the newest member of doped Bi_2Se_3 family, it has been attracting growing interest these days. The first report of this material is reported by Qiu *et al.* [73]. The basic physical properties are shown in Fig.3.21. The same as other doped Bi_2Se_3, Nb atoms are intercalated within atomic layers of Bi or Se. The ARPES data is shown in (c), confirming the existence of a Dirac point. The Dirac point as well as the bulk conduction band Fermi pocket was observed around the Γ point, similar to bulk and doped Bi_2Se_3. A critical temperature T_c of 3.6 K is also similar to other series as shown in (e). In addition, the measured volume fraction was close to 100%, which is much larger than Cu-doped one and similar to Sr-doped samples, making this compound more attractive.

Despite that Nb-doped Bi_2Se_3 is very similar to the other doped Bi_2Se_3, Nb ions also show magnetic moment. In Ref. [73], the authors claim the magnetic ordering at low temperatures. However, no magnetic ordering has been observed down to T_c in the later report [74].

Soon after the discovery of superconducting $Nb_xBi_2Se_3$, a dHvA quantum oscillation study was reported by our group [75]. The angular dependence of oscillation

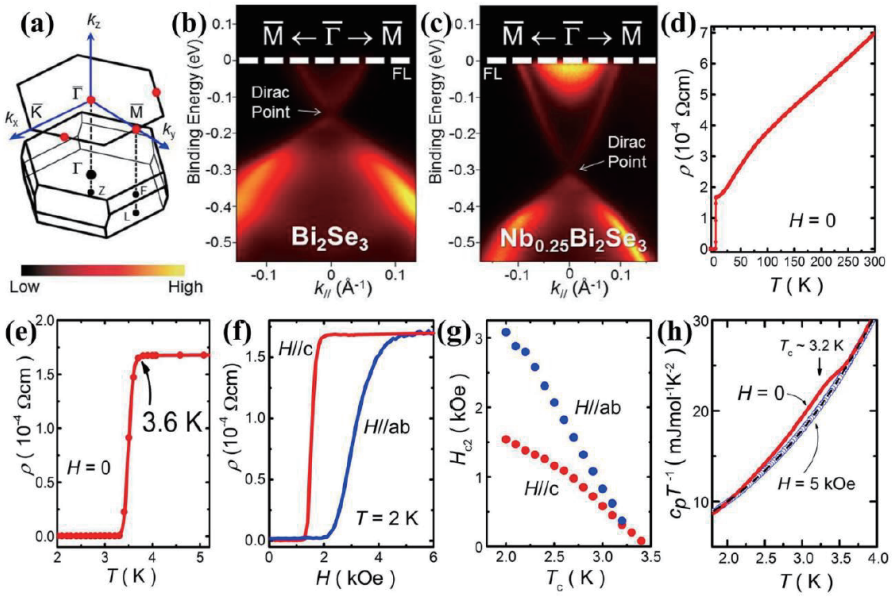

Figure 3.21: **ARPES adn other physical properties of $Nb_xBi_2Se_3$.** (a) The bulk Brillouin zone of Bi_2Se_3 crystals. (b)(c) ARPES data for a Bi_2Se_3 and $Nb_{0.25}Bi_2Se_3$ crystals, respectively. (d) Temperature dependence of resistivity from 2 K to 300 K. (e) Narrowed range of (d) around the superconducting transition. (f) Magnetoresistance curves with two different field orientations. (g) Temperature dependence of upper critical field H_{c2} for two field orientations. (h) Specific heat vs temperature plot. Adapted from ref. [73].

frequency from two samples is shown in Fig. 3.22. Similar to other doped Bi_2Se_3, the ellipsoidal Fermi pocket was observed, as shown by the solid fitting line. However, in sharp contrast to Cu- or Sr-doped compounds which only have one Fermi pocket around the Γ point, an additional branch was observed close to in-plane field orientation. Moreover, this branch shows the anisotropic in-plane angular dependence. It is not yet clear if the multiple frequencies originate from the multiple Fermi pockets or not. If the anisotropic frequency dependence reflects the anisotropy of the Fermi surface around the Γ point, this may indicate the origin of nematic order observed in this system. One weird thing is that the angular dependence of the second frequency does not seem to be symmetric along the plane. The details are discussed in the next chapter.

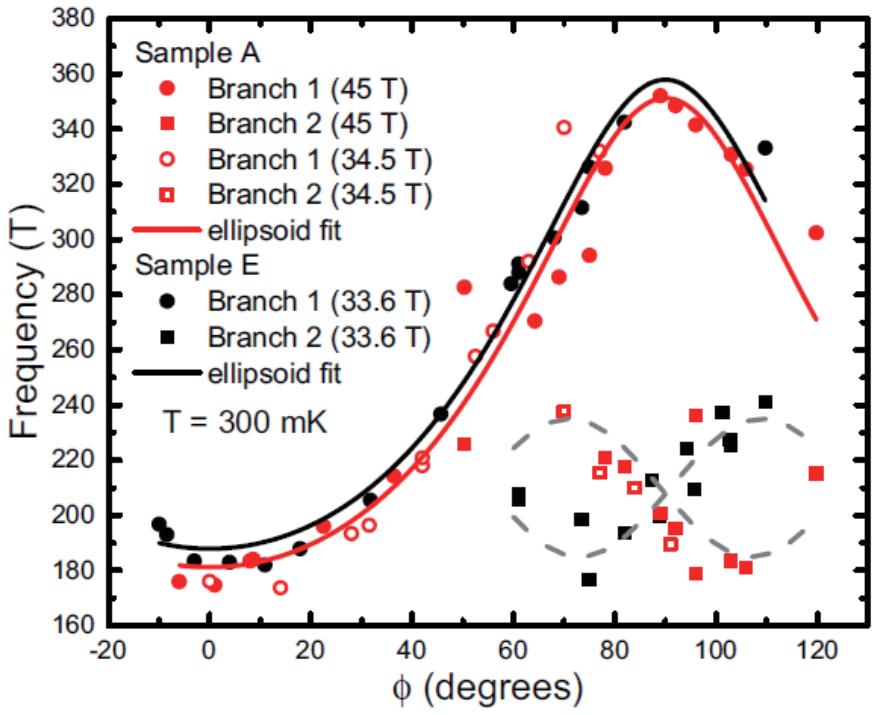

Figure 3.22: **Angular dependence of dHvA oscillation frequencies of $Nb_xBi_2Se_3$.** The data are taken at $T = 0.3$ K. The solid lines indicate the ellipsoidal fitting. Adapted from ref [75]. [73].

The first evidence of rotational symmetry breaking in $Nb_xBi_2Se_3$ was reported by our group, using torque magnetometry technique to measure the anisotropy of supercurrent and susceptibility [76]. This result is one of the main topics of this study, as described in detail in the next chapter.

Later, the nematic feature in the superconducting state of $Nb_xBi_2Se_3$ was reported by the transport measurement [74]. Similar to the report by Pan *et al.* [66], when the magnetic field is applied in-plane, the magnetoresistance shows two-fold symmetry as shown in Fig.3.23 (left) 3.23. Furthermore, by magnetization measurement, they plotted the angular dependence of upper critical field, irreversibility field and magnetization. In the right figure, solid lines are theoretical fitting [60, 77]

$$H_{c2}(\phi) = \frac{H_{c2}(0)}{\sqrt{cos^2\phi + \Gamma^2 sin^2\phi}}, \tag{3.5}$$

where Γ is a parameter.

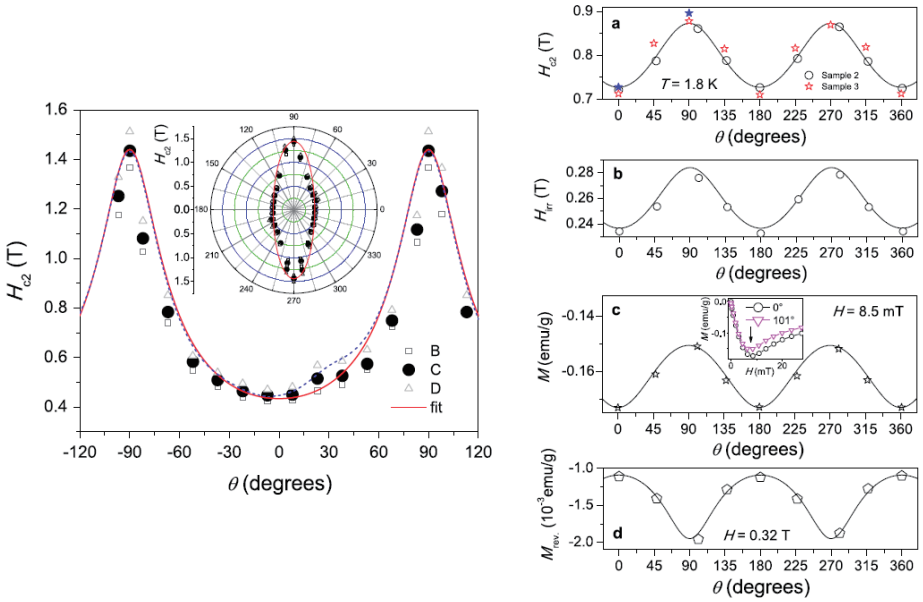

Figure 3.23: **In-plane two-fold angular dependence of upper critical field, irreversibility field and magnetization in $Nb_xBi_2Se_3$.** (left) Angular dependence of magnetoresistance at $T = 0.34$ K. B,C and D in the figure indicate when the magnetoresistance reaches 50, 75 and 90% of the normal state resistance, respectively. (right) Angular dependence of (a) upper critical field determined by magnetization, (b) irreversibility fields, (c) magnetization and (d) irreversibility field in magnetization. Adapted from ref. [74].

From the penetration depth measurement, the power-law temperature dependence of Δf was observed as shown in Fig. 3.24. If the superconducting gap is a full gap (i.e. no nodes), the temperature dependence of penetration depth should show the exponential behavior as similar to the specific heat measurement. However, the data shown in Fig. 3.24 is well fit by the parabolic fitting (red line), suggesting that the superconducting gap has a point node. This observation is consistent with the Δ_{4x} order parameter mentioned above. The data is also fit by the BCS full gap model as shown in the dashed lines, showing the clear deviations.

It is noted that there is a possibility that the lowest temperature of 0.1 T/T_c is too high to exclude the possibility of line nodes. Further experiments at a lower

temperature would be helpful to understand the superconducting ground state of this system.

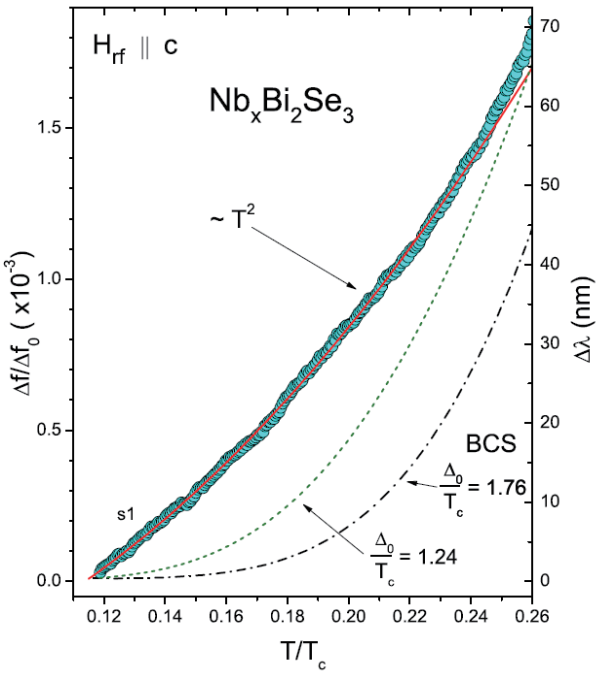

Figure 3.24: **Temperature dependence of penetration depth in $Nb_xBi_2Se_3$.** Adapted from ref. [78].

3.2 Results

In this section, I describe the details of our nematic study on Nb-doped Bi_2Se_3 by Torque magnetometry.

3.2.1 Experimental details

X-ray diffraction on single crystals was used to determine the crystal orientation. As the dopant atoms are intercalated between Bi-Se layers, the x-ray diffraction pattern from doped Bi_2Se_3 is almost identical to bulk i_2Se_3. The observed peak at 2 θ = 43.7 ^{o} corresponds to the (110) plane, determining the in-plane crystal orientation.

The free energy with respect to the external field H is given by $\mathcal{F} = \mu_0 V \vec{M} \cdot \vec{H}$.

Thus, Magnetic torque is given by the derivative of $\mathcal{F}$ with respect to the magnetic field tilt angle ϕ: $\vec{\tau}$=$\mu_0 \mathrm{V}\vec{M}\times\vec{H}$, where V is the volume of the sample, $\vec{H}$ is the external magnetic field, and $\vec{M}$ is the magnetization of the sample. Torque magnetometry is thus a thermodynamic probe that measures the free energy directly.

The sample was mounted standing up on its edge to measure the in-plane anisotropy as shown in Fig. 3.25 (A). The cantilever was rotated with respect to the magnetic field. In the most general case, the dominating term of the magnetic torque response is a periodic function of double of the azimuthal angle ϕ:

$$\tau_{2\phi} = \frac{1}{2}\mu_0 V H^2\{(\chi_{aa} - \chi_{bb})\sin 2\phi - 2\chi_{ab}\cos 2\phi\}. \tag{3.6}$$

Here $M_i = \Sigma_j \chi_{ij} H_j$. This is the case for the paramagnetic material, but for the magnetic materials, two-fold symmetry is still the most dominant if the symmetry of the crystal structure is low.

If the system has higher symmetry (e.g., cubic, tetragonal, hexagonal$\cdots$), since $\chi_{aa} = \chi_{bb}$ and $\chi_{ab} = 0$, therefore $\tau_{2\phi} = 0$. In this case, the next leading term is

$$\tau_{2n\phi} = A_{2n\phi}\sin 2n(\phi - \phi_0), \tag{3.7}$$

where n depends on the crystalline symmetry: For example, $n = 2$ for the tetragonal lattice or $n = 3$ for the hexagonal lattice. This could be understood as following. By definition, the torque becomes zero when the magnetic free energy is at the extrema. This is satisfied only when the magnetic field is applied to the symmetric axis of the crystal. Thus, the torque becomes zero every 45 degrees for tetragonal lattice, for example, resulting in $sin4\phi$ dependence. In other words, the number of zeros in the angular dependence of torque reflects the symmetry of the sample.

The rotational symmetry breaking in the normal state was detected by the torque magnetometry in tetragonal URu_2Si_2 or $BaFe_2(As_{1-x}P_x)_2$ [79, 80]. At high temper-

ature, $\sin 4\phi$ is dominant as the system is tetragonal. However, at low temperature $\sin 2\phi$ becomes dominant, indicating that the rotational symmetry is broken at low temperature.

Instead of a tetragonal lattice, Nb-doped Bi_2Se_3 has trigonal lattice, as shown in Fig. 3.25(B) which looks down the c-axis. In our experimental setup, the magnetic field is applied in the hexagonal plane to detect the in-plane anisotropy. As described above, for the paramagnetic trigonal systems in a normal state, the angular dependence of torque is expected to follow $\sin 6\phi$, with zero torque at every 30 degrees along the crystal axis or mirror plane. Here azimuthal angle, ϕ, is determined as the angle between the magnetic field and the mirror plane.

Fig.3.25(C) shows the superconducting volume of our $Nb_xBi_2Se_3$ sample close to 100 %, which is much higher than $Cu_xBi_2Se_3$ samples.

The rotational symmetry breaking measurements are done in SCM1 (Dilution fridge) and SCM 2 (Helium 3) in National High Magnetic Field Laboratory, Tallahassee. The example torque curves in the superconducting state is shown in Fig. 3.25 (D). The magnetic field dependence of torque at $T = 0.3$ K is plotted at every 30 degrees. Since the critical field of this ample at $T = 0.3$ K is around 0.6 T, 1 T is high enough to fully suppress the superconductivity and measure the normal state nature. Thus, the magnetic field is swept up from H = -1 T to 1 T, then swept back to -1 T to track the angular dependence of the superconducting hysteresis loop, which indicates that the sample is a type-II superconductor. As explained in the latter section, it is found that the symmetry of the hysteresis loop is consistent with that of the superconducting magnetic susceptibility, thus can be used to probe the rotational symmetry breaking of the superconducting state.

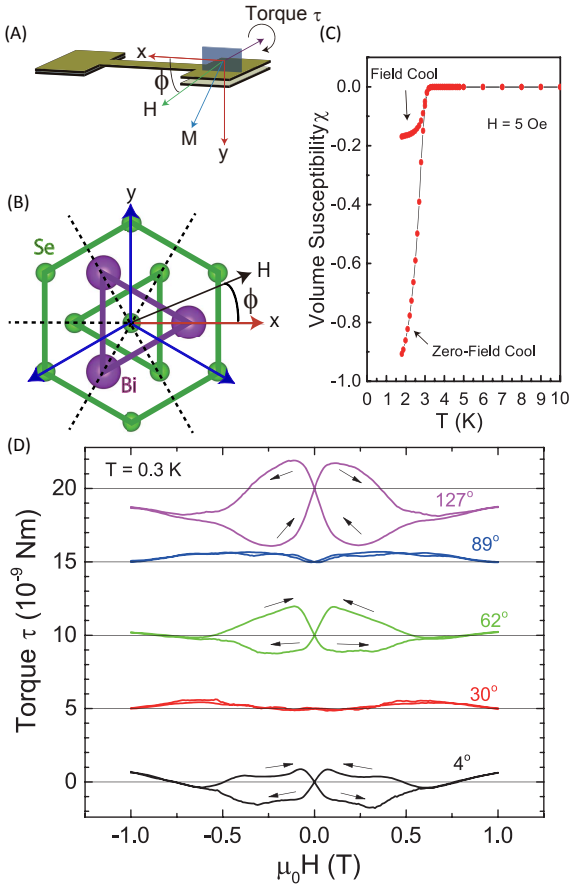

Figure 3.25: **Experimental setup and sample torque curve of $Nb_xBi_2Se_3$.** (A) Torque magnetometry setup. The magnetic field is applied in-plane to detect the anisotropy. (B) Crystal structure and field orientation. The magnetic field is applied with azimuthal angle ϕ away from the mirror plane. (C) Temperature dependence of Meissner effect, showing large superconducting volume fraction. (D) Example torque curves at every 30 degrees at $T = 0.3$ K.

3.2.2 Rotational symmetry breaking in susceptibility

To probe the symmetry of the sample in a superconducting state, we first measure the symmetry of magnetic susceptibility in both a normal state and a superconducting state. However, as we measure the anisotropy of susceptibility $\Delta\chi$ rather than the susceptibility χ itself, we define the effective susceptibility as following. First, since the torque τ is given by $\tau = M \times \mu_0 H$, $M_{\pm}$, the effective magnetization M_{eff} and the effective spontaneous magnetization ΔM_{eff} is given by

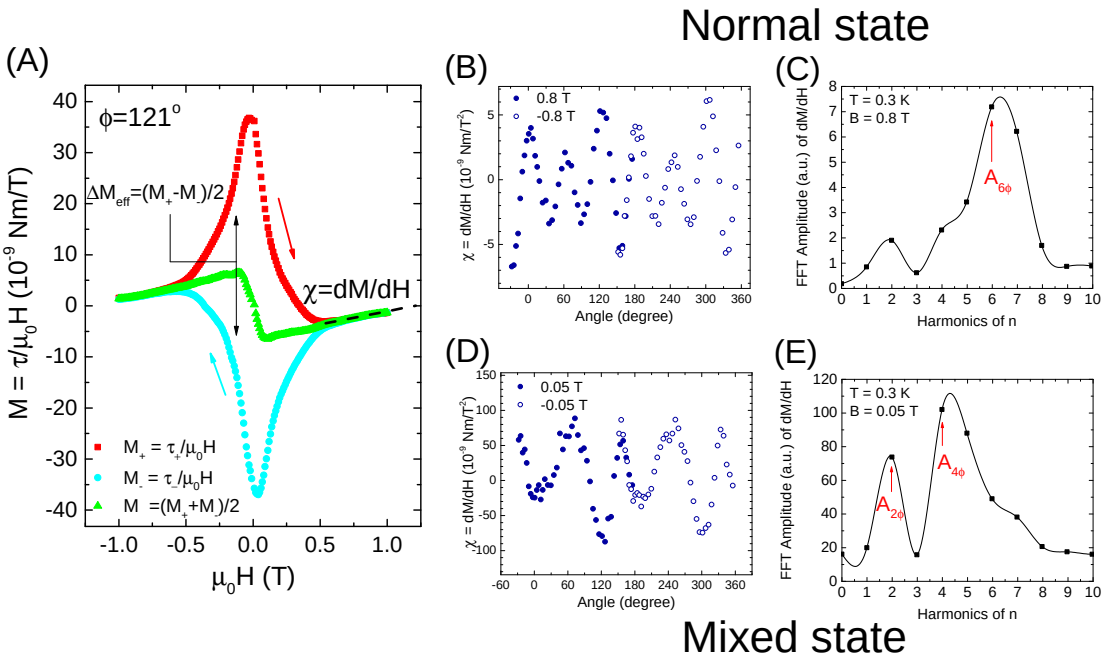

Figure 3.26: **The angular dependence of effective magnetic susceptibility of $Nb_xBi_2Se_3$ in a normal state and superconducting state.** (A) The definition of M, ΔM, and χ, which detail is explained in the main text. (B)Angular dependence of effective susceptibility χ in a normal state at 0.3 K, showing the trigonal lattice symmetry. (C) The Fast Fourier Transform (FFT) plot of data in (B). (D) Angular dependence of effective susceptibility χ in a superconducting state at 0.3 K, indicating the lower rotational symmetry compared to the normal state. (E) FFT plot of the data shown in (D).

$$M_{\pm} = \tau_{\pm}/V\mu_0 H, \tag{3.8}$$

$$M_{eff} = (M_+ + M_-)/2 \tag{3.9}$$

$$\Delta M_{eff} = (M_+ - M_-)/2 \tag{3.10}$$

where τ_+ and τ_- are the torque with increasing and decreeing magnetic field sweeping, respectively as shown in Fig. 3.26 (A). Note that, since $\tau_{\pm}$ could be negative by

definition, effective magnetization M_{eff} and $M_{\pm}$ could be negative as well. This could be understand more easily in the case of effective susceptibility. Similarly to ΔM, effective susceptibility χ is given by the derivative of ΔM:

$$\chi = \frac{dM_{eff}}{\mu_0 dH}. \tag{3.11}$$

If the sample is paramagnetic and has low crystal symmetry, the torque is given by equation 3.6. Thus,

$$\chi = \Delta\chi \sin 2\phi \tag{3.12}$$

where $\Delta\chi = \chi_{aa} - \chi_{bb}$ and assume the susceptibility tensor is diagonalized. As shown, $\chi(\phi)$ includes the angular dependence, thus it could be either positive or negative. In our case, we could define $\chi = \Delta\chi \sin 6\phi$, but since $\Delta\chi$ is a higher order term, the value of $\Delta\chi$ does not have much meaning. Also, since we are interested in the angular dependence of magnetic susceptibility, it is more convenient to explicitly include ϕ dependence in χ. These definitions are shown in Fig. 3.26.

As mentioned above, about 0.6 T is enough to suppress the superconducting state and let the sample enter the normal state. Thus, in this regime, τ_+ and τ_- as well as M_+ and M_- overlap with each other. Beam model shows that the contribution from the supercurrents induced by the magnetic field sweeping up and down are the same. Thus, $\Delta M == (M_+ + M_-)/2$ and $\chi = \frac{dM}{\mu_0 dH}$ correspond to the intrinsic magnetic magnetization and susceptibility, respectively. The angular dependence of susceptibility in the normal state and the superconducting state is measured at $T =$ 0.3 K over an angular range of 200 degrees. Also, since rotating the magnetic field 180 degrees is identical to the sign reversal of the magnetic field, the negative field sweep data at angle ϕ was treated as the positive data taken at $\phi + 180°$ to cover more than 360 degrees.

The angular dependence of the normal state susceptibility χ at high fields are shown in Fig. 3.26 (B). The data are taken at $H = 0.8$ K so that the superconductivity is fully suppressed. χ is a periodic function of 60 degrees and can be well fit by $\sin 6\phi$. This is consistent with Eq. 3.7 with $n = 3$, indicating the trigonal symmetry of the sample in the normal state. The Fast Fourier Transformation (FFT) data of Fig. 3.26 is shown in Fig. 3.26 (C). The dominant 6ϕ component clearly indicates that the rotational symmetry in the normal state of the system is not broken and trigonal.

Determining the symmetry of the superconducting state by susceptibility requires more care since the superconducting state is not paramagnetic. However, we could use the similar analogy to the hexagonal ferromagnetic material which torque follows $sin6\phi$ dependence as well. Thus, if the symmetry is not broken in the superconducting state, the susceptibility should still follow the $\sin 6\phi$ dependence.

In contrast to the normal state, the rotational symmetry of susceptibility is broken in the superconducting state, as shown in Fig. 3.26 (D). The susceptibility data is taken at $H = 0.05$ T, much lower than the critical field. The angular dependence curve does not follow $\sin 2\phi$ nor $\sin 6\phi$. Shown in Fig. 3.26(E) is the FFT plot of data in Fig. 3.26(D). Instead of the dominant 6ϕ component in the normal state, the 2ϕ and 4ϕ components are dominant in the superconducting state. Thus, the rotational symmetry of the system is broken in the superconducting state.

3.2.3 Rotational symmetry breaking in the hysteresis loop

The rotational symmetry breaking in the superconducting state is also observed in the amplitude of the hysteresis loop in magnetization $\Delta M_{eff} = (M_+ - M_-)/2$. ΔM_{eff} at zero fields can also be considered as spontaneous effective magnetization, similar to that of ferromagnets. The angular dependence of ΔM_{eff} at different fields is shown in Fig. 3.27(A). The overall shape resembles that of susceptibility in the superconducting state shown in Fig. 3.26(D). While ΔM_{eff} goes to zero every 60

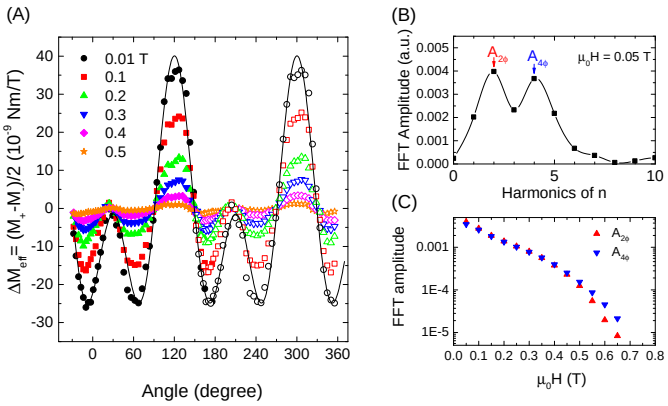

Figure 3.27: **The angular dependence of supercurrent.** (A)The angular dependence of spontaneous effective magnetization $\Delta M - \phi$ at $T = 0.3$ K and $\mu_0 H = 0.01$, 0.1, 0.2, 0.3, 0.4 and 0.5 T. The solid line it the fitting function $f(\phi) = 2A_{2\phi} sin(\phi - 30°) \cos 3\phi$. (B) Fast Fourier Transform (FFT) plot of $\Delta M - \phi$ data at $\mu_0 H = 0.05$ T. (C) The magnetic field dependence of FFT amplitude of $A_{2\phi}$ and $A_{4\phi}$ components.

degrees, the peak hight at 120 degrees is higher than that at 0 or 60 degrees. The FFT data of Fig. 3.27 is shown in Fig. 3.27(B) and (C). At low fields, the 2ϕ and 4ϕ components are dominant instead of 6ϕ components as the same as susceptibility FFT shown in Fig. 3.26(E), but here the amplitude of them are almost the same. Thus, the low field curve in 3.27(A) can be well fit by the function $f(\phi) = 2A_{2\phi} sin(\phi - 30°) \cos 3\phi$ which is shown by the solid line in (A). It is quite surprising that the spontaneous effective magnetization, which originates from the supercurrent, is represented by the product of sinϕ and cos 3ϕ rather than the summation of them. The cos 3ϕ term suggests that the trigonal crystal symmetry is still effective, while sin ϕ term indicates the rotational symmetry breaking, or nematic order. The product of sinϕ and cos 3ϕ thus infers the strong coupling between the nematic order and the crystal symmetry.

Another feature shown in Fig. 3.27(C) is the suppression of the nematic order at high fields. The magnetic field dependence of FFT amplitude for $A_{2\phi}$ and $A_{4\phi}$ is shown. As mentioned above, sin ϕ can be considered as the *nematic* term, which corresponds to $A_{2\phi}$ term in the FFT plot, where $A_{4\phi}$ corresponds to the crystal

symmetry. At low fields, $A_{2\phi}$ and $A_{4\phi}$ are almost equal. At high fields, however, $A_{2\phi}$ decays more rapidly compared to $A_{4\phi}$. This suggests that the nematic order is suppressed when the system is close to the normal state, which is consistent with NMR and specific study on $Cu_xBi_2Se_3$ [58, 59]. Thus, this confirms the nematic order in the superconducting state of $Nb_xBi_2Se_3$, which is consistent with the two-component superconducting order parameter as pointed out by Fu [60].

3.2.4 In-plane anisotropy in Fermi surface

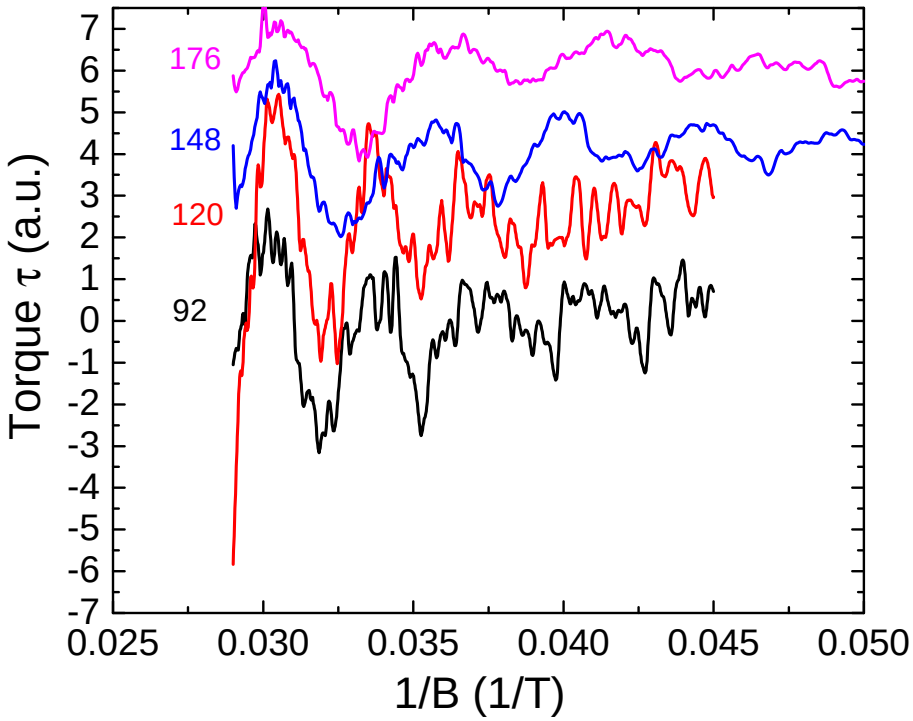

Figure 3.28: **Example in-plane torque curves at high fields.** The background is subtracted.

Recently, the rotational symmetry breaking was explained by the in-plane strain resulting in the anisotropic Fermi surface [77]. If this is the case, the shape of Fermi surface is no longer six-fold, but rather two-fold. To check if this prediction is true, we measured the in-plane angular dependence of quantum oscillation frequency. Generally, in-plane quantum oscillations tend to be small for layered materials. Also, more

than three periods of oscillation are required to precisely determine the frequency and argue the angular dependence of Fermi surface. Thus, we applied a very intense field of 35 T to observe quantum oscillations.

Prior to in-plane anisotropy, we measured the in- and out-of-plane angular dependence of quantum oscillation frequencies as mentioned before [75]. The angular dependence of quantum oscillation frequency is shown in Fig. 3.22. Note that there are two oscillation frequencies observed at $\theta = 90\,^{\circ}$. This sharply contrasts with other doped Bi_2Se_3 crystals in which only one Fermi pocket has been observed.

The example in-plane dHvA oscillations after polynomial background subtraction are shown in Fig. 3.28. The data are taken at $T = 0.3$ K using the resistive magnet in National High Magnetic Field lab, Tallahassee. While the frequencies at 92 and 120 degrees are almost the same, at higher angles the frequencies decrease by a factor of almost 2.

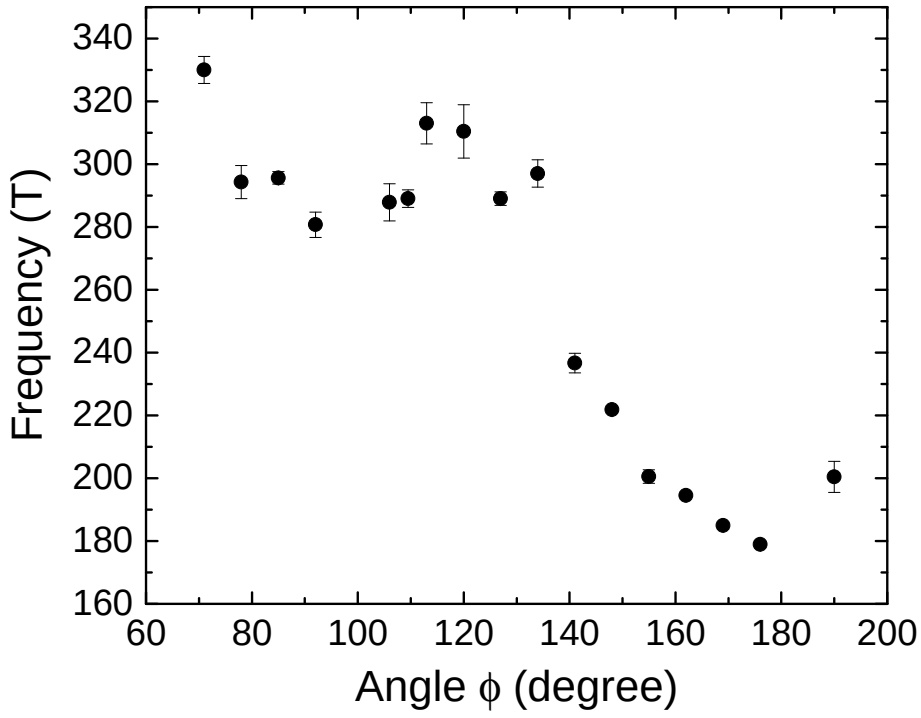

Figure 3.29: **In-plane angular dependence of oscillation frequencies.**

The in-plane angular dependence of dHvA oscillation frequencies is shown in Fig.

3.29. The covered angle range was between 70 and 190 degrees. The frequencies at low angles are almost angle-independent (300 T) while above 130 degrees they decrease down to 180 T at 180 degrees.

There are a few possibilities for the origin of the anisotropic dHvA oscillation frequencies. The first one is that the oscillation anisotropy is extrinsic. In this case, the sample either contains the different phase such as $NbSe_2$ or consists of poly-crystals. However, X-ray diffraction pattern indicates that the sample is a good single crystal. Even if there is a small amount of impurity phase in the sample, it cannot give as large signal as the single crystal. Also, if this is from the impurity phase, its angular dependence should be more isotropic. Also, the behavior cannot be explained by the ellipsoidal model, which is not consistent with the out-of-plane oscillation behavior of $Nb_xBi_2Se_3$. Thus, the extrinsic origin can be ruled out, and the anisotropy of quantum oscillation should be intrinsic.

If the anisotropic oscillation frequencies are intrinsic, it could be due to the secondary Fermi pocket in addition to the ellipsoidal pocket enclosing the Γ point. In this case, however, it is not clear why it does not follow the trigonal symmetry. Another possibility is that the system contains only one Fermi pocket, but it is no longer ellipsoidal and has two extrema in-plane. This could also explain why the secondary frequency cannot be observed when the magnetic field is applied parallel to c-axis. However, given the weak electron correlation in this system, the picture of distorted Fermi surface is questionable. In either case, further Fermiology study is desired to elucidate the origin of the nematic order.

3.2.5 Discussion

So far, we have mainly focused on our new torque magnetometry approach to discover the symmetry breaking in the superconducting state of the materials. Torque magnetometry itself has been used to detect the symmetry breaking in the normal

state of high T_c or heavy fermion superconductors [79, 80]. In this study, as mentioned above, we have further extended this method to detect the rotational symmetry breaking in the superconducting state for the first time. Among methods used to observe the nematic order in the superconducting state of doped Bi_2Se_3, torque magnetometry has its own advantages and disadvantages.

One of the biggest advantages is that this method is very sensitive to the symmetry breaking. If the symmetry is broken, the leading term is a function of 2ϕ. If the symmetry is not broken, the leading term could be a function of 4ϕ or 6ϕ, but in either case, it is a high order term and the amplitude is much smaller than that of 2ϕ contribution. Moreover, the signal from the hysteresis loop is very large and easily measurable. Thus, if there is rotational symmetry breaking (RSB), it could be detected easily by torque magnetometry. In other methods, generally, RSB could be detected by observing the anisotropy of physical values such as the upper critical field or heat capacity. Thus, if the anisotropy is small, it is hard to detect RSB. In addition, this method could be fit into the standard rotator and does not require another special setup. For capacitive cantilevers, also a pair of coaxial cables is required, but still much easier to implement than NMR, thermal measurements or STM where temperature, magnetic field (rotation or high fields) or the sample space is limited. Transport measurement would be easier to implement than torque magnetometry, but in addition to the sensitivity issue, the applied electric field intrinsically induce the symmetry breaking. Thus, dealing with the symmetry breaking result by transport measurements requires special care.

One of the disadvantages of torque magnetometry is that, in particular for the layered materials, the out-of-plane anisotropy is one order of magnitude larger than in-plane anisotropy. Thus, small angle misalignment results in large 2ϕ component offset, which may smear out the RSB signal. The signal from the sample with misalignment is shown in Fig. 3.30. The misalignment of angle is estimated to be a few degrees. The

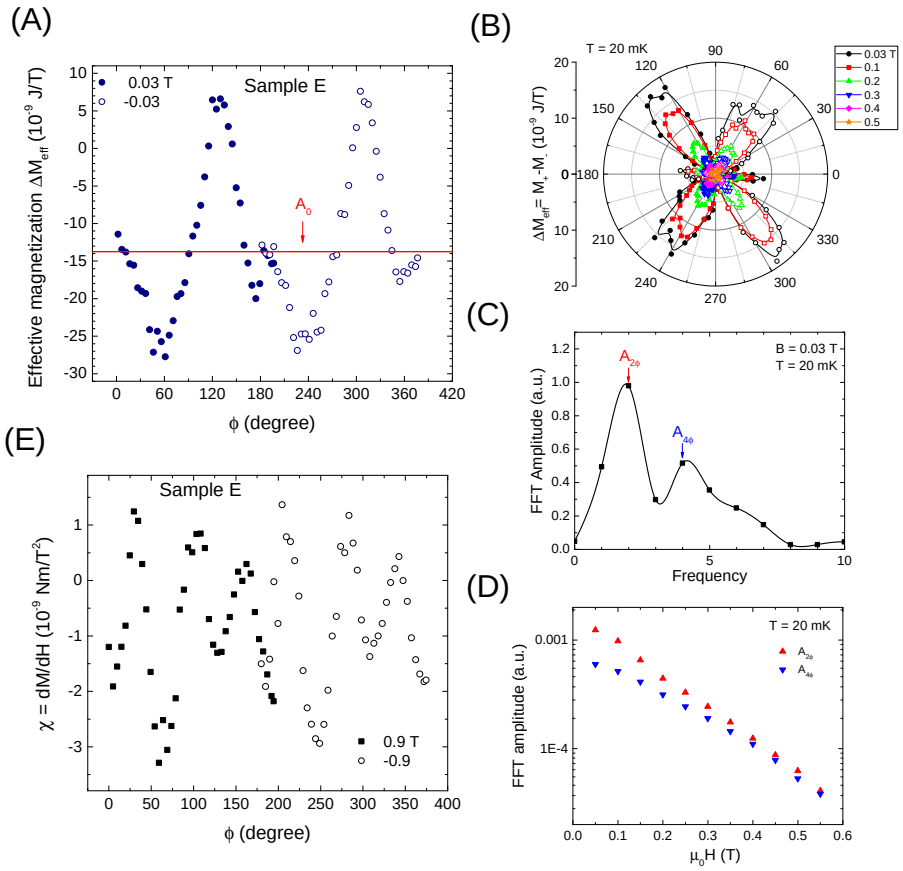

Figure 3.30: **Rotational symmetry breaking in sample E.** (A) Angular dependence of effective spontaneous magnetization ΔM_{eff} from sample E with angle misalignment. (B) Polar plot of data shown in (A). (C) FFT plot of data shown in (A) with constant background subtracted. (D) Magnetic field dependence of FFT amplitude of $A_{2\phi}$ and $A_{4\phi}$. (E) Angular dependence of effective susceptibility in the normal state.

effective magnetization vs angle is plotted in Fig. 3.30(A). As shown, the shape of the curve is quite different from Fig. 3.26(B). This is due to the out-of-plane contribution of $A_{2\phi}$. However, the FFT plot shown in 3.30(C) reveals that there are still both of $A_{2\phi}$ and $A_{4\phi}$ components with no $A_{6\phi}$ contribution. Furthermore, the magnetic field dependence of $A_{2\phi}$ component decays more rapidly than $A_{4\phi}$ component, as similar to Fig. 3.27 (C). Thus, with an angle misalignment, indeed the nematic feature is still detectable. Given the anisotropy of upper critical field of layered superconductors could be sometimes very large, the misalignment can be also the issue for other

methods. Thus, this disadvantage could be ignored. Another disadvantage is that, since the hysteresis loop vanishes along with a certain direction, upper critical field H_{c2} cannot be easily detected in a certain direction. Thus, torque magnetometry is not an ideal tool to evaluate the anisotropy of H_{c2}. Also, while the anisotropy of specific heat or Knight shift can be related to the superconducting gap symmetry or the pairing, torque magnetometry cannot investigate the details of the superconducting nature except for the upper critical fields. Thus, another experimental method is needed to further probe the superconducting nature of the system.

Next, we discuss the origin of the nematic feature in the superconducting state of $Nb_xBi_2Se_3$. First, since the torque magnetometry is a thermodynamic probe, the measurement setup itself does not induce the symmetry breaking. On the other hand, for thermal or electrical transport, thermal or electric field gradient could break the symmetry. As mentioned in the previous chapter, the nematic order has been observed by NMR, specific heat, transport H_{c2} or magnetization, confirming that the nematic order is intrinsic. The next possibility is that the rotational symmetry breaking is induced by the structural transition. Since no sign of structural transition has been observed so far, the lattice constant change should be tiny if it exists. As mentioned below, measuring the change of lattice constant is highly desired. Another possibility is that the nematic order is accompanied by the distortion of Fermi surface as proposed by Venderbos, Kozii and Fu [77]. In this case, the distortion of Fermi surface could be induced by the in-plane tensor strain. If this is the case, the nematic order indeed exists in the normal state. If this is the case, since NMR and specific heat measurement [58, 59] as well as our study did not show the sign of rotational symmetry breaking in the normal state, it is important to study why the nematic order is pronounced in the superconducting state.

To think of the nematic order, it is noteworthy that the nematic axis stays the same direction in the different thermal cycle. Fig. 3.31 shows the polar plot of

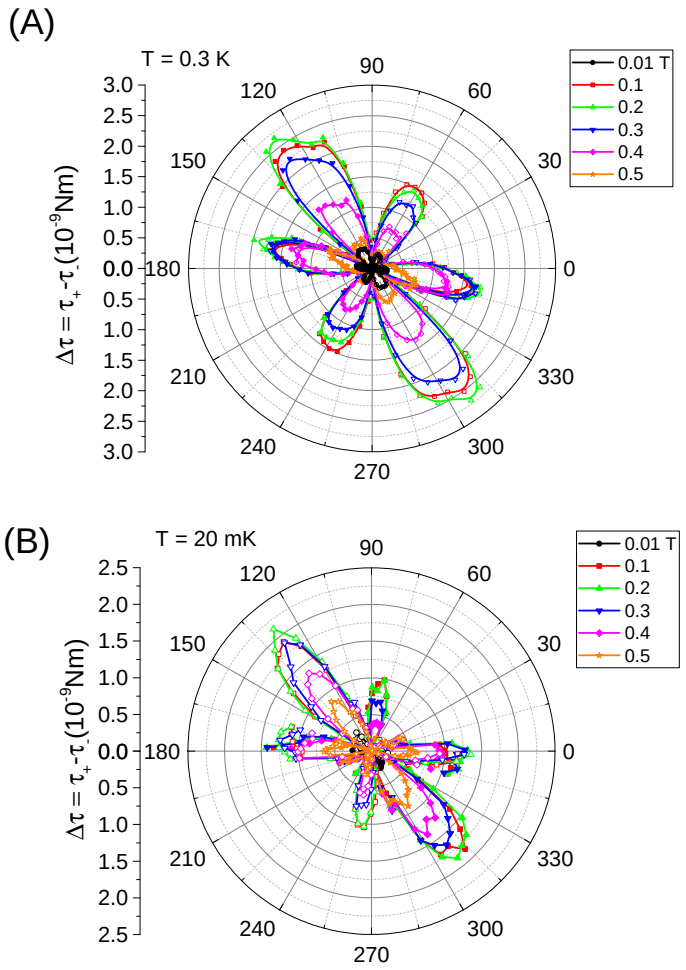

Figure 3.31: **Polar plot of hysteresis loop amplitude of torque for different cooldowns .** (A) THe first cooldown to T= 0.3 K in the helium-3 cryostat. (B) The second cooldown to T = 0.02 K in the dilution fridge.

hysteresis loop amplitude of torque for different cooldowns. While the shape of the polar plot is slightly different due to the small angle misalignment, the nematic axis stays close within 10 degrees uncertainty (around 120 degrees). In doped Bi_2Se_3, the nematic axis is mostly fixed. This fact helps to understand the nature of nematic order in this system.

There are several questions to be answered. First, if the nematic order is induced by the Fermi surface distortion, what is the critical temperature T_c? This question is important to understand the origin of the nematic order. It is also important to check

if there is a lattice constant change at T_c and what kind of physical properties shows the critical behavior around T_c. Second, why is there no domain effect observed, but the mm-size sample behaves like single-domain? In iron-based superconductors, the nematic order is accompanied by the structural transition. Below the transition temperature, the system consists of two equivalent domains which size is μm order. Thus, it is surprising that the doped Bi_2Se_3 does not form three equivalent domains. This question is also related to what determines the direction of the nematic axis. Third, what is the driving force of the nematic order? Since doped Bi_2Se_3 is considered to be more or less non-magnetic and non-correlated, the driving force could be related to the topological nature. Finally, is nematicity related to the emergence of superconductivity? Since the nematic order has been observed in high T_c or heavy Fermion superconductors, it is important to figure out if the nematicity is universal in unconventional superconductors.

3.2.6 Summary

In summary, we have observed the nematic order in the superconducting state of Nb-Bi_2Se_3 by in-plane torque magnetometry which is a thermodynamic probe. Either hysteresis loop or magnetic susceptibility show nematicity in the superconducting state, while in the normal state the angular dependence of susceptibility is a function of sin 6ϕ, indicating that the rotational symmetry is preserved. Furthermore, we revealed that the in-plane quantum oscillation frequency shows two-fold symmetry rather than six-fold. This is consistent with the theoretical prediction that the origin of nematicity is an in-plane strain. Further in-plane Fermiology study will nail down what is the driving force of strain.

CHAPTER IV

Unconventional superconductivity in transition metal dichalcogenide WTe_2 thin films

4.1 Background

4.1.1 Transition metal dichalcogenides

As described in Chapter I, the inversion symmetry breaking is a key ingredient for Weyl semimetals. Particularly, a family of transition metal dichalcogenides (TMD)s has been recently focused on due to its non-centrosymmetric (i.e. inversion symmetry breaking) crystal structure in monolayers. One of the exotic features TMDs show is Ising superconductivity, where the upper critical field H_{c2} violates the paramagnetic Pauli limit by a factor of 5-10 . This feature was recently observed in monolayer of MoS_2 and $NbSe_2$ [81, 82, 83, 84, 85, 86].

MoS_2 and $NbSe_2$ have the 2H-type crystal structure as shown in Fig. 4.1. The bulk single crystal consists of the stacked monolayers of triangular MoS_2 and $NbSe_2$ lattices, resulting in a honeycomb-like structure. Adjacent monolayers have the opposite direction to each other. If the even number of the monolayer is stacked, there is an inversion center in between the layers, resulting in the centrosymmetric structure. However, if the odd number of the monolayer is stacked, in particular in the monolayer case, in-plane inversion symmetry is broken, generating in-plane electric

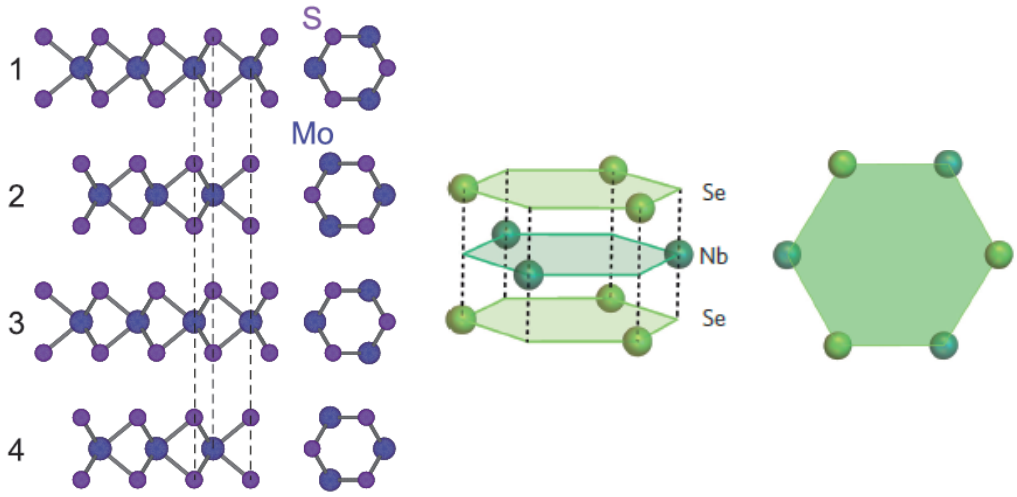

Figure 4.1: **Crystal structure of 2H-MoS_2 and $NbSe_2$.** Adapted from [81] (left) and [84] (right).

field E. Thus, in the studies mentioned above, mono-layer systems have been mainly focused on. Importantly, TMDs also have very strong spin-orbit coupling (SOC)s, which makes the systems topologically nontrivial. When the system becomes a thin film, due to the strong anisotropy around the interface, the additional spin-orbit coupling (called Rashba SOC) emerges, Also, when the inversion symmetry is broken, there is additional SOC that is proportional to $k \times E \cdot \sigma$, which pins the spin direction to out-of-plane. This is called the Ising SOC, with the comparison to in-plane type Rashba SOC. In this case, the Cooper pair in the superconducting state is also strongly pinned to the out-of-plane as well, preventing the magnetic field from breaking the pairs and enhancing the in-plane H_{c2}. This type of superconductors is called Ising superconductors.

The first evidence of Ising superconductivity was reported by two groups mearing the gated monolayer MoS_2 device [81, 82]. The two-dimensional superconducting features are shown in Fig. 4.2. The critical temperature T_c is 7.4 K (Fig. 4.2(A)). The angular dependence of the upper critical field H_{c2} (Fig. 4.2(B)(C)(D)) shows the cusp at 0 degrees from in-plane, indicating two-dimensional system. Furthermore,

in the V vs I plot around T_c, the power law dependence was observed, indicating the BKT transition (Fig. 4.2(E)(F)). This confirms the two-dimensionality in this system.

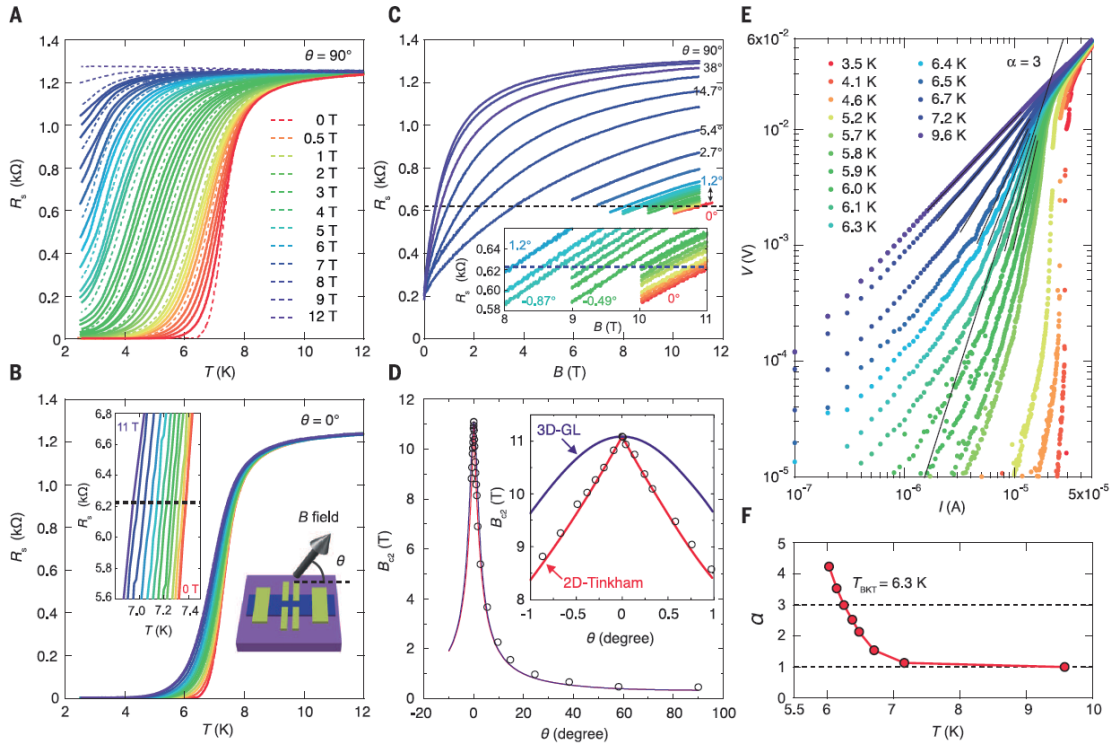

Figure 4.2: **Two-dimensional features in gated monolayer MoS_2.** (A) Temperature dependence of resistivity of gated monolayer MoS_2 with out-of-plane magnetic fields. (B) Temperature dependence of resistivity of gated monolayer MoS_2 with in-plane magnetic fields. (C) Magnetoresistivity at different angles. (D) Angular dependence of H_{c2}. Solid lines indicate the two-dimensional (red) and three dimensional (blue) fitting. (E) V vs I plot around the superconducting transition in a logarithmic scale. (F) Temperature dependence of the exponent of the power-law scale. Adapted from [81].

The violation of paramagnetic Pauli limit H_p is shown in Fig. 4.3. The magnetic field is applied in-plane. Above the magnetic field of Pauli limit H_p, which is given by $H_p = 1.84\ T_c$, the Zeeman energy exceeds the superconducting condensation energy, resulting in the breaking of superconductivity. In Ising superconductors, however, the Ising SOC pins the spin direction to out-of-plane, suppressing the Zeeman energy and

enhancing the effective Pauli limit. The magnetic field and temperature dependence of resistivity of monolayer MoS_2 is shown in Fig. 4.3 (A) and (B), respectively. While T_c is around 8 K, H_{c2} is much higher than its Pauli limit of around 14 T. The H_{c2} vs T diagram is plotted in Fig. 4.3 (C)(D), clearly showing the violation of Pauli limit. Thus, this indicates the existence of Ising superconductivity mechanism in this system.

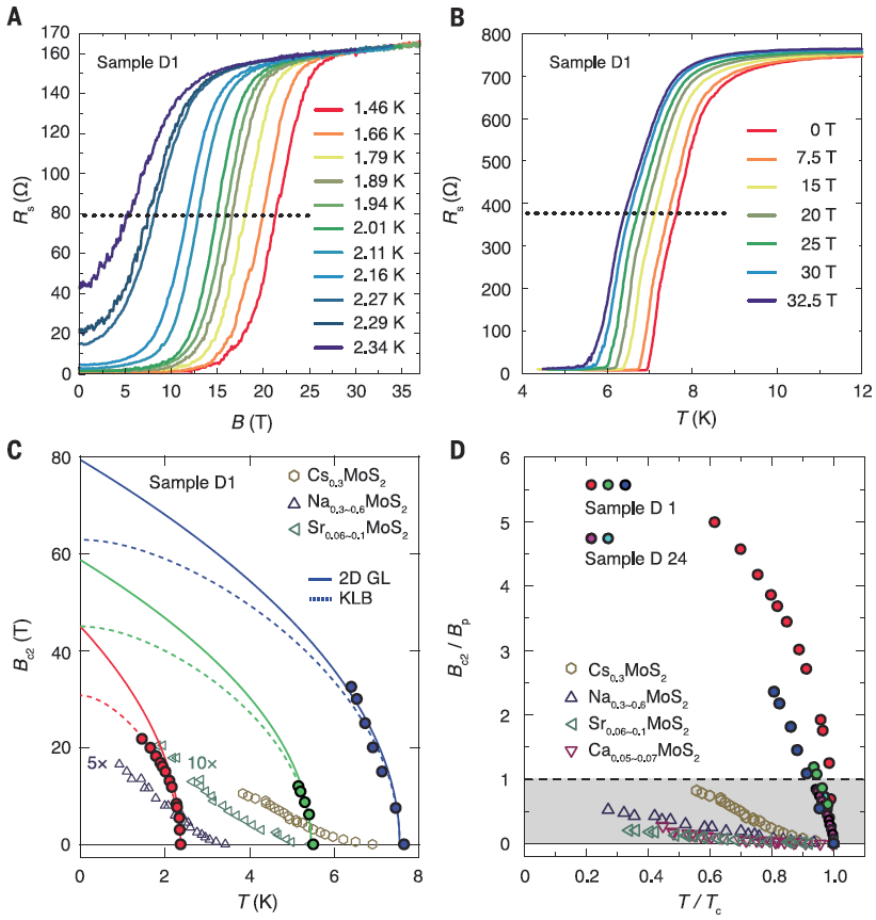

Figure 4.3: **Violation of Pauli limit in monolayer MoS_2.** (A)(B) Magnetic field and temperature dependence of resistivity of monolayer MoS_2, respectively. (C)(D) H_{c2} vs T diagram and its normalized plot, respectively. Adapted from [81].

4.1.2 Type II Weyl semimetal WTe_2

4.1.2.1 Type II Weyl semimetal

More recently TMD compound WTe_2 and $MoTe_2$ show even more exotic features due to its unique T_d crystal structure. The T_d has no inversion symmetry in bulk.

As the inversion symmetry is broken, the Weyl physics can be expected in these systems. Moreover, in 2015 Soluyanov *et al.* predicted that these materials belong to a new Weyl system, called type II Weyl semimetal [87]. The conceptual band structure of type-II Weyl semimetal is shown in Fig. 4.4. In ordinary Weyl semimetals (i.e., type-I), the linear dispersion around the Weyl point is symmetric, as shown in Fig. 4.4 (a). This also means that the Fermi surface is point-like around the Weyl point. However, in type-II Weyl semimetals, the Weyl point is "tilted", thus the Fermi surface can be different from the simple type-I Weyl physics. This case was overlooked by Weyl since it breaks the Lorentz invariance. However, in condensed matter physics, Lorentz invariance could be unpreserved, realizing the new type of Weyl fermion. Thus, there is no counterpart of Type-II Weyl fermion in the elementary particle physics, which makes this system more interesting. The theoretical calculation also predicts that WTe_2 and $MoTe_2$ have type-II Weyl points.

Soon after the theoretical discovery and prediction of type-II Weyl semimetals, the existence of type-II Weyl points are experimentally confirmed by ARPES in WTe_2, $MoTe_2$ and related maretirals [88, 89, 90, 91, 92, 93, 94].

To study WTe_2 and $MoTe_2$, it is very important to understand the crystal structure of them. The bulk $MoTe_2$ may have three different structures, which are a hexagonal 2H phase (which is mentioned above), monoclinic 1T' phase and orthorhombic T_d phase. The crystal structures of 1T' and T_d are almost the same, except for the layer stacking angle as shown in Fig. 4.5 (c)(d). For T_d phase, each layer is stacked vertically (4.5 (d)), while for 1T' phase the stacking angle is 94 degrees (Fig.

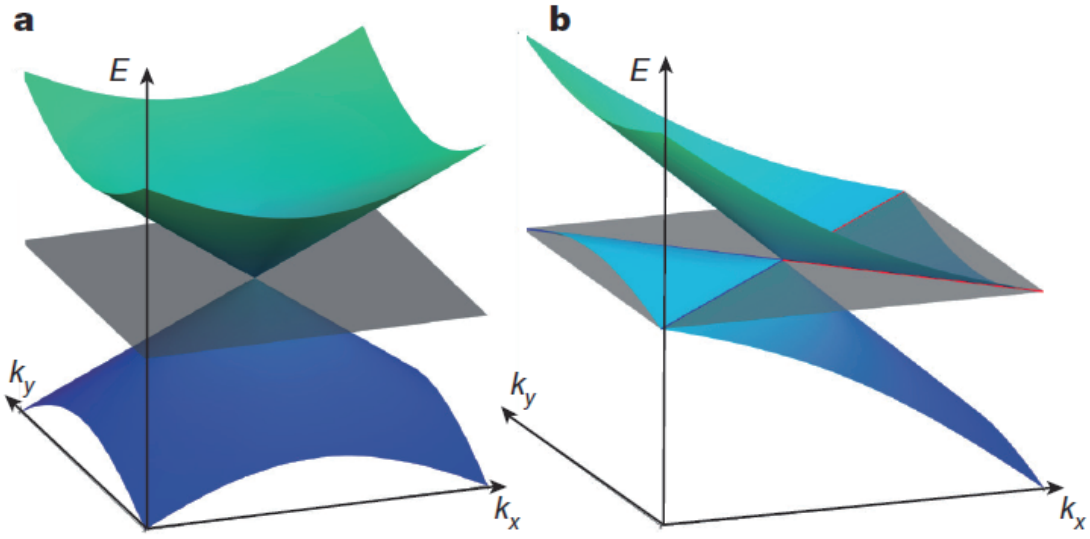

Figure 4.4: **Band structure of type-II Weyl semimetal.** (a) Type-I Weyl semimetal. (b) Type-II Weyl semimetal. Adapted from [87].

4.5 (c)). Notably, while the 1T' phase is centrosymmetric, the T_d phase is non-centrosymmetric. Thus, to study the Weyl physics in these systems, it is important to make sure that the sample is in the T_d phase. It is know that, for $MoTe_2$, there is a structural phase transition from the high-temperature 1T' phase to the low-temperature T_d phase at around $T = 250$ K (Fig. 4.5 (i)). On the other hand, the bulk WTe_2 has the T_d structure from the room temperature down to the dilution fridge temperature.

4.1.2.2 Large, non-saturating magnetoresistance in WTe_2

Prior to the discovery of Type-II Weyl nature, WTe_2 has already attracted huge interest due to giant, non-saturating magnetoresistance [95]. The magnetoresistance at a different temperature is shown in Fig. 4.6. The MR reaches 450,000 % at 4.5 K and 14.7 T, and 13 million % at 0.5 K and 60 T. Remarkably, the MR is not saturating and parabolic up to 60 T.

It is explained by the electron and hole carrier model. In this model, the conduc-

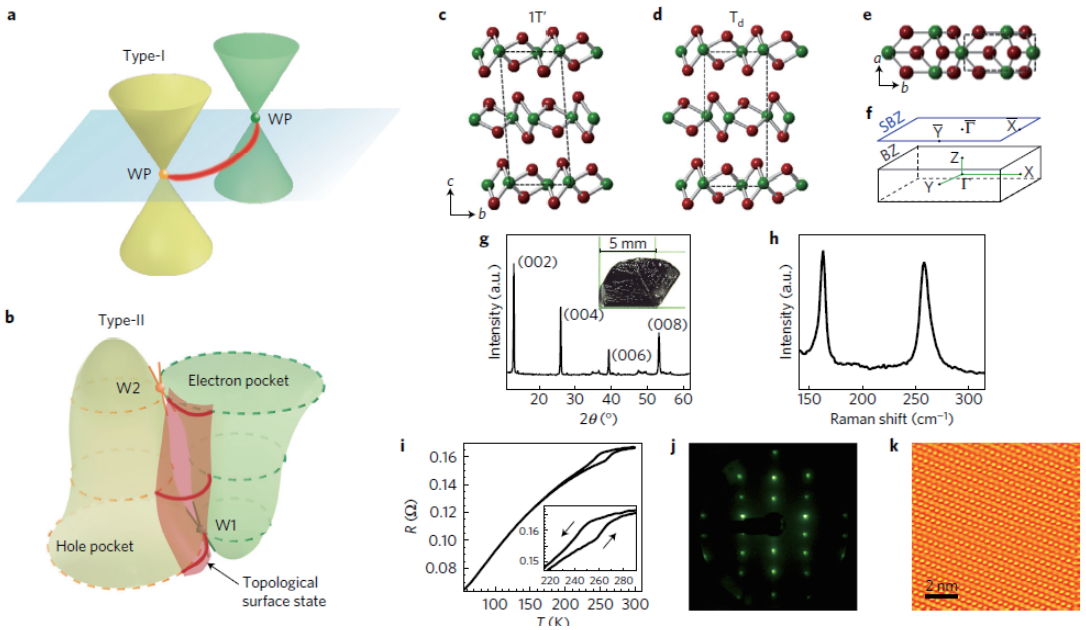

Figure 4.5: **Crystal structure of $MoTe_2$.** (a)(b) Band structure of Type-I and II Weyl semimetals, respectively. (c)(d) The crystal structure of 1T' ans T_d phase, respectively. (e) The crystal structure seen in-plane. (f) Brillouin zone. (g) X-ray diffraction at room temperature. (h) Raman spectrum at room temperature (i) Temperature dependence of resistivity showing the first order phase transition. (j) Electron diffraction pattern at the low temperature phase. (k) STM image at 4.2 K. Adapted from [93].

tivity tensor is given by

$$\sigma = e\left[\frac{n\mu_n}{1+i\mu_n B} + \frac{p\mu_p}{1-i\mu_p B}\right] \tag{4.1}$$

where n, p, μ_n and μ_p are the carrier density and mobility of electrons and holed, respectively. The resistivity is therefore given by

$$\rho = \frac{1+\mu_n\mu_p B^2 + i(\mu_n-\mu_p)B}{e[n\mu_n + p\mu_p + i(p-n)\mu_n\mu_p B]} \tag{4.2}$$

which has maxima at $n = p$. Thus, the large MR indicates that the electron and hole are perfectly compensated in this system.

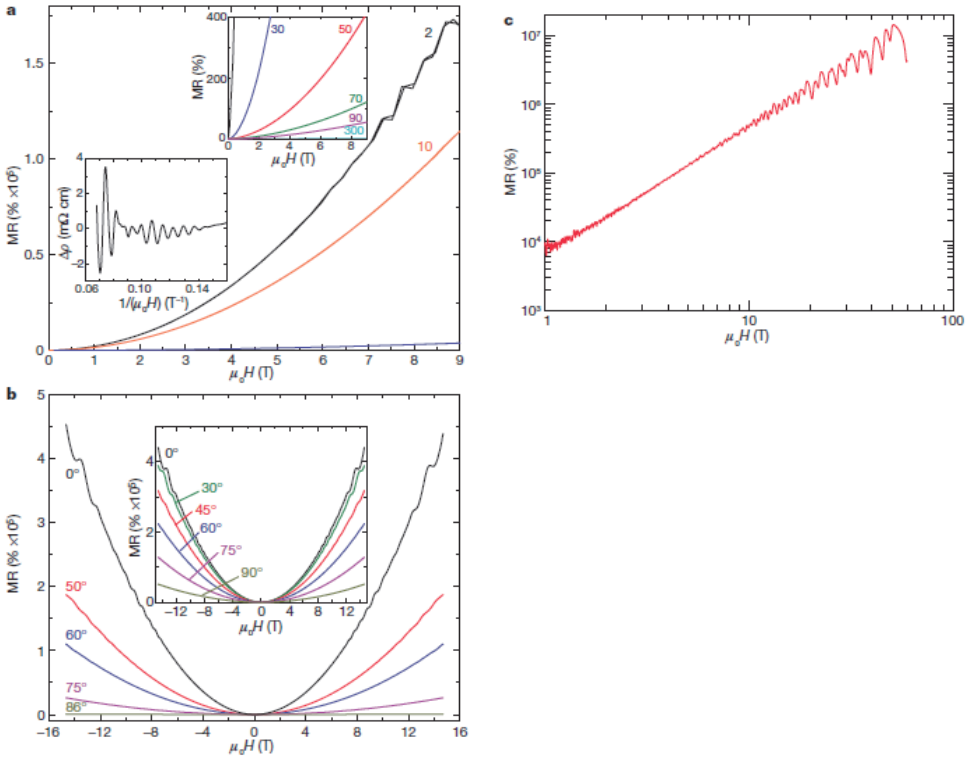

Figure 4.6: **Large, non-saturating magnetoresistance of WTe_2.** (a) MR curves with $H \parallel a$ at different temperatures. (b) MR curves at 4.5 K and different angle from c-axis. The current is applied parallel to a-axis. (c) High-field MR data at 0.53 K. Adapted from [95].

4.1.2.3 Superconductivity

While WTe_2 is metallic down to the dilution fridge temperature, the pressure-induced superconductivity was reported [96, 97]. In Fig. 4.7, the pressure dependence of resistivity and susceptibility at low temperature is shown. The resistivity drop was observed at 2.5 GPa, and the zero resistivity was achieved at 11 GPa, as shown in Fig. 4.7. T_c increases as the applied pressure increases, and at becomes maximum of 7 K at 16.8 GPa, above which T_c start decreasing (Fig. 4.7(b)). The susceptibility measurement in Fig. 4.7 (c) also shows the Meissner effect, confirming the superconductivity. However, the upper critical field H_{C2} of WTe_2 under pressure is much lower than the Pauli limit.

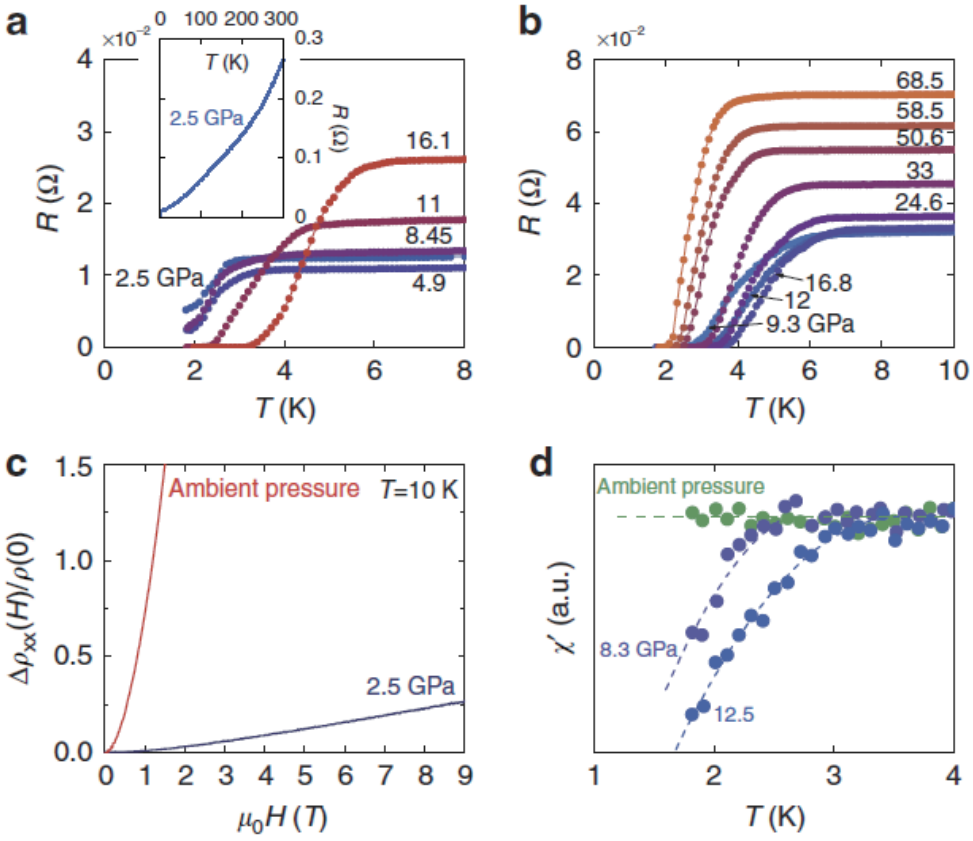

Figure 4.7: **Pressure-induced superconductivity in WTe_2.** (a) Resistivity vs temperature at different pressures. (b) Higher pressure resistivity vs temperature plot. (c) MR curves at ambient pressure and 2.5 GPa. (d) THe a.c. susceptibility measurement under pressure. Adapted from [96].

From X-ray diffraction analysis, it is pointed out that the superconductivity is induced by the structural transition from T_d to 1T' under pressure[98]. Fig. 4.8 (a) shows the simulated X-ray diffraction peaks of T_d (blue) and 1T' (green) phases as well as experimental results at 10 GPa. Since two structures are very similar, the X-ray diffraction pattern is also similar to each other. The significant difference is shown in (011) and (113) peaks, which split into (011) and $(01\bar{1})$ or (113) and $(11\bar{3})$ in the 1T' phase due to lower symmetry. From experimental results, at 10 GPa clearly those peaks split into two, indicating that the sample is in 1T' phase. The evolution of the peak splitting by the applied pressure is shown in Fig. 4.8 (b). At 1.3 GPa, the

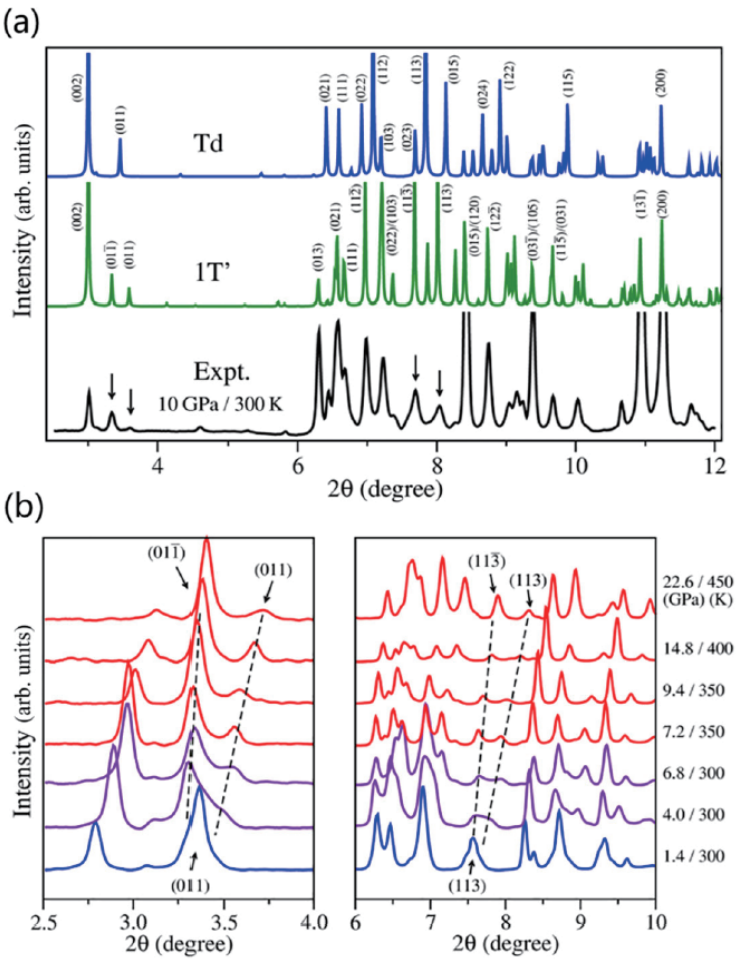

Figure 4.8: **X-ray diffraction peaks of WTe_2 under pressure.** (a) Simulated X-ray diffraction peaks of T_d and 1T phases and experimental result at 10 GPa. (b) X-ray diffraction patterns at different pressures Adapted from [98].

peak is still merged, but above 4 Gpa, the split of diffraction peaks is observed. As the pressure increases, the peak separation increases as well. Thus, the high-pressure studies of superconducting properties reflect the centrosymmetric crystal structure, which does not possess Weyl points.

On the other hand, $MoTe_2$ becomes a superconductor at $T_c = 0.1$ K [99]. When the pressure is applied to the sample, T_c increases dramatically to 5 K at 0.8 GPa with a rapid drop of the structural transition temperature. At higher pressure, T_c keeps increasing while the crystal structure becomes 1T' all the way to the base temperature.

This behavior is consistent with that of WTe_2. The difference of pressure dependence of crystal structure and superconducting temperature between WTe_2 and $MoTe_2$ has to be considered when one desires to study superconducting properties in Type-II Weyl systems.

4.2 Results

4.2.1 Sample characterization

Thin WTe_2 films were grown on sapphire c-Al_2O_3 substrates by a Veeco Genxplor MBE growth system. We measured the films with four different thickness of 5.5, 7, 10 and 14 nm. The structural properties of thin films were measured by scanning probe microscopy (SPM), cross-sectional transmission electron microscopy (TEM), XPS, and EDX. According to the SPM result, the sample surface is very smooth, with a roughness of 0.22 nm as shown in Fig. 4.9 (a). X-ray photoelectron spectroscopy (XPS) measurement was performed right after growth, showing that the core level peaks of W (4d orbit) and Te (3d orbit) are consistent with the previous studies on WTe_2 Bulk crystals (Fig. 4.9(b)). Also, the peaks from oxidized W and Te were not observed. The uniform and continuous film growth on a sapphire was observed by TEM without any pinholes as shown in Fig. 4.9 (c). The expansion of (c) on WTe_2 layers in (d) shows that the interplanar spacing is 0.667 nm, which is slightly smaller than that of Bluk crystals (0.7035 nm). Thus, the tensor strain is present due to the lattice mismatch between WTe_2 and sapphire. The energy dispersive X-ray spectroscopy (EDX) measurement along the blue line in (c) is shown in (e). The W and T intensities are almost constant at the regions of WTe_2 films, indicating the uniform growth. X-ray diffraction pattern in (f) shows the strong peaks from (024) and (122), which supports the T_d structure of the films.

The resistivity vs temperature curves down to 0.3 K for 10 and 5.5 nm WTe_2

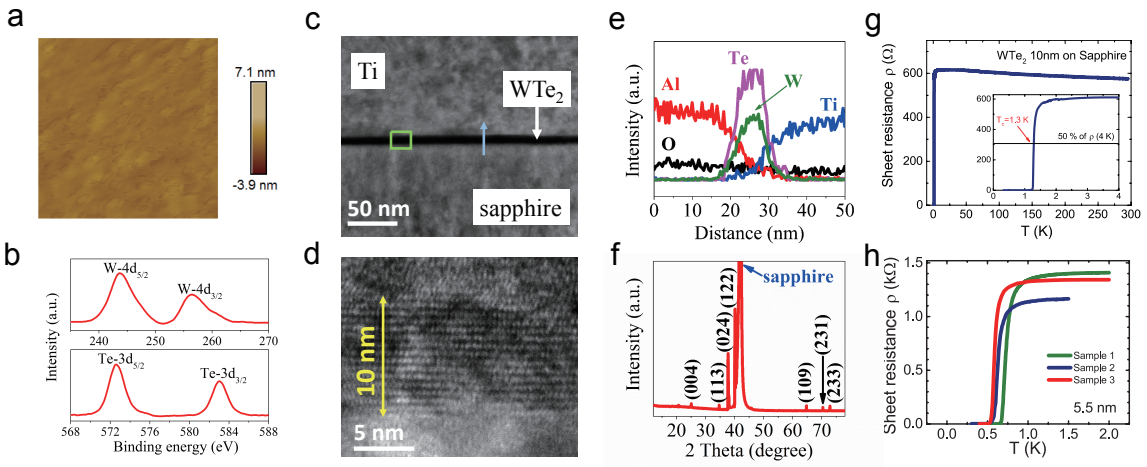

Figure 4.9: **Characterization of WTe_2 thin films.** (a) SPM image of the surface of a WTe_2 thin film. (b) XPS spectra. (c) Cross sectional TEM image of the thin film. (d) Expansion of (c). (e) EDX spectra along the blue arrow shown in (c). (f) X-ray diffraction pattern. (g)(h) Resistivity vs temperature showing the superconducting transition at around 1 K for samples with thickness 10 nm and 5.5 nm, respectively.

films are shown in Fig. 4.9 (g) and (h), respectively. From room temperature, the resistivity keeps decreasing down to 50 K, below which the resistivity becomes T independent until the superconducting critical temperature T_c. T_c is around 1 K for all the samples. Since the resistivity is almost constant near T_c in the normal state, we define T_c as $R(T_c) = 0.5\ R(T = 4K)$.

To further confirm the superconductivity, we measured the mutual inductance of the WTe_2 thin film. Shown in Fig. 4.10 is the temperature dependence of mutual inductance signal normalized by the value at T= 4 K with and without 1 T magnetic field applied. The magnetic field is applied perpendicular to the film surface so that 1 T is high enough to completely suppress the superconductivity as discussed later. Below 2 K, the Meissner effect was observed at 0 T, while under magnetic fields the signal is temperature independent. The observation of both Meissner effect and zero resistivity confirms the superconducting transition in WTe_2 thin films.

We also carried out the control experiments to confirm that the superconductiv-

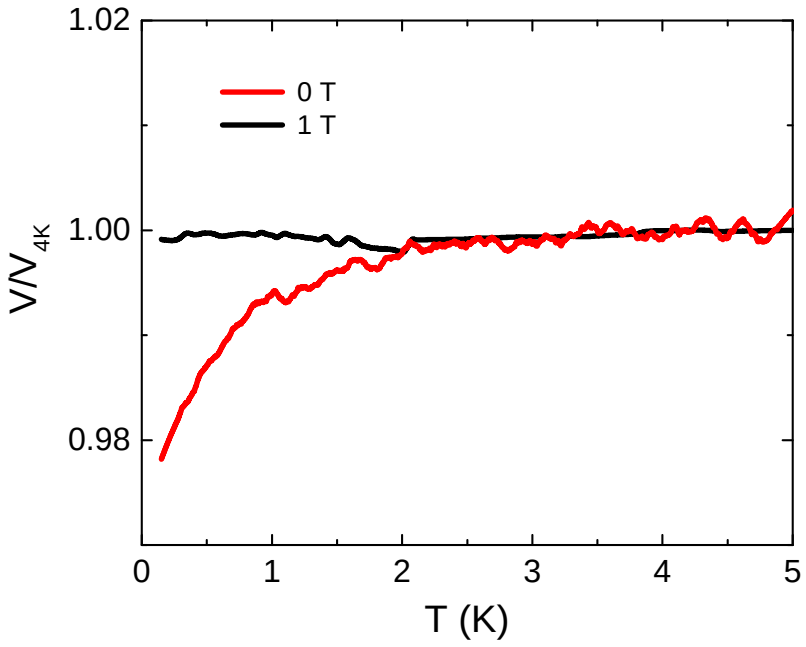

Figure 4.10: **Control experiments of the 10 nm W thin film.** The temperature dependence of resistivity from the 10 nm W thin film confirms that the superconductivity originates from the WTe_2 phase of the samples.

ity originates from the WTe_2 thin films and not from the superconducting phase of tungsten [100]. The W thin film with 10 nm thickness was grown in the same condition as WTe_2 sample growth. The temperature dependence of resistivity from the W film is shown in Fig. 4.11. No superconducting transition was observed down to 25 mK. Also, the metallic behavior is different from what we observed from WTe_2 films, indicating that the contribution from the W phase is ignorable if it exists. Thus, it is confirmed that the observed superconductivity is intrinsic and originates from WTe_2 phase.

4.2.2 Low field enhancement of T_c

Fig. 4.12 shows the resistivity data from 5.5 nm thickness samples. First, the resistivity vs temperature under different in-plane magnetic fields are shown in (a) and (b). As shown in (a), the critical temperature T_c initially increases with applying magnetic fields up to 2 T. This behavior is different from the usual superconductors

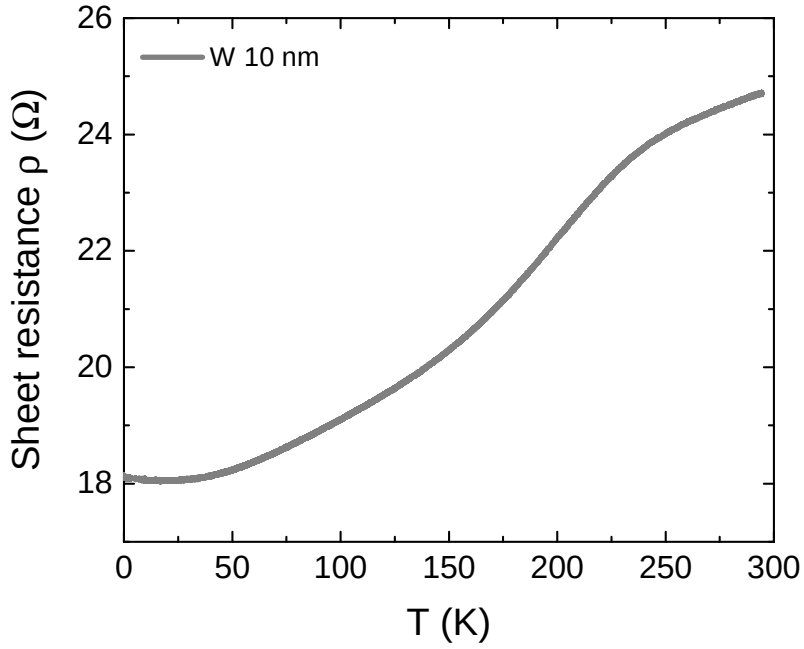

Figure 4.11: **Control experiments of the 10 nm W thin film.** The temperature dependence of resistivity from the 10 nm W thin film confirms that the superconductivity originates from the WTe_2 phase of the samples.

where the magnetic fields suppress superconductivity. Above 2 T, T_c starts to decrease as shown in (b). The T_c enhancement is 10 mK at 2 T. This means that when the magnetic field is increasing, the MR is negative at low fields. Indeed, we observe this behavior as shown in Fig. 4.12(c). The similar but even larger negative MR behavior was observed in sample 2 (Fig. 4.12(d)), confirming the enhancement of T_c by low magnetic fields. Since the MR becomes almost constant at high fields, similar to T_c, we define the upper critical field H_{c2} as $R(H_{c2}) = 0.5\ R_{const}$. The phase diagram of normalized upper critical field H_{c2}/H_p vs critical temperature T_c/T_{c0} is plotted in Fig. 4.12(e), where Pauli limit $H_p = 1.84\ T_c$. Sample 1 shows clear enhancement of T_c by magnetic fields. Even larger enhancement of 1.6% at 3 T was observed in sample 2. Since there is a 10% error in evaluating the thickness of WTe_2 thin films, the difference between sample 1 and 2 could be due to the potential thickness difference.

In general, the upper critical field H_{c2} is limited by two factors, Pauli paramagnetic limit H_p and orbital limit H_{orb}. Above the magnetic field of Pauli limit H_p, the Zeeman

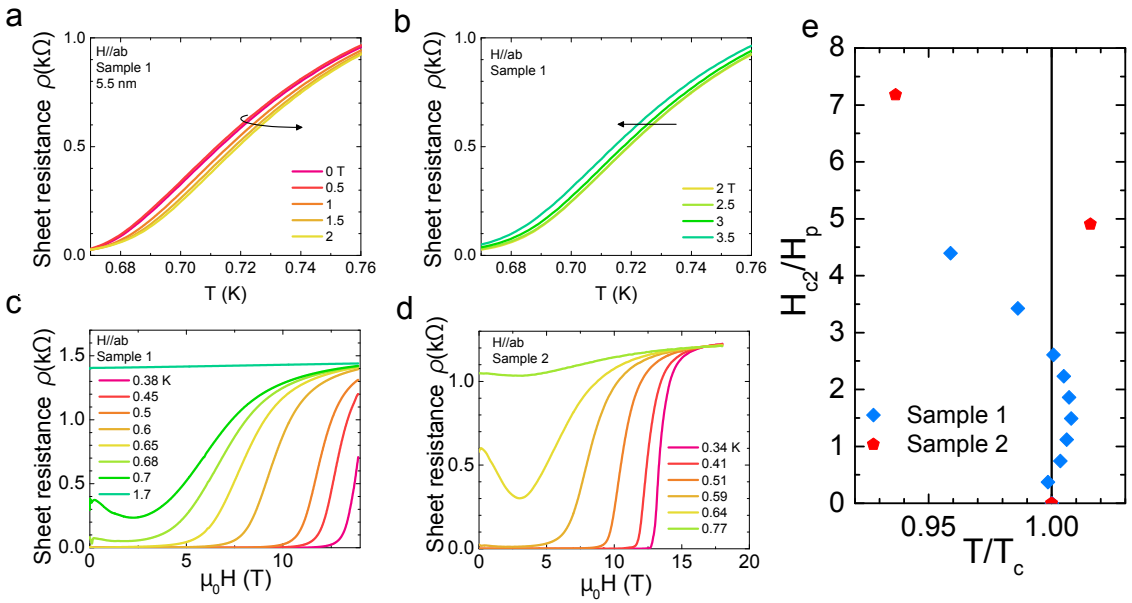

Figure 4.12: Fig. **Resistivity from 5.5 nm samples under in-plane magnetic fields.** (a)(b) Temperature dependence of resistivity under magnetic fields (a) up to 2 T and (b) above 2 T. (c)(d) Magnetoresistance at different temperatures from sample 1 and sample 2, respectively. (e) Phase diagram of H_{c2}/H_p vs T_c/T_{c0}.

energy exceeds the superconducting condensation energy, resulting in the breaking of superconductivity. At the orbital limit H_{orb}, two vortex cores overlap with each other, also destroying the superconducting state. Generally, however, the orbital limit does not exist in two dimensional systems with a magnetic field applied in-plane because of no orbital degrees of freedom. Thus, in-plane H_{c2} is dominantly limited by the Pauli limit. The violation of Pauli limit indicates that the superconducting pairing is more governed by a spin triplet rather than a spin singlet.

The in-plane MR from thicker samples are also measured. Fig. 4.13 shows the MR curves from 7, 10 and 14 nm films. At high temperatures close to T_c, 7nm sample shows the negative MR indicating the enhancement of T_c by low magnetic fields (Fig.4.13(b)). However, the thicker samples did not show the field enhancement of T_c ()Fig. 4.13(d)(f)). All of the samples show the violation of Pauli limit.

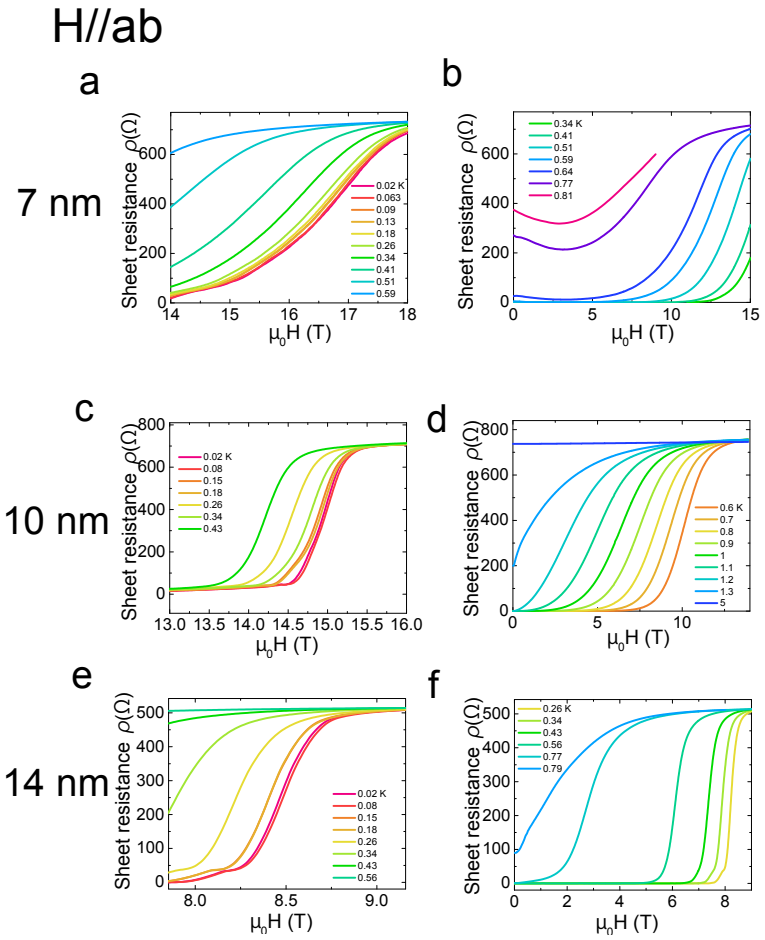

Figure 4.13: **In-plane magnetoresistnace from 7, 10 and 14 nm samples.** (a)(b) Magnetoresistance from the 7nm sample at low temperatures (a) and high temperatures (b), respectively. (c)(d) From the 10 nm sample. (e)(f) From the 14 nm sample.

Contrary to the in-plane MR, the out-of-plane H_{c2} is limited by the orbital limit for all the samples as shown in Fig. 4.14. This is also seen in the H_{c2} vs T_c phase diagram shown later.

4.2.3 High field enhancement of T_c

The unconventional feature in the upper critical field was also observed in low temperature, high field region, as shown in Fig. 4.15. We measured the same 5.5 nm samples as measured in Fig. 4.12. For sample 2, H_{c2} at 90 mK is 0.11 T higher than that of 20 and 63 mK, then H_{c2} decreases as temperature increases (Fig. 4.15(a)(b)).

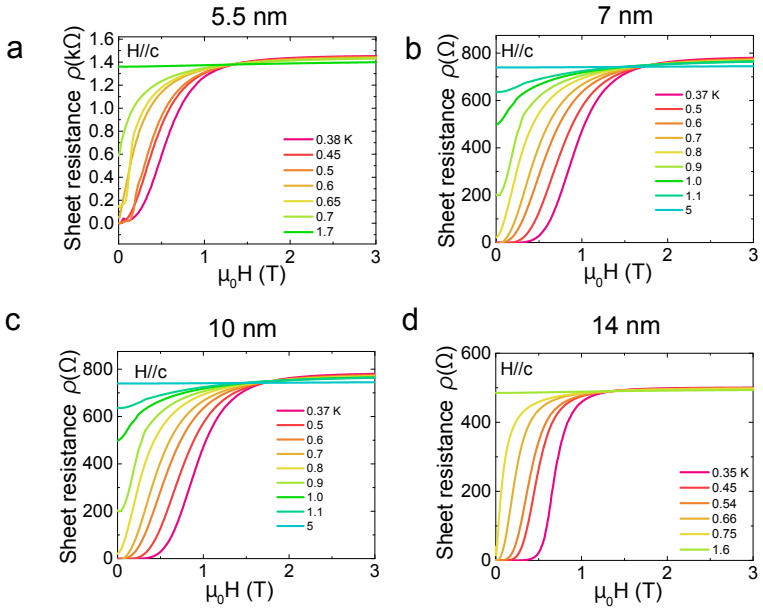

Figure 4.14: **Out-of-plane magnetoresistnace from 5.5, 7, 10 and 14 nm samples.** (a)(b)(c)(d) MR from 5.5, 7, 10 and 14 nm films, respectively

This behavior is more apparent in sample 1. H_{c2} is at 96 and 160 mK is 0.29 T higher than that of the base temperature of 40 mK, as shown in Fig. 4.15(c). This non-monotonic behavior can be also treated as the T_c enhanced by the high magnetic field. The resistance vs temperature at fixed fields are shown in Fig. 4.15(d). At $H = 13.7$ T, while the resistivity at the base temperature of 20 mK is finite, it becomes zero at a higher temperature between 100 and 200 mK. The resistivity drop with increasing T is also observed in higher magnetic fields. The H_{c2} vs T_c phase diagram at high fields and low temperatures is shown in Fig. 4.15 (e). As the temperature decreases, the critical fields flatten out, then slightly drops close to zero temperature. The H_{c2} enhancement for sample 1 is 0.8% at 90m K compared to 20 mK. For sample 2, the enhancement is 2 % at 96 and 160 mK compared to 40 mK. Thus, the re-entrant superconductivity behavior was confirmed by two samples.

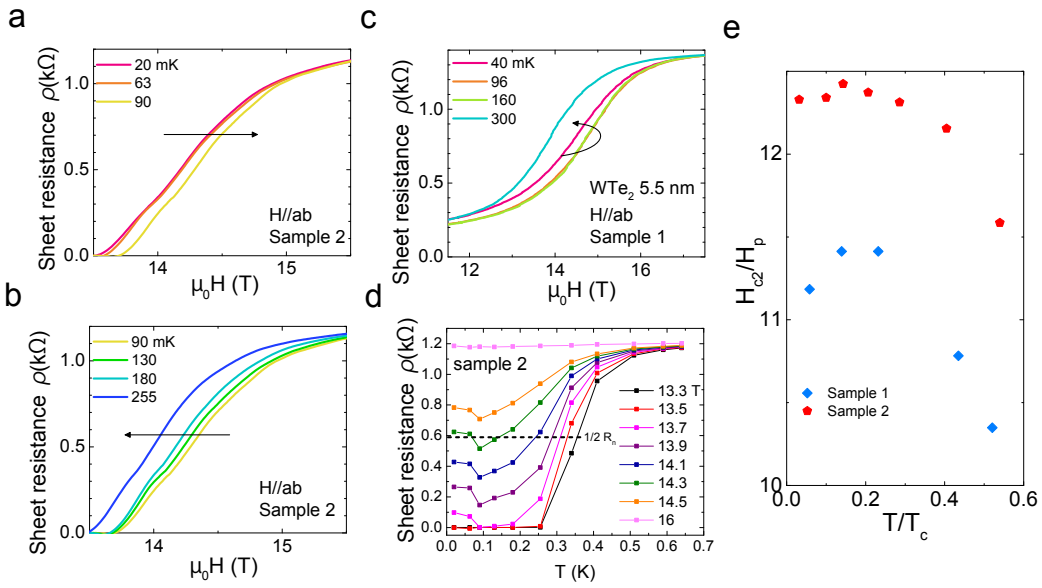

Figure 4.15: **High-field superconductivity enhancement at the base temperature.** (a)(b) Magnetic field dependence of resistivity at low temperatures from sample 2. (c) Magnetic field dependence of resistivity at low temperatures from sample 1. (d) Temperature dependence of resistivity at different fields. The data shown in (c) is used to construct the figure. (e) Phase diagram of H_{c2}/H_p vs T/T_c.

4.2.4 Thickness dependence of T_c and H_{c2}

The summary of H_{c2} and T_c is shown in Fig. 4.16. Fig. 4.16 (a) is the phase diagram of normalized H_{c2} vs T_c for all the thickness (5.5, 7, 10 and 14 nm) with H ∥ab and H ∥c. For in-plane configuration, the 5.5 and 7nm samples show very large Pauli violation of more than 10 times H_p. As far as we know, this is the highest value among all the non-centrosymmetric superconductors. Also, the enhancement of T_c with applied magnetic field around T_c is observed only in 5.5 and 7 nm samples. On the other hand, H_{c2} vs T curves with H ∥c overlap with each other, confirming that the H_{c2} is limited by H_{orb} in this configuration. The thickness dependence of T_c and H_{c2} is shown in Fig. 4.16 (b). The T_c of the 10 nm film shows highest T_c of about 1.55 K. The H_{c2} is almost the same between 5.5, 7 and 10 nm samples.

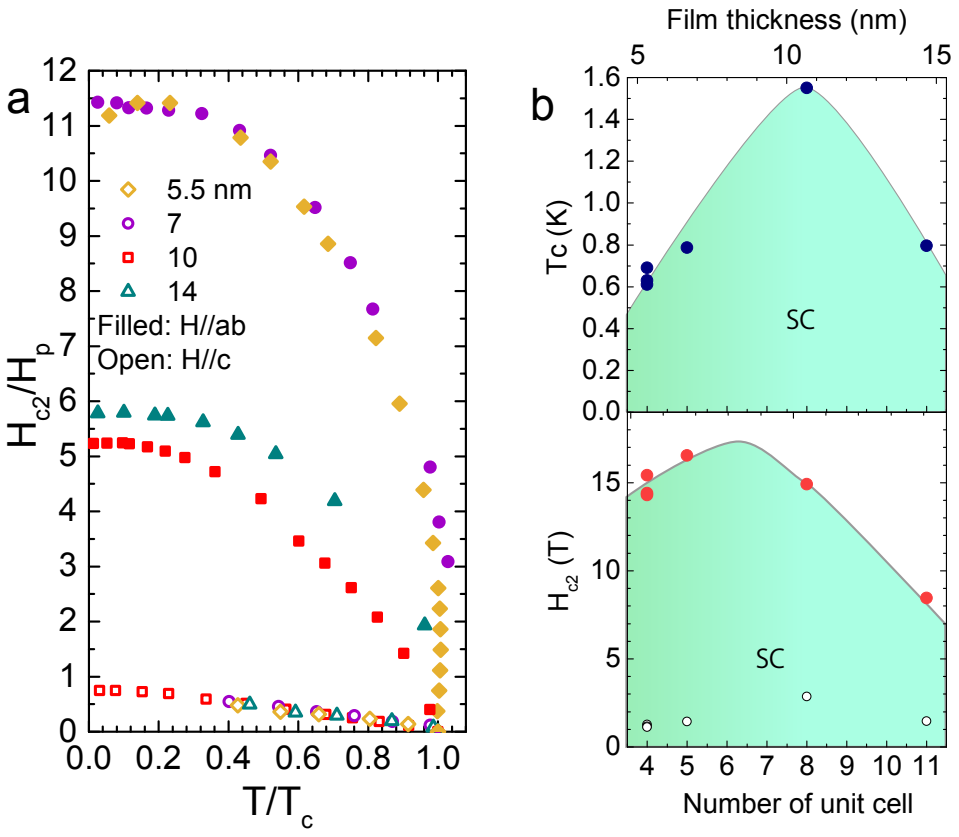

Figure 4.16: **Summary of H_{c2} and T_c from WTe_2 films.** (a) Phase diagram of H_{c2} vs T_c. (b) Thickness dependence of T_c (top) and H_{c2} (bottom).

4.2.5 Two dimensional features of WTe_2 thin films

4.2.5.1 Weak anti-localization

The normal state magnetoconductance curve from 10 nm film measured in Fig.4.9(g) is shown in Fig. 4.17 (a). The magnetic field is applied in-plane. The conductance shows a peak at zero magnetic field, suggesting a weak anti-localization (WAL). In this case, the applied magnetic field suppresses the enhanced conductivity from the destructive interference between time-reversed electron paths, resulting in the lower conductivity. The observation of WAL indicates that the system is strongly spin-orbit coupled and low-dimensional, as observed in typical TIs Bi_2Se_3 [101] or Bi_2Te_3 [102].

The WAL contribution can be fit by Hikami-Larkin-Nagaoka (HLN) theory [103] as

$$\Delta\sigma_{xx}(H) = \alpha\frac{e^2}{2\pi^2\hbar}\left[\ln\left(\frac{B_\phi}{B}\right) - \psi\left(\frac{1}{2}+\frac{B_\phi}{B}\right)\right] \tag{4.3}$$

where ψ is a digamma function, $B_\phi = \frac{\hbar}{4eL_\phi^2}$ and L_ϕ is a dephasing length, and $\alpha = \frac{1}{2}$ for each conduction channel. We obtained $\alpha = 1.16$ from $T = 5$ K fitting, which is close to the contribution from top and bottom surfaces, then fixed this value for fitting other temperature curves. The fitted curves are shown as dashed-lines in Fig. 4.17 (a). The observation of WAL is consistent with the flake WTe_2 measurements [104]. Fig. 4.17 (b) shows the temperature dependence of B_ϕ and L_ϕ.

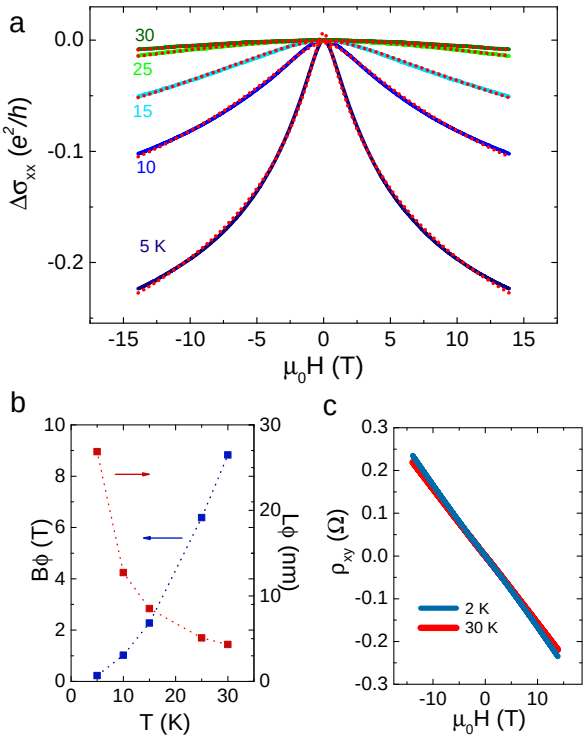

Figure 4.17: **Weak anti-localization from the 10nm WTe_2 film.** (a) Magneto-conductance at different temperatures above T_c. Dashed lines are the fitted curves using (4.3). (b) Temperature dependence of B_ϕ and L_ϕ. (c) Hall effect at 2 K and 30 K.

Also, in the bulk single crystals of WTe_2, very large, non-saturating MR was

observed [95], and it is explained by the perfect compensation of electron and hole pockets [105, 106]. We did not see such a large MR from all the WTe_2 films we measured. This could be due to the large doping effect. Fig. 4.17 (c) shows the Hall resistance at 2 K and 30 K up to 14 T. At both of temperatures, only one electron contribution was resolved, indicating that our thin films are highly electron-doped. The carrier density obtained from the Hall slope is about 3.3×10^{15} cm^{-2}.

4.2.5.2 Berezinskii–Kosterlitz–Thouless transition

Another feature indicating two-dimensionality is the Berezinskii–Kosterlitz–Thouless (BKT) transition [107, 108]. The superconducting transition in a two-dimensional system is a BKT transition, where the vortex-antivortex pairs unbind and the IV curve shows power-low dependence $V \propto I^{\alpha}$ rather than exponential behavior with $\alpha = 3$ at the BKT transition temperature T_{BKT} [109, 110, 111]. The IV curves from our samples are shown in Fig. 4.18 (a). The power-law behavior is observed at around the superconducting transition temperature. The exponent α vs temperature is shown in Fig. 4.18 (c), where α becomes 3 at T_{BKT} which is estimated to be 1.26 K. The observation of the BKT transition confirms that the system is two-dimensional.

4.2.5.3 Angular dependence

The angular dependence of H_{c2} also shows the two-dimensional feature. Shown in Fig. 4.19 is the angular dependence of H_{c2} from the 10 nm WTe_2 thin film at different magnetic field orientations and $T = 0.3$ K. The magnetic field was applied with the tilt angle θ from c-axis. The angular dependence of H_{c2} is well fit by the equation in two-dimensions [11]

$$\frac{H_{c2}(\phi)}{H_{c2\|c}} \cos\phi + \left(\frac{H_{c2}(\phi)}{H_{c2\|ab}} \sin\phi \right)^2 = 1. \tag{4.4}$$

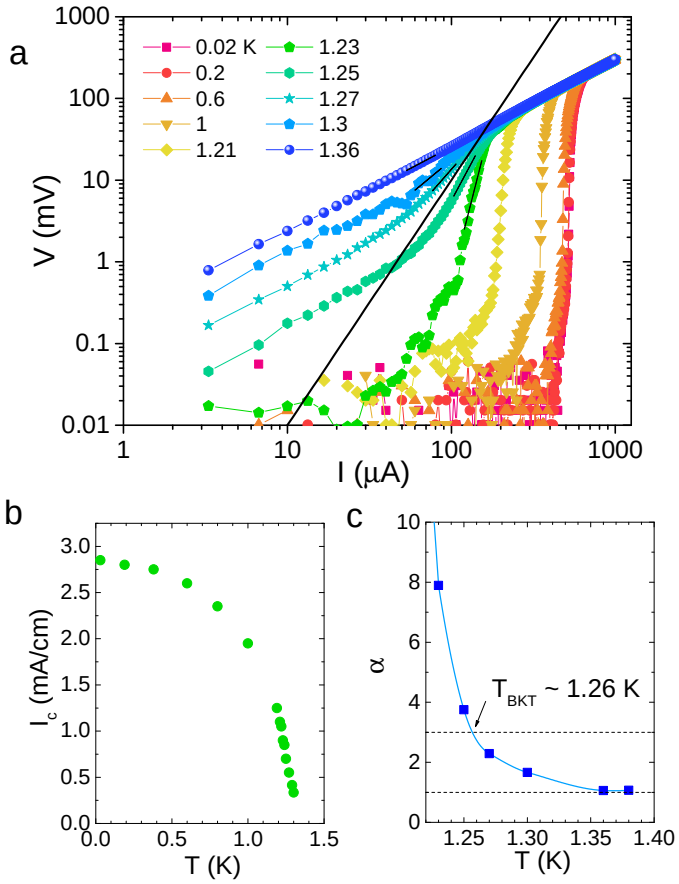

Figure 4.18: **Berezinskii–Kosterlitz–Thouless transition.** (a) Current dependence of voltage from the WTe_2 thin film on a logarithmic scale. (b) Temperature dependence of the critical current density I_c. (c) Temperature dependence of the exponent α.

There is a sharp cusp near $\theta = 90°$ (Fig. 4.19 (inset)), which is a two-dimensional feature. Because of this, we paid special attention to confirm that the magnetic field orientation is controlled stable and precise.

4.2.6 Fitting of Ising superconductivity

The H_{c2} vs T_c curve is fitted by the theoretical moedl of Ising superconductivity as following [81]

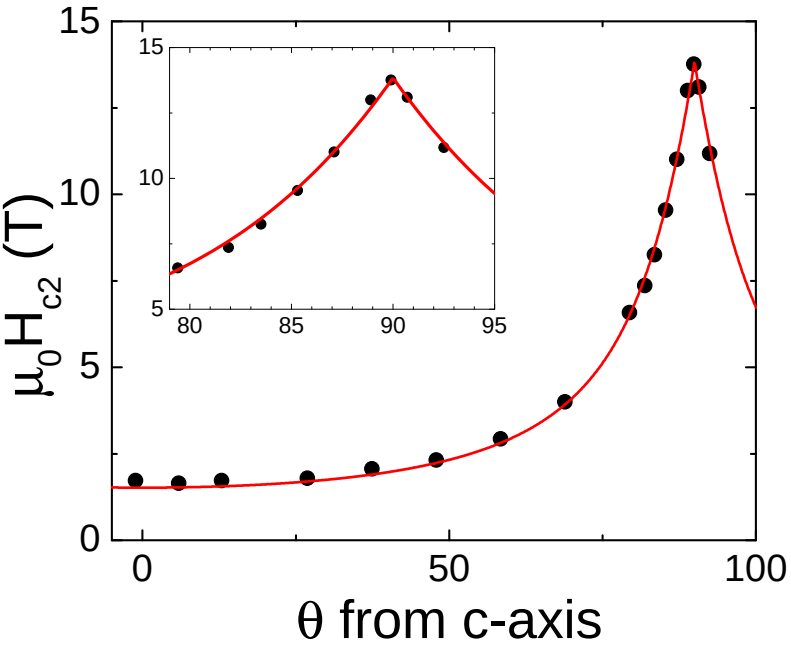

Figure 4.19: **Angular dependence of the upper critical field H_{c2}.** The data was taken at $T = 0.3$ and magnetic field with the tilt angle θ from c-axis. (inset) the expansion of the range near 90 degrees.

$$\ln\left(\frac{T_c}{T_{c0}}\right) + \Psi\left(\rho_-\right) + \Psi\left(\rho_+\right) + \left[\Psi\left(\rho_-\right) - \Psi\left(\rho_+\right)\right] \frac{\left(\mathbf{g_F} + \beta_{\mathbf{SO}}\right)^2 - \mathbf{b}^2}{|\mathbf{g_F} + \beta_{\mathbf{SO}} - \mathbf{b}||\mathbf{g_F} + \beta_{\mathbf{SO}} + \mathbf{b}|} = 0 \tag{4.5}$$

where

$$\rho_\pm = \frac{|\mathbf{g_F} + \beta_{\mathbf{SO}} + \mathbf{b}| \pm |\mathbf{g_F} + \beta_{\mathbf{SO}} - \mathbf{b}|}{2\pi T_c} \tag{4.6}$$

with parameters

$$\mathbf{b} = (\mu_B B_{c2}, 0, 0)\,, \mathbf{g_F} = (\alpha_F k_F, -\alpha_F k_F, 0)\,, \beta_{\mathbf{SO}} = (0, 0, \beta_{SO}) \tag{4.7}$$

and

$$\Psi\left(\rho\right) \equiv \frac{1}{2} Re\left[\psi\left(\frac{1+i\rho}{2}\right) - \psi\left(\frac{1}{2}\right)\right]. \tag{4.8}$$

The fitted H_{c2} vs T_c curve is shown in Fig. 4.20. The high-temperature feature

could be fit well by Eq. (4.5), though it does not explain the field enhancement of T_c. On the other hand, the non-monotonic behavior of H_{c2} vs T around zero temperature cannot be well fit by this model.

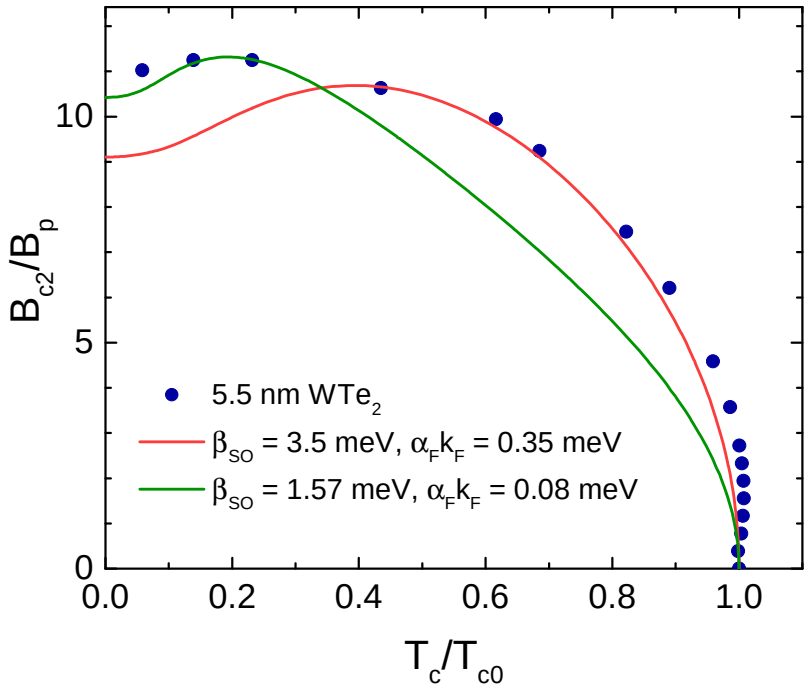

Figure 4.20: **Ising superconductivity fitting of the upper critical field H_{c2} vs T_c.** The fitting parameters are $\beta_{SO} = 3.5$ meV, $\alpha_f k_F = 0.35$ meV (red) and $\beta_{SO} = 1.57$ meV, $\alpha_f k_F = 0.08$ meV (green), respectively.

4.2.7 Discussion

First, we note that the enhancement of T_c under magnetic fields is not artificial but rather intrinsic. Near $T = T_c$, the negative MR corresponds to the enhancement of T_c. Since the magnetic field is applied in-plane, the classical parabolic MR should be negligible. Also, since the bulk WTe_2 is a Type II Weyl semimetal, the chiral anomaly effect is expected. However, the negative MR was observed even when the current is perpendicular to the magnetic field, eliminating this possibility. The thermometer was calibrated under magnetic fields, therefore the possibility of temperature misreading is excluded as well. Also, the negative MR was only observed around T_c, above which

the MR is always positive. Thus, we conclude that the negative MR originates from the enhanced superconductivity by the magnetic field.

Second, the non-monotonic behavior of H_{c2} vs T near zero temperature is also intrinsic rather than artificial. As shown in Fig. 4.19, the H_{c2} is very sensitive to the angle. Thus, at each temperature, we adjusted the magnetic field angle within 0.05 degrees from the surface of the samples. Also, we swept several curves at the same temperature to make sure that there is no angle misalignment induced during the field sweep. Thus, there is negligible angle misalignment effect in the results. The sample temperature was well controlled by the liquid He3/He4 surrounding the samples, eliminating the possibility of temperature drifting effect during sweeping. These results confirm that the non-monotonic behavior of H_{c2} vs T at the base temperature is intrinsic.

We next discuss the crystal structure of our thin films. As mentioned above, X-ray scattering result is consistent with the non-centrosymmetric T_d phase. If this is the case, the large value of H_{c2}/H_p is attributed to the Ising superconductivity. However, when the WTe_2 thin films are grown on Bi and MoS_2 substrates, the centrosymmetric 1T' phase was observed [112]. If this is the case, high H_{c2}/H_p could be possibly attributed to the p-wave superconducting pairing.

Unfortunately, it is difficult to determine the crystal structure of our samples since the lattice mismatch between the WTe_2 and sapphire substrate is very large. Therefore, even though the lattice constant relaxation is rapid, the error bar of the lattice constant smears out the peak splitting of the 1T' phase discussed in the previous chapter.

Another difference of our films compared to the bulk WTe_2 is the negligible MR above T_c. The Hall signal indicates that our samples are highly electron-doped. As mentioned, the origin of extremely large MR in bulk WTe_2 could originate from the perfect compensation of electrons and holes. Thus, if the system is doped, it is

reasonable that the MR becomes small. However, it is notable that in the pressure studies the MR decreases as the pressure increases and the system becomes close to the 1T' phase. Thus, further experiments on this system is desired to clarify the origin of our observation of unconventional superconductivity.

4.2.8 Summary

In summary, we have grown and measured thin films of WTe_2 on sapphire substrates. The in-plane H_{c2}/H_p is more than 10, which could be attributed to the Ising superconductivity. Also, at around T_c, the small in-plane magnetic field enhances T_c by 1.6 %. At high fields, the nonmonotonic H_{c2} vs T was observed, which could be understood by the competition of Zeeman term and Ising type SOC, consistent with the Ising superconductivity. X-ray result is consistent with the T_d crystal structure, but more experiments are desired to exactly determine the phase of this system.

CHAPTER V

Unconventional ferromagnetism in $LaNiO_3$ thin films on $LaAlO_3$ (111) substrate

5.1 Background

5.1.1 Honeycomb lattice on (111) bilayer

Transition metal oxides (TMO) have been intensively studied to understand various quantum phenomena of strongly correlated materials, such as metal-insulator transition, multiferroicity and high-temperature superconductivity [113, 114]. The advances in ultra-thin film growth with atomic precision further provide a wide control of lattice constant and geometrical confinement. Most of the previous studies on TMO thin films have been focused on systems grown along the (001) direction. Recently, several theoretical studies have shown that the bilayer TMO grown along (111) direction are promising candidates for realizing strongly correlated topological phases due to the presence of buckled graphene-like honeycomb lattice [115].

Fig. 5.1 (b)(c) shows the idea of buckled honeycomb lattice. When the heterostructure of perovskite compounds ABO_3 and $A'B'O_3$ are grown along [111] direction, each (111) bilayer atoms are located on a (bilayer) honeycomb lattice sites like graphene. Thus, as explained in Chapter I, the Dirac point is expected in the energy dispersion. While graphene is not correlated nor spin-orbit coupled, TMOs

are moderately r correlated and could have strong spin-orbit coupling. Thus, the topological features in TMOs is an interesting field.

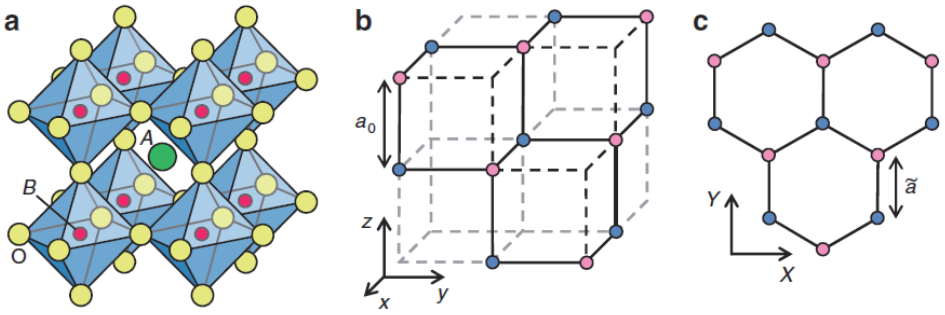

Figure 5.1: **Buckled honeycomb lattice in a (111) bilayer cubic system.** (a) Perovskite crystal structure. (b) Buckled honeycomb lattice formed by a (111) bilayer atoms. (c) The honeycomb lattice looked down from [111] direction. Adapted from [115].

5.1.2 Rare earth Nickelates

Among TMOs, in particular, lanthanum nickelate $LaNiO_3$ (LNO) has been theoretically studied intensively. $LaNiO_3$ belongs to rare earth nickelate family $RNiO_3$ (RNO), but LNO is the only metallic compound at all temperatures with non-magnetic ground state among $RNiO_3$ [116]. As shown in Fig. 5.2, Among R = Pr, Nd, Sm, and La, only $LaNiO_3$ is metallic and paramagnetic down to the base temperature.

The phase diagram of $RNiO_3$ as a function of ionic radius is shown in Fig. 5.3. As shown in the inset, $RNiO_3$ has a perovskite crystal structure. In general, the Ni-O-Ni bond angle θ is distorted and smaller than 180 degrees, due to the too small ionic radius of rare earth elements. As the ionic radius increases from Sm to La, also θ increases from 152.6° (Sm) to 165.2° (La), getting close to the cubic structure.

Since we are interested in the topological semimetal features, naturally we focus on $LaNiO_3$, the only conducting nickelate.

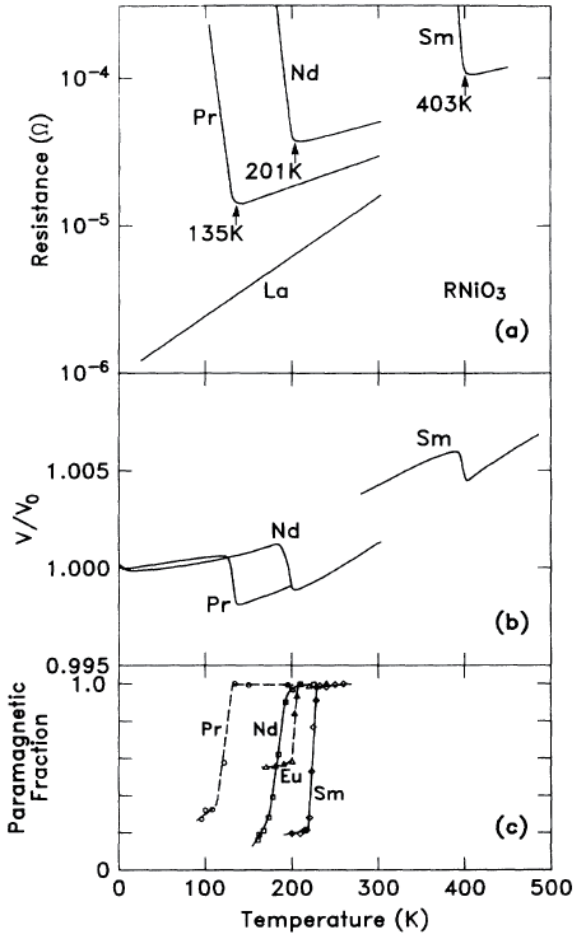

Figure 5.2: **Metal-to-insulator transition in $R\mathbf{NO}_3$.** (a)(b)(c) Temperature dependence of resistance, volume of the unit cell the paramagnetic fraction for $R\mathrm{NO}_3$, respectively. Adapted from [116].

5.1.3 $\mathrm{LaNiO_3/LaAlO_3}$ heterostructure

Many $\mathrm{LaNiO_3/LaAlO_3}$ (LNO/LAO) heterostructures are grown along (001) direction after the prediction of high T_c cuprate-like physics in this system [117, 118]. For (111) direction growth, recent theoretical calculations predict the possibility of topologically nontrivial interacting ground states such as quantum anomalous Hall effect and Dirac half semimetal, as well as multiferroicity (ferroelectricity and ferromagnetism) and metal-insulator transition [119, 120, 121, 122, 123].

For example, Doennig *et al.* showed that when $(\mathrm{LaNiO_3})_M/(\mathrm{LaAlO_3})_N$ het-

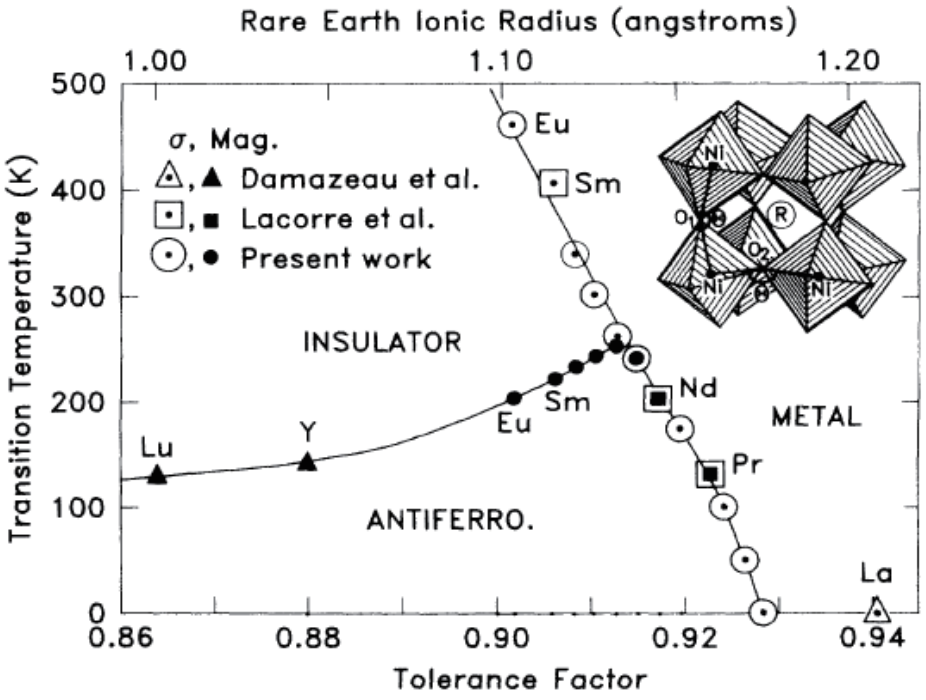

Figure 5.3: **Phase diagram of RNiO$_3$ (R = Sm, Nd, Pr, La, Eu) as a function of ionic radius.** Adapted from [116].

erostructure grown along [111] direction may have topological, ferromagnetic or ferroelectric features depending on M, N and the crystal symmetry. When M, N = (2,4), and the crystal symmetry is P321, the calculated band structure is shown in Fig. 5.4 (a). The system has Dirac point at K and K' points as similar to graphene. Also, the system is expected to be ferromagnetic despite that both of $LaNiO_3$ and $LaAlO_3$ are paramagnetic. On the other hand, if the system has P3 symmetry, the band has a gap at the K point and the system is multiferroic (ferroelectric and ferromagnetic) (Fig. 5.4).

Despite the intriguing theoretical predictions, however, experimental studies on (111) oriented RNO thin films have not been very successful due to the difficulty of growth along the strongly polarized (111) interface [124]. The first report on (LNO/LAO) superlattice shows insulating behavior rather than the expected Dirac semimetals [125]. The temperature dependence of resistivity for superlattices of

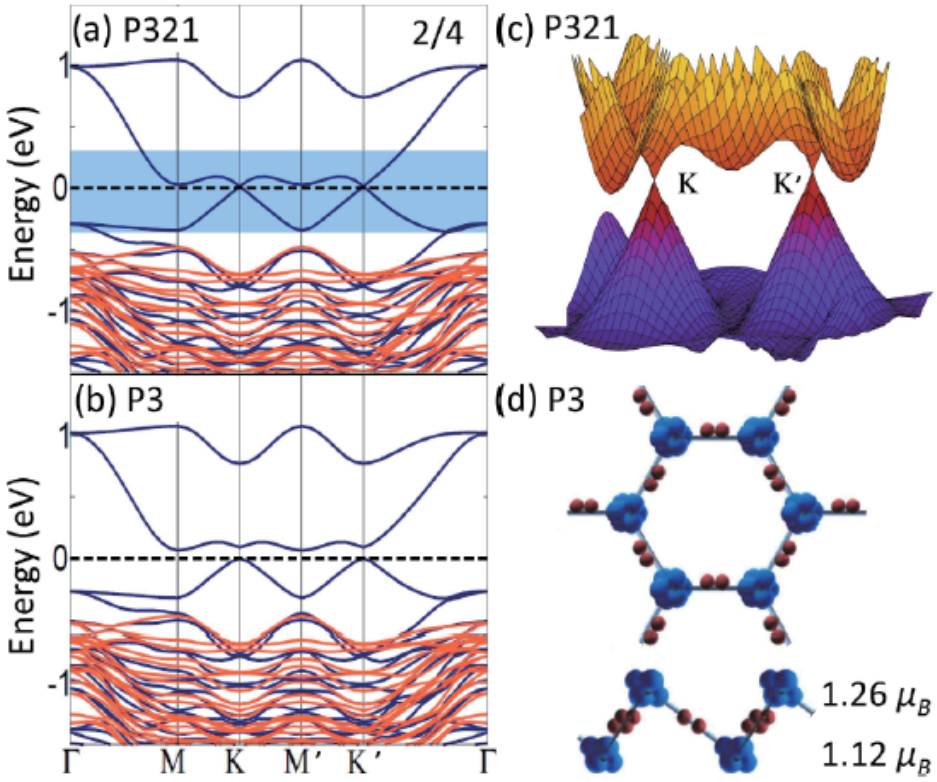

Figure 5.4: **Phase diagram of RNO$_3$ (R = Sm, Nd, Pr, La, Eu, Y, Lu) as a function of ionic radius.** Adapted from [123].

LNO$_M$/LAO$_N$ is shown in Fig. 5.5. For (M, N)=(1,1), (2,2), (2,3) and (2,4), all the samples show completely insulating behavior. Moreover, the superlattices (3,3) grown on LAO (001) also shows the insulating behavior. The activated gap E_g of (2,3) sample is obtained to be 95 meV by the fitting $\sigma \propto exp(-E_g/2k_BT)$.

More recently, LNO thin films grown on (111) LAO substrate have shown the polar metallic feature indicating ferroelectricity [126]. However, so far no experimental sign of topological features has been reported in the LNO system. Furthermore, while many theoretical calculations predict that the ferromagnetic phase is favored in LNO/LAO thin films [121, 123] (and even LSDA + U calculations predict bulk LNO ferromagnetism [127]), no ferromagnetic phase has been observed from LNO heterostructures except for ferromagnetic $LaMnO_3$ [128] or $CaMnO_3$ [129] superlat-

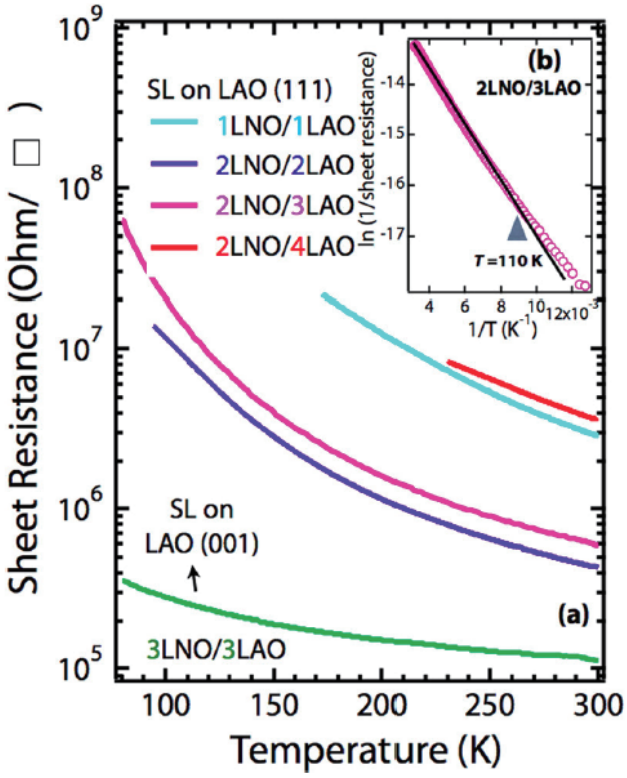

Figure 5.5: **Phase diagram of RNO$_3$ as a function of ionic radius.** Adapted from [125].

tice.

5.2 Results

In this section, we report the first observation of ferromagnetism from $LaNiO_3$ thin films grown on nonmagnetic $LaAlO_3$ (111) substrates. With the existence of a ferroelectric metal state reported before [126], LNO/LAO thin films exhibit multiferroicity, shedding light on the application of multiferroic metals. Moreover, positive linear magnetoresistance and the sign reversal of hysteresis loop have been observed. These features are consistent with the presence of Dirac point. The anisotropic magnetoresistance and planar Hall effect measurement further confirm the preserved C_3 symmetry, which is consistent with the theoretical prediction of ferromagnetic massive

Dirac state.

5.2.1 Hysteresis loop in magnetoresistance

Epitaxial LNO thin films were synthesized on LAO (111) and (001) substrates by the pulsed laser deposition (PLD) method where the film thickness can be in situ monitored during the PLD growth by a RHEED (Reflection High Energy Electron Diffraction) technique. The thickness of the as-grown LNO thin films is about 2.23 and 3.86 nm for the (111) and (001) samples, respectively. Since the unit-layer thickness is 0.223 and 0.386 nm in the pseudocubic (111) and (001) orientations, respectively, both LNO/LAO (111) and (001) thin films are 10-layer-thick. More details of the sample fabrication can be found in the previous literature [126].

Fig. 5.6 summarizes the angular and temperature dependence of magnetoresistance (MR) for the LNO/LAO(111) thin film. We have measured two samples and the similar behavior was observed. Fig. 5.6 (a) shows an angular dependence of MR measured at $T = 3$K. A clear butterfly-like hysteresis loop was observed at each angle. This is the first evidence of ferromagnetism in LNO/LAO(111). Focusing on the sign of the loop, at around 0 degree MR is larger when sweeping the magnetic field from zero, indicating that the resistivity is enhanced in the vicinity of the magnetization reversal. This is typical for most of the ferromagnets, as carriers are usually scattered by domain walls. However, at 30 degrees, there is a sign reversal of hysteresis loop at low fields, whereas at high fields, the domain wall contribution is still positive. Above 30 degrees the conductivity is totally enhanced by the domain wall. The similar behavior has been observed in ferromagnetic topological insulators [130] and topological Kondo insulators [131], and is attributed to chiral conducting modes mediated by the Dirac point.

The weird behavior of MR can be also observed in the temperature dependence, as shown in Fig. 5.6 (b) ($H\|$ c) and (c) (H $\|$ ab). In both orientation, while

between 3 K and 10 K the MR shows positive and sub-linear behavior at high fields, the MR becomes almost linear between 25 K and 50 K. Particularly, in $H \parallel$ ab configuration, the linear behavior continues down to zero fields, whereas in $H \parallel$ c configuration MR becomes rounded at zero fields. The angular dependence of linearity in ferromagnet is usually related to anisotropic magnetoresistance (AMR). When the magnetic field is applied parallel to the hard axis, MR is rounded near zero field due to slow magnetization saturation [132]. When the field is applied along the easy axis, AMR effect decreases and magnon suppression mechanism becomes dominant, resulting in linear MR. Thus, ab-plane is expected to be an easy axis (easy plane). However, in ferromagnetic materials, magnon suppression usually makes MR negatively linear, not positively.

Recently, it has been reported that ferromagnetic topological insulator $Cr_{0.15}(Bi_{0.1}Sb_{0.9})_{1.85}Te_3$ shows positive linear MR when the gate voltage is tuned so that the Fermi level lies near the Dirac point, while MR becomes negative when the Fermi level lies way below or above the Dirac point [133]. The strong connection between the Dirac point and positive linear MR in time-reversal-symmetry-broken materials is also indicated in one of the Dirac material candidate $Bi_2Ir_2O_7$ [134], which shows both hysteresis loop and positive linear MR.

We note the difference between $LaNiO_3$ thin films grown on $LaAlO_3$ (111) substrate and $LaAlO_3$ (001) substrate. The temperature dependence of resistance for both configurations is shown in Fig. 5.6 (d). LNO (001) thin film not only shows much smaller resistivity than LNO (111) thin films, it also shows the metallic temperature dependence down to $T = 20$ mK. This is consistent with the previous reports [135] and also similar to the bulk $LaNiO_3$, a paramagnetic metal. On the other hand, LNO/LAO(111) shows metal-insulator transition (MIT) at around 100 K. This kind of MIT has been observed in other $RNiO_3$ families, and indeed $LaNiO_3$ is the only metallic compound. Especially, in $NdNiO_3$ (NNO) thin film, MIT can be controlled

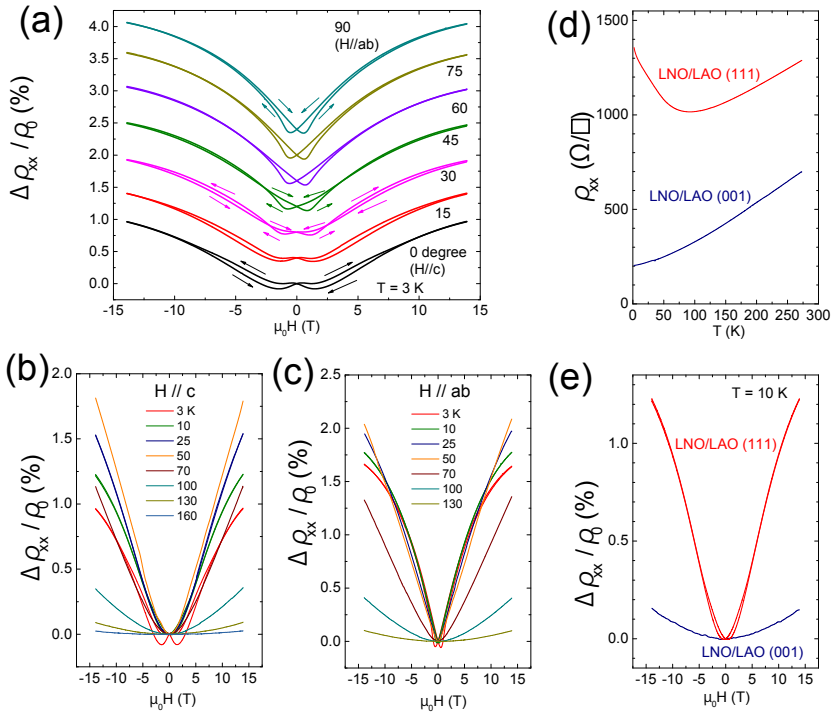

Figure 5.6: Angular and temperature dependence of magnetoresistance from $LaNiO_3/LaAlO_3$ thin film. (a) Angular dependence of normalized magnetoresistance $\Delta\rho_{xx}/\rho_0$ at T = 3K between 0 ($H \parallel c$) and 90 degrees ($H \parallel ab$). The curves are vertically displaced by 0.4 % for clarity. The arrows mark the direction of the increase of magnetic fields. The current is applied along the $[1\bar{1}0]$ direction, and the magnetic field H is applied always perpendicular to the current. (b)(c) Temperature dependence of $\Delta\rho_{xx}/\rho_0$ at out-of-plane (b) and in-plane (c) field orientations ranged from 3 to 130 K. (d)(e) Temperature (d) and out-of-plane magnetic field (e) dependence of ρ_{xx} for both LNO/LAO (111) and (001) configurations.

by the lattice mismatch between NNO and the substrate, and resistivity versus temperature curve shows small upturn on the boundary of metal and insulator phase [136]. We also note that the gapped behavior at low T is consistent with the predicted gapped Dirac semimetal. The MR behavior is also quite different between LNO/LAO (111) and LNO/LAO (001). In LNO/LAO(001), MR is one order of magnitude smaller than that from LNO/LAO (111) shown in Fig. 5.6 (e), and shows no linear behavior. This behavior is almost the same as bulk and thin film studies grown

on $LaAlO_3$ substrates reported previously [135], while negative MR was reported in $LaAlO_3$ thin films grown on SrTiO3 substrates [137].

5.2.2 Anomalous Hall effect

Another strong evidence of ferromagnetism is anomalous Hall effect (AHE). In a ferromagnetic material, ρ_{yx} is expressed as

$$\rho_{xy} = R_H B + \mu_0 R_s M \tag{5.1}$$

where R_H and R_s are ordinary and anomalous Hall coefficients. We display the angular dependence of the AHE at $T = 3$K in Fig. 5.7 (a). Clear large hysteresis loops are observed when the magnetic field is applied parallel to c-axis, while the anomalous Hall coefficient is quickly saturated at low fields when the magnetic field gets close to the plane. This is consistent with the easy-plane picture.

Temperature dependence of the AHE is shown in Fig. 5.7 (b). At $T = 25$K, the hysteresis loop becomes very small and at $T = 50$K no anomalous Hall component was observed, indicating that T_c is around 50 K. Above 50 K, ρ_{yx} is almost linear and the calculated carrier density is similar to one from the bulk $LaNiO_3$ or thin $LaNiO_3$ film grown on (001) $LaAlO_3$ (Fig. 5.7 (c)). This fact indicates that the doping effect by the lattice strain is relatively small, but rather the magnetism is affected by the symmetry of thin films, e.g., strain orientation. From the hysteresis loop and AHE, it is inferred that the system is ferromagnetic. However, the hysteresis loop, AHE, and positive MR could be also observed in antiferromagnetic or even nonmagnetic systems [138]. Thus, these possibilities cannot be ruled out.

The symmetry of the system could be reduced from undistorted P_{321} to P_3 or even fully distorted P_1 due to the strain, and it is predicted that the symmetry plays a key role on whether the system is Dirac material or multiferroic [123]. When the lattice is undistorted and in P_{321} symmetry, the system is predicted to be ferromagnetic

Dirac half-semimetal. With broken inversion symmetry due to the lattice strain, the symmetry is reduced to P_3 and the system becomes multiferroic (ferroelectric and ferromagnetic) with Dirac point gapped (massive Dirac). When the lattice symmetry is fully broken and becomes P1, the system is still multiferroic and gapped, but Dirac point no longer exists. Thus, it is important to check if the symmetry of the system (especially C_3) is broken or not.

5.2.3 Anisotropic magnetoresistance and planar Hall effect

To solve this issue, we have measured in-plane AMR and planar Hall effect (PHE). In poly crystals, the angular dependence of AMR and PHE depends on the angle between the current and magnetic field and is dominated by two-fold components. However, in crystalline system, AMR only depends on θ and ϕ, where θ (ϕ) is the angle between magnetic field (current) and certain crystal axis ($[1\bar{1}0]$ for our case). The angular dependence of AMR $\Delta\rho_{xx}(\theta,\phi)$ reflects the crystal symmetry. For a hexagonal system [139], $\Delta\rho_{xx}(\theta,\phi)$ is given by

$$\Delta\rho_{xx}(\theta,\phi) = C_2\cos(2\theta-2\phi) + C_4\cos(4\theta+2\phi) + C_6\cos(6\theta). \tag{5.2}$$

where C_2, C_4 and C_6 are AMR coefficients for two-, four- and six-fold components. Similarly, the angular dependence of PHE in a hexagonal system is given by

$$\Delta\rho_{yx}(\theta,\phi) = C_2\sin(2\theta-2\phi) - C_4\sin(4\theta+2\phi). \tag{5.3}$$

Note that the six-fold component vanishes in PHE.

The angular dependence of ρ_{xx} and ρ_{yx} with $H = 14$T at different temperatures are shown in Fig. 5.8 (a)-(f). At temperatures lower than $T = 25$K, the angle sweep-up and sweep-down show different behavior, indicating that the magnetization is not fully polarized. At higher T, both of AMR and PHE are fit well by Eq. 5.2

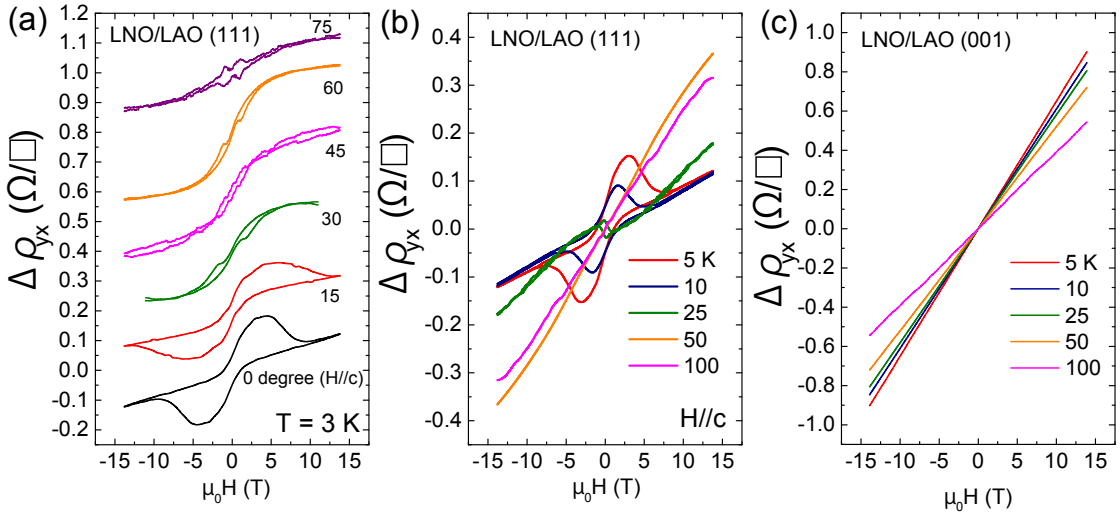

Figure 5.7: Anomalous Hall effect from $LaNiO_3/LaAlO_3$ (111) and (001) thin films. (a) Angular dependence of AHE with applied magnetic field tilted from 0 to 75 degrees, taken at $T = 3$K. Curves are displaced by 0.2 Ω/square for clarity .(b) Hysteresis loops of ρ_{yx} at selected T. The magnetic field is applied perpendicular to the film plane. (c) ρ_{yx} at selected T from LNO/LAO (001).

and 5.3. Particularly, below $T = 50$K the six- (four-) fold component was clearly observed in AMR (PHE), while above $T = 60$K the signal is dominated by two-fold component, indicating that the critical temperature is around $T = 60$K, consistent with AHE measurements. This is more clearly seen in fast Fourier transform (FFT) plots (Fig. 5.8 (g)(h)). Furthermore, the six-fold component shown in AMR but not in PHE indicates the presence of C_3 symmetry. This is consistent with P321 or P3 symmetry, with which the theory predicts the existence of Dirac point [123]. However, it contradicts with the monoclinic symmetry with three equivalent domains determined by the optical second-harmonic generation measurement [126]. Another possibility is that the angular dependence of AMR and PHE results from a domain distribution.

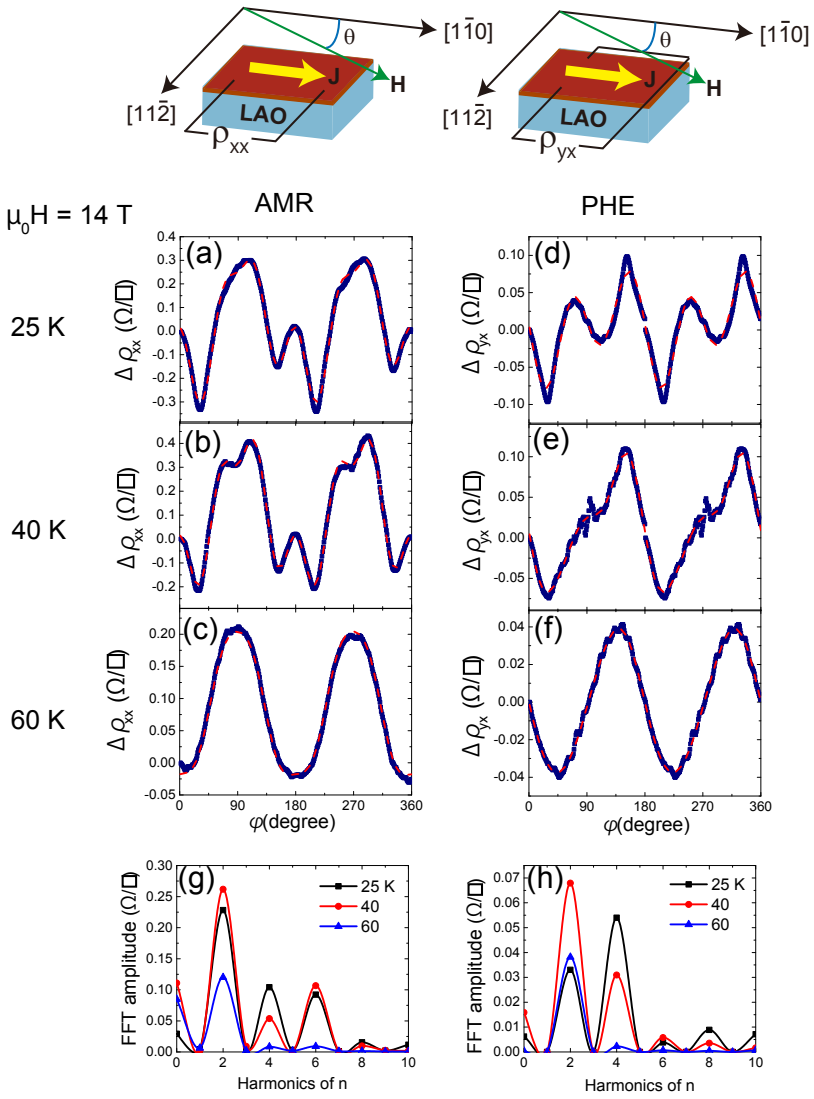

Figure 5.8: Anisotropic magnetoresistance and planar Hall effect at selected T. (a)-(c) Angular dependence of anisotropic magnetoresistance at T = 25, 40 and 60 K, respectively. The current is applied to [1$\bar{1}$0] direction. The magnetic field is applied in-plane with angle θ from the [1$\bar{1}$0] axis. Red dashed lines are fitting curves using Eq. 5.2. Fitting parameter of ϕ is around 4 degrees, indicating the misalignment between the current and the [1$\bar{1}$0] axis. (d)-(f) Angular dependence of Planar Hall effect with the same condition as AMR. Red dashed lines are fitting curves using Eq. 5.3. Due to small out-of-plane misalignment ($\sim$ 1 degree), the signal was symmetrized to eliminate the contribution from ordinary and anomalous Hall effect. (g)(h) Fast Fournier Transformation (FFT) plot of the data in (a)-(f) displays as a function of harmonic numbers.

5.2.4 Discussion

The positive linear MR observed in $H \parallel ab$ orientation is striking, since it excludes the most of the possibilities related to quantum interference. It is known that the two-dimensional disorder-induced quantum interference has a $\ln B$ dependence of magnetic field. Thus, the combination of $\ln B$ and parabolic MR from classical orbital effect could result in the linear behavior of MR. However, since the magnetic field is applied in-plane, classical MR contribution cannot be large. Also, weak localization and weak anti-localization can be ruled out, as they are considered to be orbital effect and highly affected by perpendicular component of H. Nevertheless, the in-plane MR is even larger than that from out-of-plane in our case. Furthermore, given that LNO/LAO (001) shows one order of magnitude smaller MR with no linear behavior, it is hard to think that the disorder effect is dominant in LNO/LAO(111). Thus, we can rule out this possibility.

Linear positive MR has been also reported in thin ferromagnetic films [140]. In this case, linear MR originates from disorder, and it should be isotropic. Again, this contradicts with our angular dependence of MR. Therefore this possibility can be ruled out as well, and we conclude that the positive linear MR comes from the intrinsic effect.

From the theoretical prediction, the LNO/LAO (111) system with P_3 symmetry becomes multiferroic with gapped Dirac point. All our observations are consistent with this picture: sign reversal of hysteresis loop, positive linear MR, ferromagnetic and ferroelectric features, the gapped behavior of temperature dependence of resistivity at low T and C_3 symmetry observed in in-plane AMR. Surprisingly, however, in $NdNiO_3/LaAlO_3$ (111) and $LaNiO_3/LaAlO_3$ (111)thin films, the rotational symmetry as well as inversion symmetry is found to be broken [126]. There are a few explanations. First, it is possible that the AMR and PHE could not tell the difference between P_3 and P_c (monoclinic) with three equivalent domain variants with the angle

of 120 degrees between each domain. Since the origin of AMR is the spin-dependent scattering of conducting electrons lead by spin-orbit coupling, its length scale could be longer than the domain size. In this case, the theory predicts that the system is still multiferroic, but the Dirac point no longer exists. Also, it is possible that the system is partially detwinned by the magnetic field, similar to that observed in iron-based superconductors [141, 142]. If this is the case, the calculation predicts that gap opening happens at the K point.

Finally, it is worth pointing out the electron-driven parity-breaking phase as a possible origin of multiferroicity in LNO/LAO (111). A similar ferroelectric metal phase has been reported in the bulk $LiOsO_3$ [143], accompanied by the structural transition at 140 K where the inversion symmetry disappears. This effect is argued to originate from the inversion symmetry breaking induced by the electron correlation in spin-orbit-coupled correlated metals [144]. In the theory, the p-wave spin-spin interaction leads to spin-split Fermi surfaces and gives rise to a polarization of electrons. Similarly, in LNO/LAO (111), despite the C_3 symmetry of LAO substrate, the inversion symmetry is broken up to room temperature, which leads to ferroelectricity [126]. The transition is accompanied by the Fermi surface spin splitting, which lays the foundation for the magnetic ordering.

In summary, we first observed the ferromagnetic state of $LaNiO_3$ thin film grown on $LaAlO_3$ (111) substrate as predicted by many groups. This result is important not only because it gives further guidance to improve the theoretical calculation, but also, with the ferroelectric feature reported before, it sheds light on the application to the spintronics. Moreover, our results are consistent with the existence of gapped Dirac point predicted by the theory. These results would be a significant step forward in the realization of strongly correlated topological phase by geometrical engineering of buckled honeycomb lattice.

CHAPTER VI

Conclusion

In this study, we investigated the three materials, $Nb_xBi_2Se_3$, WTe_2 thin films on sapphire substrates and $LaAlO_3$ thin films grown on $LaAlO_3$ (111) substrates. They are expected to belong to three different classes of topological materials: topological superconductors, Weyl semimetals and Dirac semimetals.

In Nb-doped Bi_2Se_3, we have observed the nematic order in the superconducting state of Nb-Bi_2Se_3 by in-plane torque magnetometry which is a thermodynamic probe. Either hysteresis loop or magnetic susceptibility show nematicity in the superconducting state, while in the normal state the angular dependence of susceptibility is a function of sin 6ϕ, indicating that the rotational symmetry is preserved. Furthermore, we revealed that the in-plane quantum oscillation frequency shows two-fold symmetry rather than six-fold. This is consistent with the theoretical prediction that the origin of nematicity is an in-plane strain. Further in-plane Fermiology study will nail down what is the driving force of strain.

In the thin films of WTe_2 grown on sapphire substrates, I observed that the in-plane upper critical field H_{c2} is more than 10 times larger than the Pauli limit H_p, indicating the Ising superconductivity in this system. Also, at around T_c, the small in-plane magnetic field enhances T_c by 1.6 %. At high fields, the nonmonotonic H_{c2} vs T was observed, which could be understood by the competition of Zeeman term and

Ising type SOC, consistent with the Ising superconductivity. X-ray result is consistent with the T_d crystal structure, but more experiments are desired to exactly determine the phase of this system.

In $LaNiO_3$ thin films grown on $LaAlO_3$ (111), we first observed the ferromagnetic state as predicted by many groups. This result is significant not only because it gives further guidance to improve the theoretical calculation, but also, with the ferroelectric feature reported before, it sheds light on the application to the spintronics. Moreover, our results are consistent with the existence of gapped Dirac point predicted by the theory. These results would be a significant step forward in the realization of strongly correlated topological phase by geometrical engineering of buckled honeycomb lattice.

These results will help further understand the exotic features of topological materials. In particular, the combination of topology and correlation or superconductivity is quite a new field. The observation of nematic superconductivity, field-enhanced T_c and magnetic Dirac physics would be a hallmark for this field.

APPENDICES

APPENDIX A

Pauli susceptibility in spin liquid herbertsmithite

In this appendix, I describe our torque magnetometry results on the spin liquid material herbertsmithite.

A.1 Background

When the strong geometric frustration exists in the antiferromagnetic system, the ground state may have no magnetic ordering. This phase is called the quantum spin liquid state. The most promising playground for the spin liquid is the $S = 1/2$ Heisenberg antiferromagnet in the kagome lattice because of the strong frustration [145, 146, 147]. In particular, herbertsmithite $ZnCu_3(OH)_6Cl_2$ consists of Kagome planes of spin $S = 1/2$ Cu^{2+} atoms separated by non-magnetic Zn atoms, making it ideal to study the spin liquid state [148]. Despite the large superexchange interaction of $J = 17$ meV, no magnetic ordering was observed down to 50 mK[149, 150]. Furthermore, recent neutron scattering measurement shows that the spin excitations form a continuum, indicating the fractional spinon excitation in this system [151].

In this appendix, I show that the susceptibility in the high field gapless ground state of herbertsmithite exhibit the Pauli susceptibility, indicating the spin liquid state.

A.2 Sample preperation Single crystals of herbertsmithite were grown from

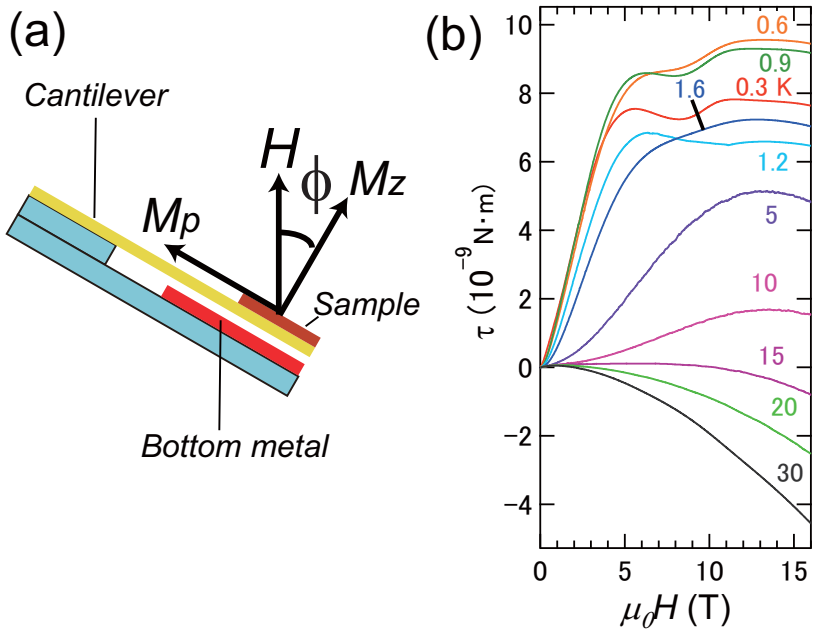

Figure A.1: **Torque curves on herbertsmithite.** (a) The schematic of torque magnetometry setup. (b) Temperature dependence of torque at $\theta = 20$ °.

powder samples. As described in Ref. [152], the powder samples were grown by sealing the parent compounds in a quartz tube, then they were transported in a three-zone furnace under a temperature gradient. In this study, two samples (sample A, B) were measured. The sample volumes are $0.3 \times 0.3 \times 0.4$ mm^3 $0.1 \times 0.1 \times 0.2$ mm^3, respectively. The X-ray diffraction indicates that, while about 15% of interlayer Zn atoms are replaced by Cu atoms in sample A, and 25% in sample B, no Zn atom sits in the Cu site, resulting in the perfect Cu kagome plane. In the results below, we mainly focused on sample A unless mentioned otherwise.

A.3 Temperature dependence of torque at low fields

The torque magnetometry setup is shown in Fig. A.1 (a). The single crystal of herbertsmithite was mounted on the cantilever with ab plane facing up. The magnetic field is applied with tilt angle θ from c-axis. Fig. A.1 (b) shows the example torque curves at different temperatures with $\theta = 20°$. At low temperatures, the Currie-like impurity contribution is dominant at low fields, while at high fields it is fully

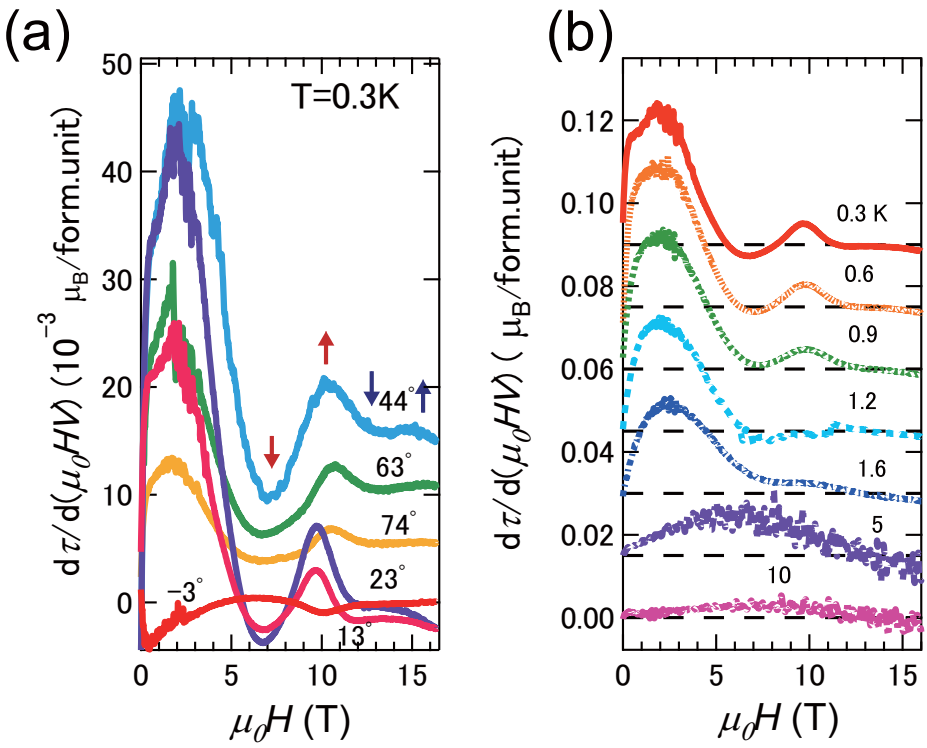

Figure A.2: **Derivative of torque as a function of magnetitic field. (a) Angular dependence (b) Temperature dependence**

saturated and the contribution from the intrinsic kagome plane becomes dominant. The impurity contribution decreases as the temperature increases and at around $T =$ 15 K the torque sign changes. This is consistent with the previous study[**?** 153]. At 30 K,, the curve is almost parabolic, indicating the whole system is paramagnetic.

A.4 Anomalies in low field torque

As shown in Fig. A.1 (b), there is a non-monotonic behavior of torque at low temperatures. These field-driven anomalies are observed at low temperatures and low fields, around the region where the impurity contribution saturates. Fig. A.2 (a) shows the derivative of torque as a function of the magnetic field to emphasize the anomalies, at different angles and $T = 0.3$ K. As indicated by the blue and red arrows, two pairs of anomalies were observed between $H = 7$ T and 15 T. Furthermore, the positions of the peaks are almost angular dependent, which is consistent with the isotropic Heisenberg model.

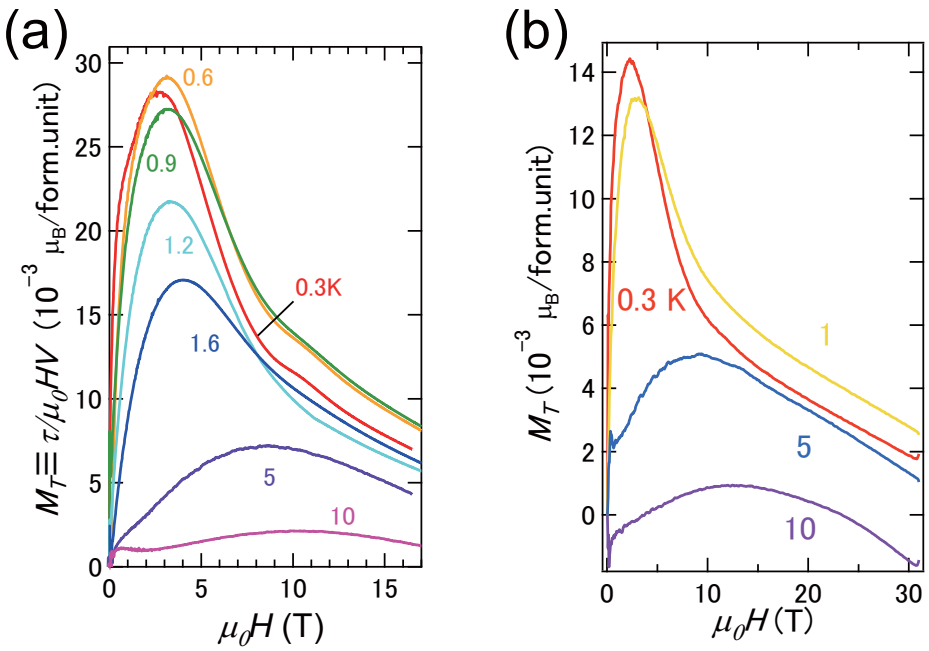

Figure A.3: **Field dependence of effective magnetization.** (a) Data taken up to 18 T. (b) Measured up to 31 T.

The temperature dependence of anomalies from 0.3 K to 10 K at $\theta = 20\,^\circ$ is shown in Fig. A.2 (b). The locations of anomalies are also temperature dependent up to T = 0.9 K, above which the anomalies disappear. This trend is also observed in sample B.

A.5 Pauli susceptibility in herbertsmithite

As the torque τ is given by $\tau = VM \times \mu_0 H$, the effective transverse magnetization M_T is given by $M_T = \frac{\tau}{\mu_0 HV}$. The temperature dependence of M_T up to 17 T is shown in Fig. A.3 (a). At higher fields above 10 T, the slope of M_T becomes almost linear with fields, indicating that the impurity magnetic moment is saturated and the contribution from kagome plane is dominant. The similar behavior is also observed from sample B. Shown in Fig. A.3 (b) is the M_T vs magnetic fields plot up to 31 T at 0.3, 1, 5 and 10 K form sample B. The high field slope is almost independent of temperature, indicating the Pauli susceptibility. To further illustrate this, the effective magnetic susceptibility $\chi_{eff} = dM_T/d\mu_0 H$ as a function of the magnetic

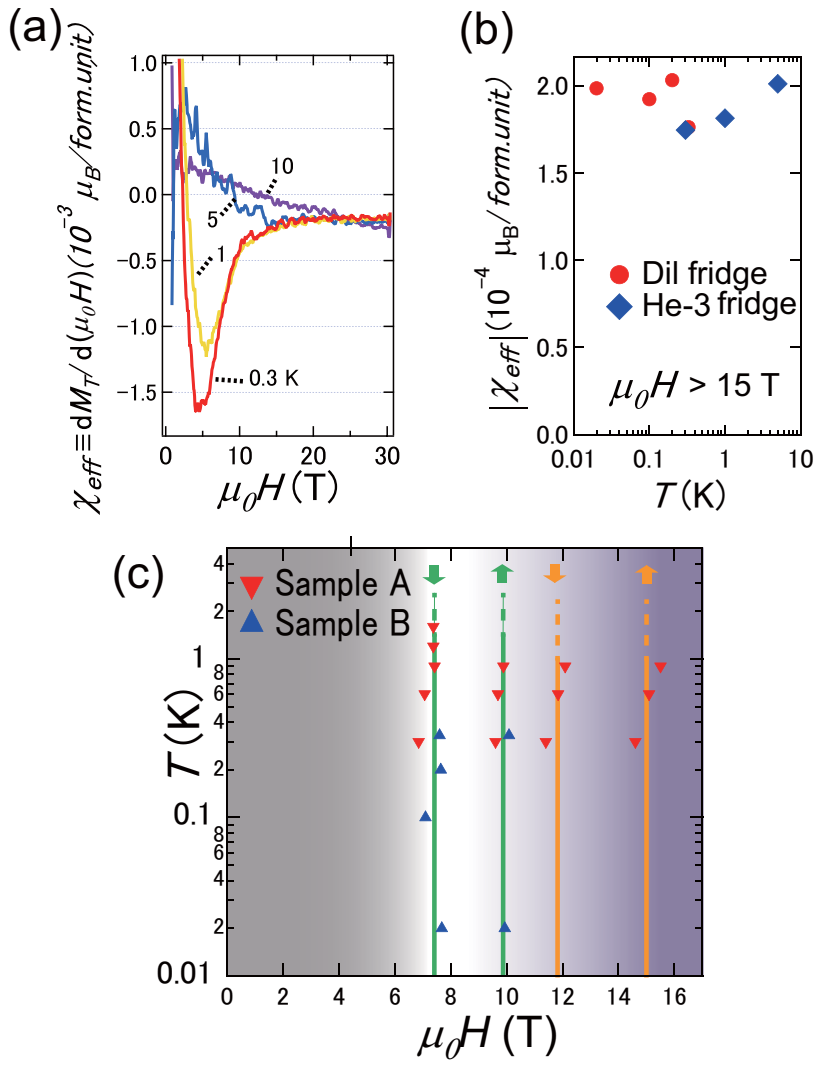

Figure A.4: **Phase diagram of herbertsmithite.**

field is shown in Fig. A.4 (a), using the data in Fig. A.3 (b). At $T = 0.3$, 1 and 5 K, χ_{eff} becomes constant and field-independent above 15 T.

The high field χ_{eff} vs temperature plot is sown in Fig. A.4 (b). It is almost constant between 0.02 K and 10 K, suggesting the Pauli susceptibility from spinon Fermi surface.

A.6 Phase diagram of herbertsmithite by torque magnetometry

Finally, the phase diagram of herbertsmithite is shown in Fig. A.4 (c). Between 8 and 16 T, we observed the anomalies in the torque between 20 mK and 1.6 K. Above

16 T and low temperatures, the impurity magnetic moment is fully saturated, and the signal originates from the intrinsic kagome contribution.

APPENDIX B

Quantum oscillations in a pyrochlore superconductor $Cd_2Re_2O_7$

B.1 Background

$Cd_2Re_2O_7$ is the first pyrochlore superconductor with $T_c = 1$ K [154]. When the sample is cooled down from room temperature, there is a crystal structural transition from cubic $Fd\bar{3}m$ phase to non-centrosymmetric tetragonal $I\bar{4}m2$ phase at $T_{s1} = 200$ K. After that, there is another structural transition to tetragonal $I4_122$ phase at $T_{s2} = 120$ K. Surprisingly, while the electronic properties dramatically change below T_{s1}, the lattice constant change is less than 0.01 % across T_{s1} [155] (Fig. B.1), indicating that the phase transition is driven by the electron correlation. Recently, this behavior was explained by Fu as the spin-orbit-coupling-driven phase transition into the multipolar order [144]. The multipolar behavior was recently confirmed by Harter *et al.* using optical second harmonic generation techniques [156]. Another important consequence of the multipolar order is the Fermi-surface splitting by the spin-orbit coupling. However, no Fermiology studies have been made on this compound so far. In this appendix, I provide the evidence of the spin-split Fermi surface by dHvA and SdH quantum oscillations.

B.2 dHvA oscillations at low fields

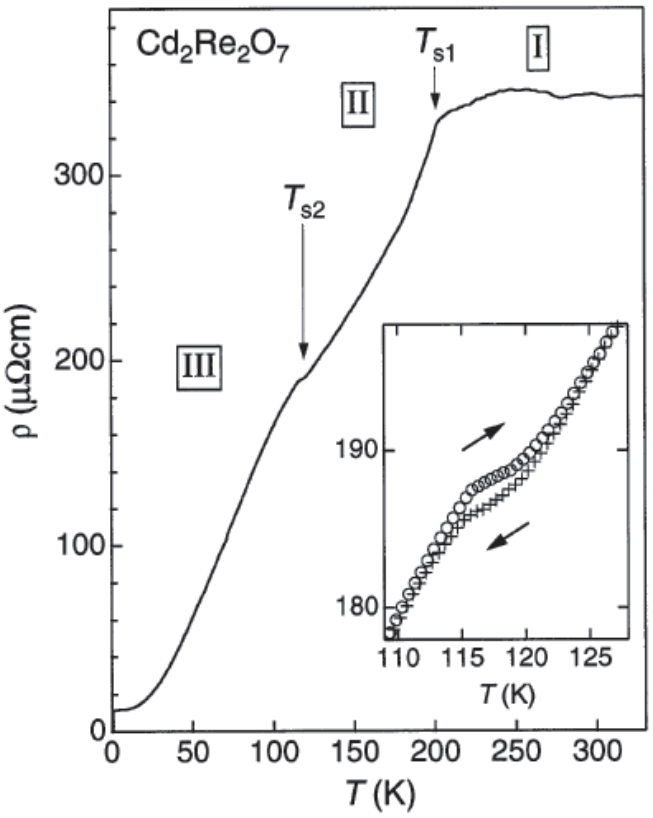

Figure B.1: **Temperature dependence of resistivity from $Cd_2Re_2O_7$.** (inset) The first order phase transition at around 120 K. Adapted from [155].

In this section, I describe the torque response up to 18 T, relatively low field features. The similar setup as described in Chap. III was used to observe the dHvA effect. Since only (111) surface is the well-defined surface obtained from $Cd_2Re_2O_7$, we applied the magnetic field in (110) plane so as to cover three high-symmetry axes, [110], [001] and [111]. The typical torque curve is shown in Fig. B.2. At low fields, the superconducting hysteresis loop was observed, consistent with the previous studies. The clear quantum oscillations were observed above 4-5 T.

The angular dependence of torque is shown in Fig. B.3 (a). The FFT plot of Fig. B.3 (a) after background subtraction is shown in Fig. B.3 (b). The dominant frequencies are below 100 T. Higher branches of 300-500 T is also apparent for most

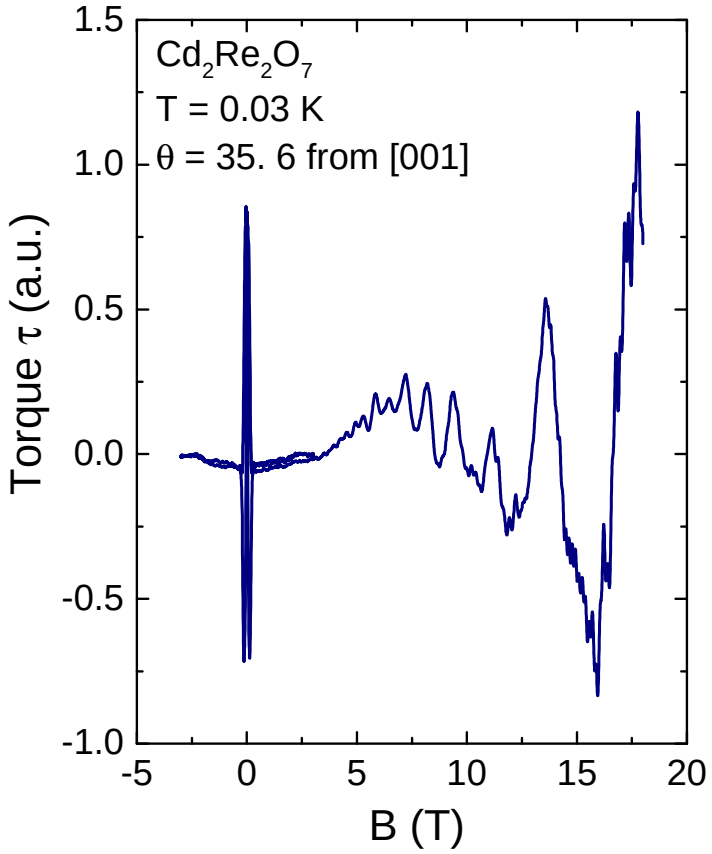

Figure B.2: **Example torque curve up to 18 T.**

of the frequencies, and even higher frequencies of 1.5-2.5 kT were also observed in certain angles.

In addition, we observed a hysteresis loop at around 2 T, way above the upper critical fields, as shown in The origin of this hysteresis is not clear. If the hysteresis loop is intrinsic, then it indicates that there is a first-order phase transition. Thus, further study is desired to determine if this phase transition is indeed a crystal structural transition or not.

B.3 dHvA oscillations at high fields

To further nail down the high-frequency behavior, we applied up to 45 T in the

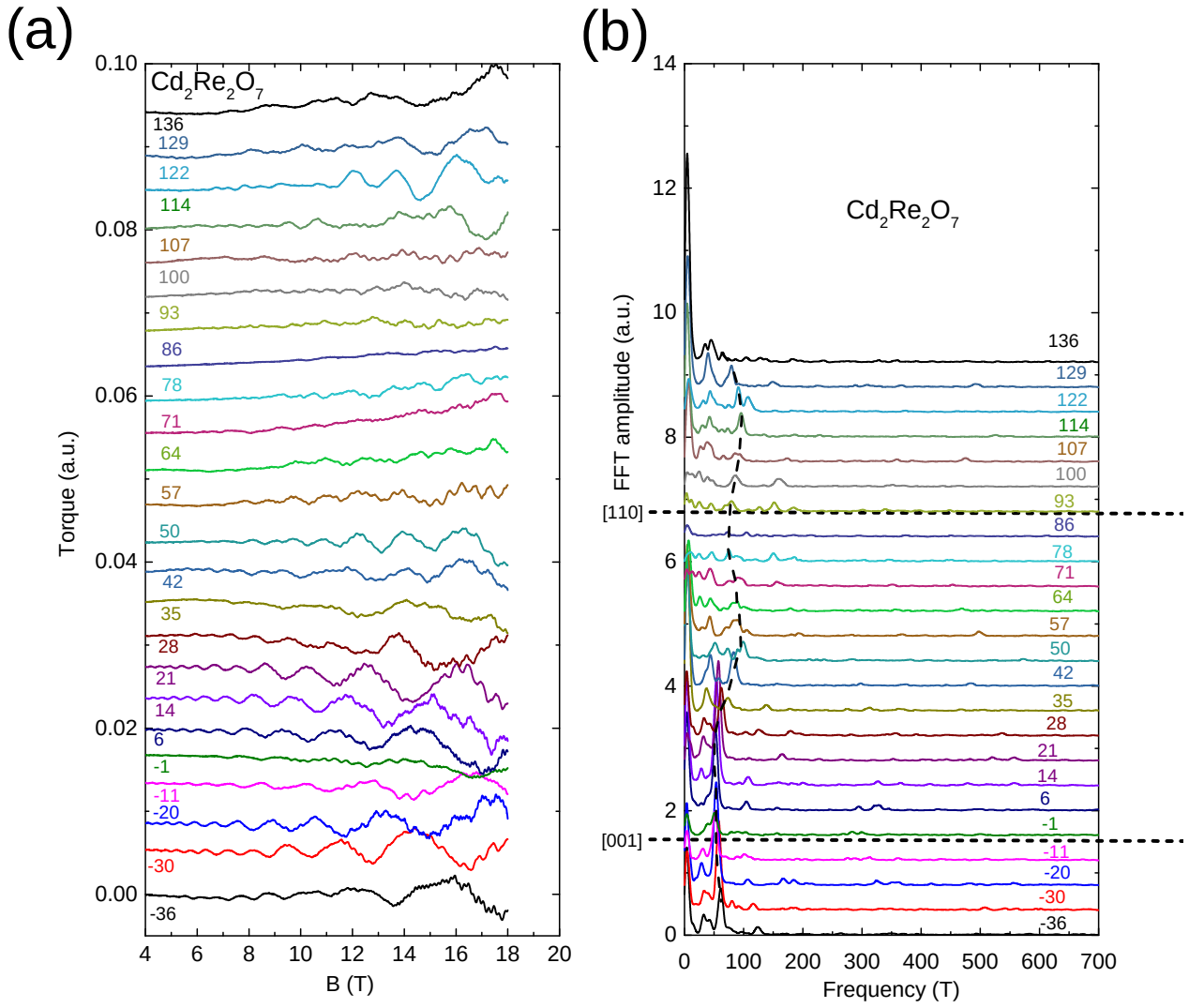

Figure B.3: **Low field torque and FFT plots.** (a) Torque curves. (b) FFT plots. The used data range is between 15 T and 45 T. The magnetic field was applied within the $(1\bar{1}0)$ plane.

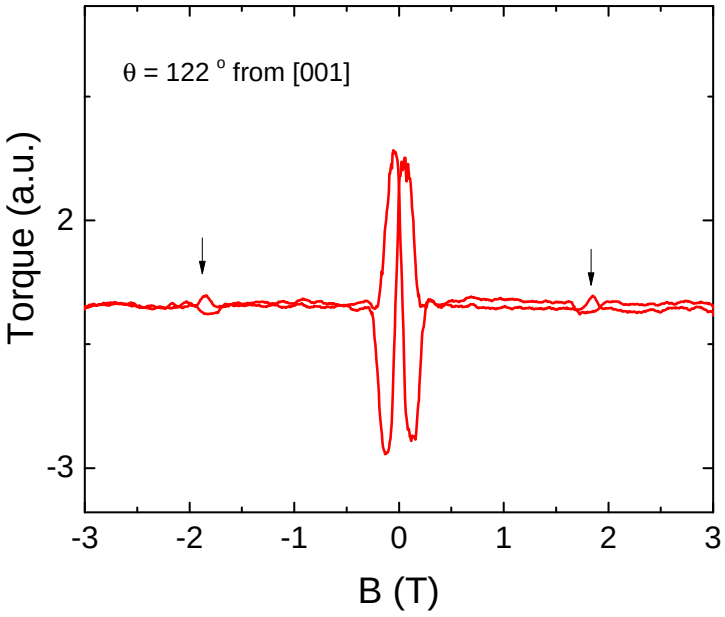

Figure B.4: **Additional hysteresis loop at 2 T.**

hybrid magnet in National High Magnetic Field, Tallahassee. The angular dependence of torque after background subtraction and the FFT data are shown in Fig. B.5 (a) and (b). Due to the higher fields, the higher frequencies are clearly resolved around 800 T, 1.5 kT and above 2 kT. In particular, when $\theta = 58$ degrees, which is close to [111] axis, there are multiple frequencies observed between 2 kT and 2.5 kT. At low temperatures, the crystal structure becomes tetragonal and there are three equivalent domains. However, when the magnetic field is applied parallel to [111] axis (in the cubic state), the quantum oscillations from three domains become identical. Multiple frequencies are consistent with this picture, and also they indicate the existence of the spin-split Fermi surface.

We also measured the temperature dependence of FFT amplitude of quantum oscillation to evaluate the effective mass of each pocket as shown in Fig. B.6.

B.4 SdH oscillations at pulse fields

Since the magnetization measurement picks up all the signals from the sample,

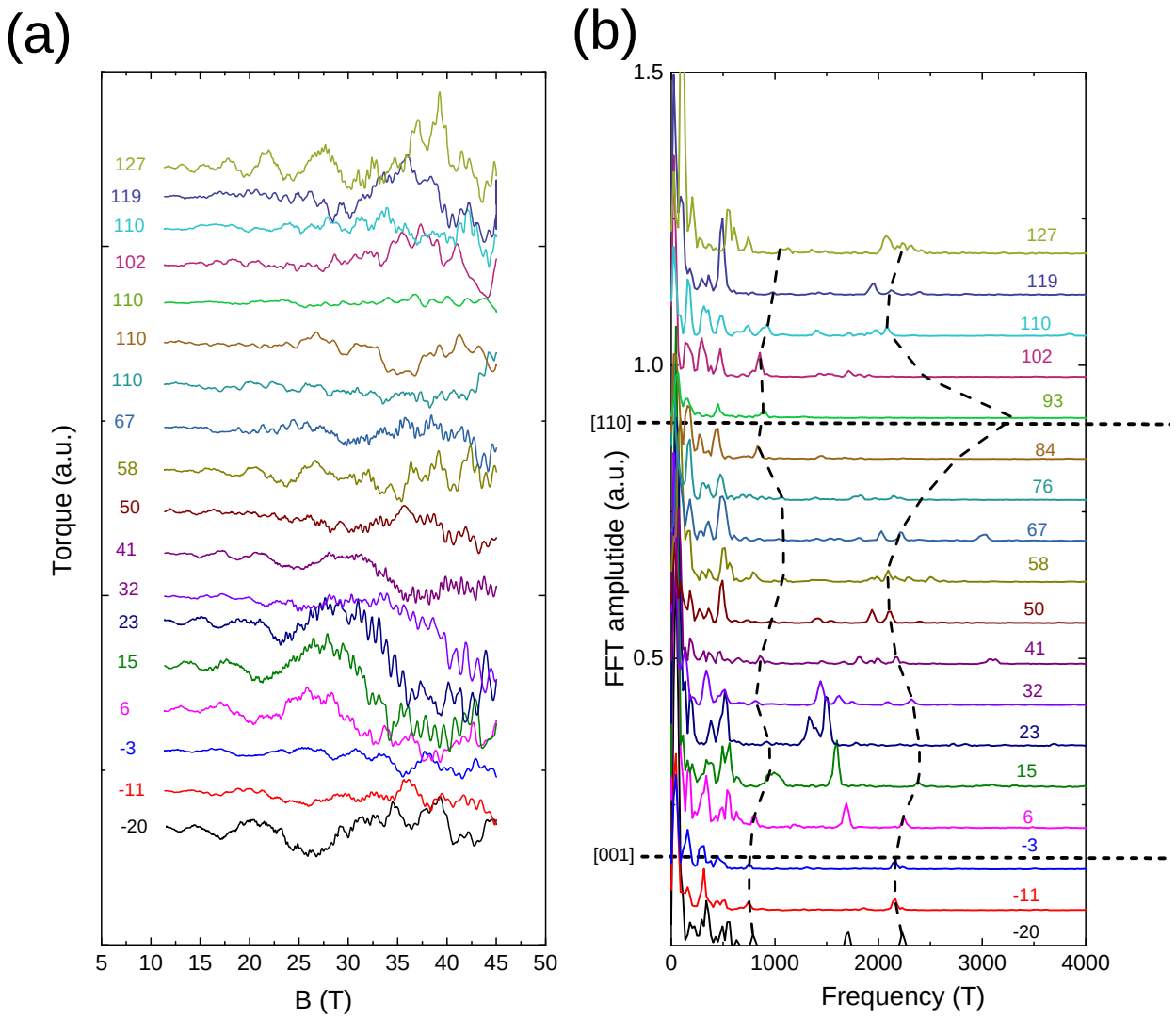

Figure B.5: **High field torque and FFT plots.** (a) Torque curves. (b) FFT plots. The used data range is between 35 T and 65 T. The magnetic field was applied within the $(1\bar{1}0)$ plane.

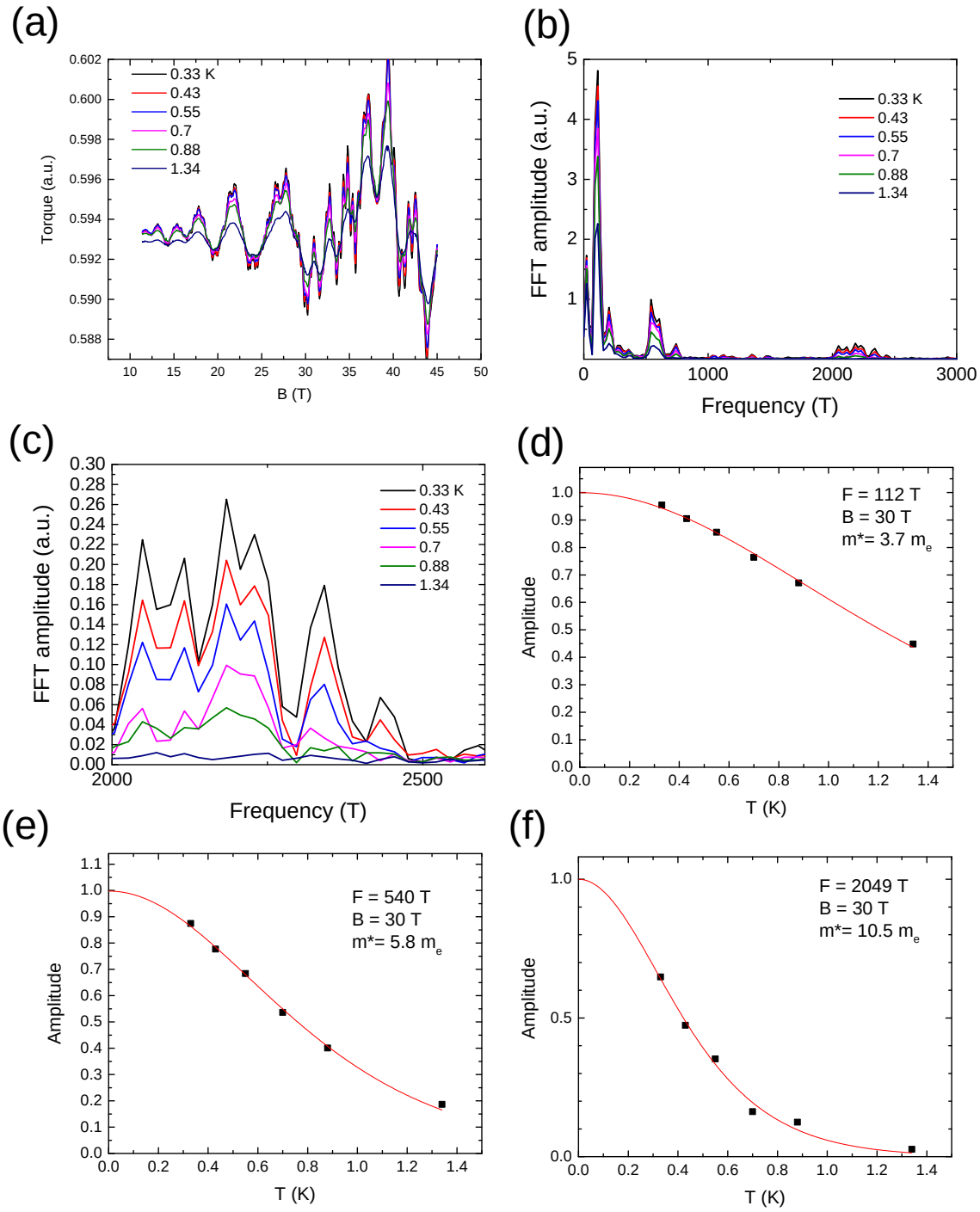

Figure B.6: **Tempeature dependence of quantum oscillation amplitude.** (a) Torque curves. (b) FFT plot. (c) Expanded between 2 kT and 2.6 kT. (d)(e)(f) Temperature dependence of FFT amplitude. The red lines are the fitting curves of LK formula.

sometimes the dHvA oscillations arise from the impurity phase of the sample. Thus, it is important to observe the SdH oscillations to confirm that the oscillations originate from the target sample, since the SdH effect is not sensitive to the impurity phase.

To observe the SdH oscillations, we used PDO technique [157] in the pulse fields in National High Magnetic Field Lab, Los Alamos. The pulse magnetic fields of up to 65 T were applied. Since $Cd_2Re_2O_7$ is metallic and its resistivity is small, it is difficult to directly measure the resistivity of the sample by standard 4-wire measurement. Instead, PDO can be used to measure the relative change of conductivity of the sample. Thus, the quantum oscillations observed by PDO originate from the SdH effect.

Firstly, we show the validity of our data taken in the pulse fields. Fig. B.7 shows the two PDO data taken at almost the same condition at T = 0.77 K (black) and T = 0.78 K (red). They reasonably overlap to each other. Moreover, the FFT plot in Fig. B.7 (b) shows that the signal is reproducible, hence these oscillation peaks are intrinsic. Furthermore, two peaks observed around 2.4 kT are consistent with the spin-split Fermi surface.

The temperature dependence of FFT data is shown in Fig. B.8. The gradually vanishing peaks confirm that the peaks are intrinsic and not noise.

The angular dependence of FFT data taken by PDO is shown in Fig. B.9. In this measurement, due to the sample space limitation, the magnetic field was applied within the $(11\bar{2})$ plane. This result confirms that all the branches around 500 T, 1.5 kT and 2.5 kT are intrinsic.

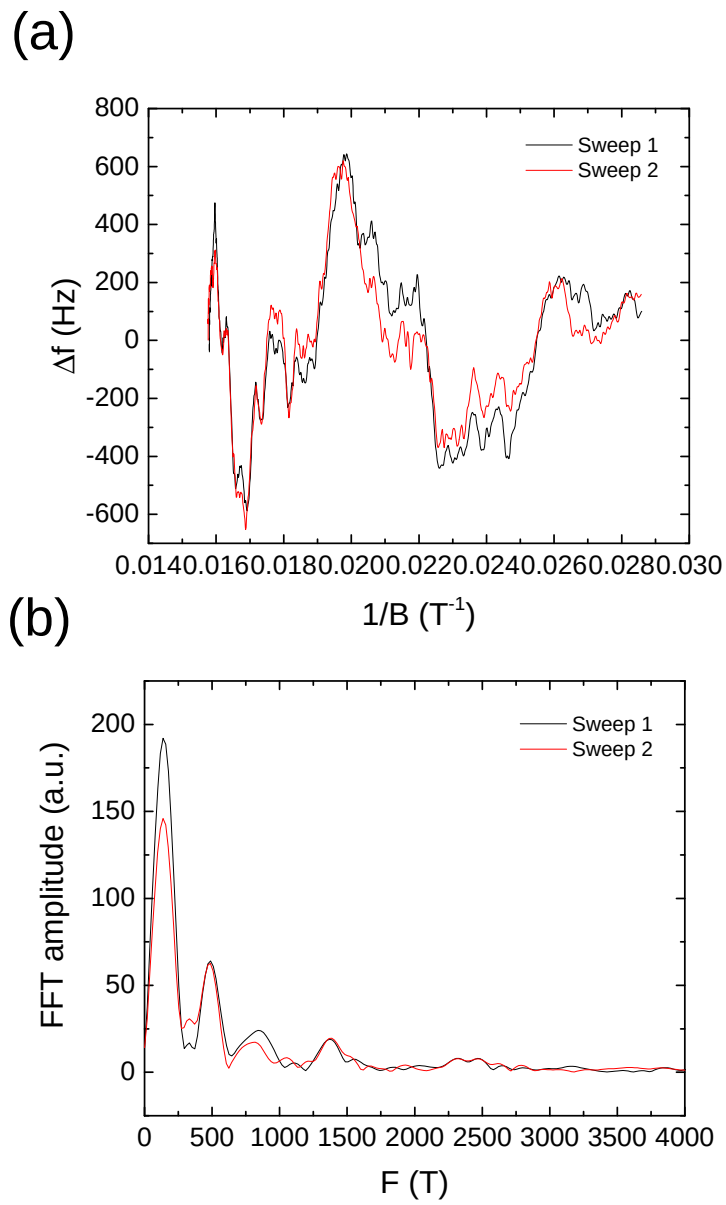

Figure B.7: **Reproducible PDO signals in pulse magnetic fields.** (a) PDO signals vs magnetic fields after background subtraction. (c) FFT plot.

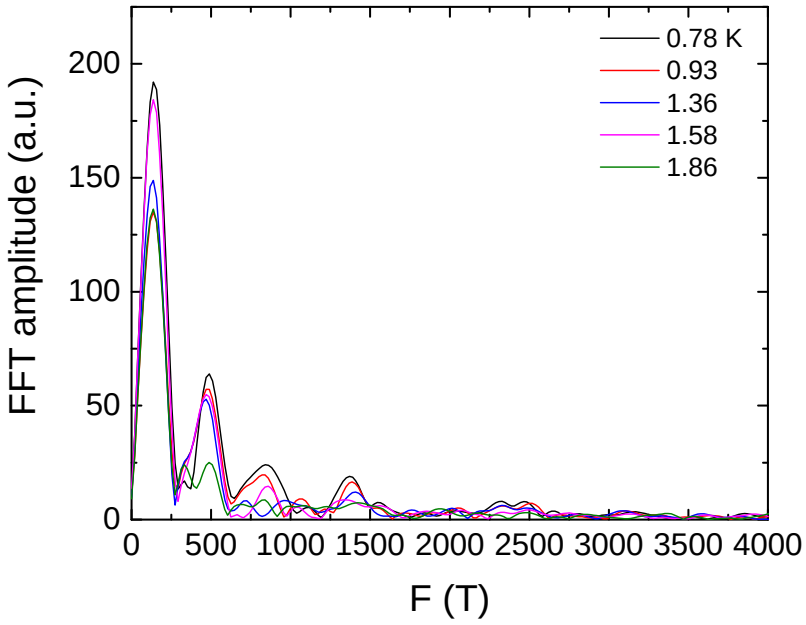

Figure B.8: **Temperature dependence of FFT data.**

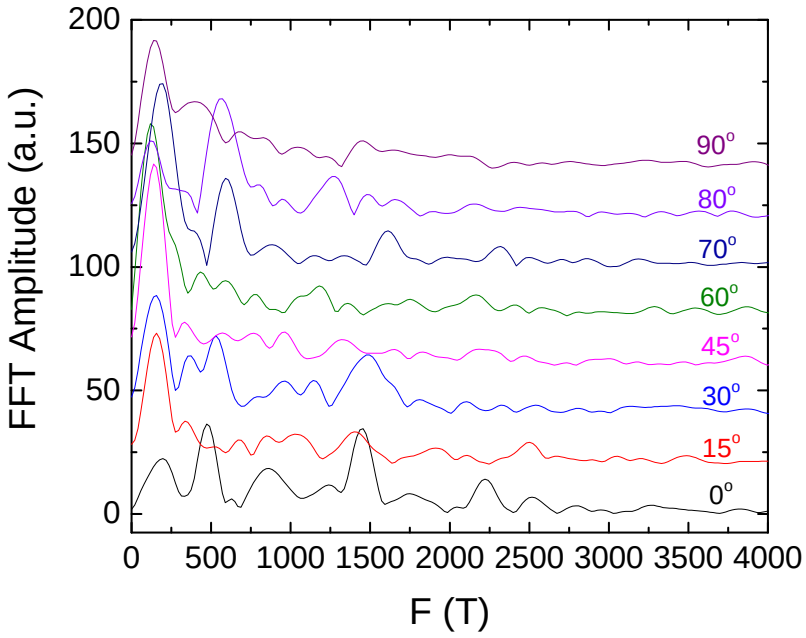

Figure B.9: **Angular dependence of FFT data.**

BIBLIOGRAPHY

BIBLIOGRAPHY

[1] David J Thouless, Mahito Kohmoto, M Peter Nightingale, and Md den Nijs. Quantized Hall conductance in a two-dimensional periodic potential. *Physical Review Letters*, 49(6):405, 1982.

[2] Grigory E Volovik. *The universe in a helium droplet*, volume 117. Oxford University Press on Demand, 2003.

[3] Charles L Kane and Eugene J Mele. Quantum spin Hall effect in graphene. *Physical review letters*, 95(22):226801, 2005.

[4] Joel E Moore and Leon Balents. Topological invariants of time-reversal-invariant band structures. *Physical Review B*, 75(12):121306, 2007.

[5] Liang Fu, Charles L Kane, and Eugene J Mele. Topological insulators in three dimensions. *Physical review letters*, 98(10):106803, 2007.

[6] YL Chen, James G Analytis, J-H Chu, ZK Liu, S-K Mo, Xiao-Liang Qi, HJ Zhang, DH Lu, Xi Dai, Zhong Fang, et al. Experimental realization of a three-dimensional topological insulator, Bi_2Te_3. *science*, 325(5937):178–181, 2009.

[7] Markus König, Steffen Wiedmann, Christoph Brüne, Andreas Roth, Hartmut Buhmann, Laurens W Molenkamp, Xiao-Liang Qi, and Shou-Cheng Zhang. Quantum spin Hall insulator state in HgTe quantum wells. *Science*, 318(5851):766–770, 2007.

[8] Ivan Knez, Rui-Rui Du, and Gerard Sullivan. Evidence for helical edge modes in inverted InAs/GaSb quantum wells. *Physical review letters*, 107(13):136603, 2011.

[9] David Hsieh, Dong Qian, Lewis Wray, YuQi Xia, Yew San Hor, Robert Joseph Cava, and M Zahid Hasan. A topological Dirac insulator in a quantum spin Hall phase. *Nature*, 452(7190):970, 2008.

[10] SHUN-QING. SHEN. *TOPOLOGICAL INSULATORS: Dirac Equation in Condensed Matter*. SPRINGER, 2017.

[11] Michael Tinkham. *Introduction to superconductivity*. Courier Corporation, 1996.

[12] A Yu Kitaev. Unpaired Majorana fermions in quantum wires. *Physics-Uspekhi*, 44(10S):131, 2001.

[13] Liang Fu and Erez Berg. Odd-parity topological superconductors: theory and application to $Cu_xBi_2Se_3$. *Physical review letters*, 105(9):097001, 2010.

[14] Y Maeno, H Hashimoto, K Yoshida, S Nishizaki, T Fujita, JG Bednorz, and F Lichtenberg. Superconductivity in a layered perovskite without copper. *Nature*, 372(6506):532, 1994.

[15] K Ishida, H Mukuda, Y Kitaoka, K Asayama, ZQ Mao, Y Mori, and Y Maeno. Spin-triplet superconductivity in Sr_2RuO_4 identified by ^{17}O Knight shift. *Nature*, 396(6712):658, 1998.

[16] G Ml Luke, Y Fudamoto, KM Kojima, MI Larkin, J Merrin, B Nachumi, YJ Uemura, Y Maeno, ZQ Mao, Y Mori, et al. Time-reversal symmetry-breaking superconductivity in Sr)2RuO_4. *Nature*, 394(6693):558, 1998.

[17] GR Stewart, Z Fisk, JO Willis, and JL Smith. Possibility of Coexistence of Bulk Superconductivity and Spin Fluctuations in UPt_3. *Physical review letters*, 52(8):679, 1984.

[18] Youichi Yanase. Nonsymmorphic Weyl superconductivity in UPt_3 based on E_{2u} representation. *Physical Review B*, 94(17):174502, 2016.

[19] SHINGO YONEZAWA. Bulk Topological Superconductors. *AAPPS Bulletin*, 26(3), 2016.

[20] Masatoshi Sato and Yoichi Ando. Topological superconductors: a review. *Reports on Progress in Physics*, 80(7):076501, 2017.

[21] Mikito Koshino and Intan Fatimah Hizbullah. Magnetic susceptibility in three-dimensional nodal semimetals. *Physical Review B*, 93(4):045201, 2016.

[22] AA Burkov, MD Hook, and Leon Balents. Topological nodal semimetals. *Physical Review B*, 84(23):235126, 2011.

[23] T Sato, Kouji Segawa, K Kosaka, S Souma, K Nakayama, K Eto, T Minami, Yoichi Ando, and T Takahashi. Unexpected mass acquisition of Dirac fermions at the quantum phase transition of a topological insulator. *Nature Physics*, 7(11):840, 2011.

[24] Su-Yang Xu, Y Xia, LA Wray, S Jia, F Meier, JH Dil, J Osterwalder, B Slomski, A Bansil, H Lin, et al. Topological phase transition and texture inversion in a tunable topological insulator. *Science*, 332(6029):560–564, 2011.

[25] Matthew Brahlek, Namrata Bansal, Nikesh Koirala, Su-Yang Xu, Madhab Neupane, Chang Liu, M Zahid Hasan, and Seongshik Oh. Topological-metal to band-insulator transition in $(Bi_{1-x}In_x)_2Se_3$ thin films. *Physical review letters*, 109(18):186403, 2012.

[26] Zhijun Wang, Yan Sun, Xing-Qiu Chen, Cesare Franchini, Gang Xu, Hongming Weng, Xi Dai, and Zhong Fang. Dirac semimetal and topological phase transitions in A_3Bi (A= Na, K, Rb). *Physical Review B*, 85(19):195320, 2012.

[27] Zhijun Wang, Hongming Weng, Quansheng Wu, Xi Dai, and Zhong Fang. Three-dimensional Dirac semimetal and quantum transport in Cd_3As_2. *Physical Review B*, 88(12):125427, 2013.

[28] ZK Liu, Bo Zhou, Yong Zhang, ZJ Wang, HM Weng, Dharmalingam Prabhakaran, S-K Mo, ZX Shen, Zhong Fang, Xi Dai, et al. Discovery of a three-dimensional topological Dirac semimetal, Na_3Bi. *Science*, 343(6173):864–867, 2014.

[29] ZK Liu, Juan Jiang, Bo Zhou, ZJ Wang, Yi Zhang, HM Weng, Dharmalingam Prabhakaran, Sung Kwan Mo, Han Peng, Pavel Dudin, et al. A stable three-dimensional topological Dirac semimetal Cd_3As_2. *Nature materials*, 13(7):677, 2014.

[30] NP Armitage, EJ Mele, and Ashvin Vishwanath. Weyl and Dirac semimetals in three-dimensional solids. *Reviews of Modern Physics*, 90(1):015001, 2018.

[31] Hermann Weyl. Gravitation and the electron. *Proceedings of the National Academy of Sciences*, 15(4):323–334, 1929.

[32] Hongming Weng, Chen Fang, Zhong Fang, B Andrei Bernevig, and Xi Dai. Weyl semimetal phase in noncentrosymmetric transition-metal monophosphides. *Physical Review X*, 5(1):011029, 2015.

[33] Shin-Ming Huang, Su-Yang Xu, Ilya Belopolski, Chi-Cheng Lee, Guoqing Chang, BaoKai Wang, Nasser Alidoust, Guang Bian, Madhab Neupane, Chenglong Zhang, et al. A Weyl Fermion semimetal with surface Fermi arcs in the transition metal monopnictide TaAs class. *Nature communications*, 6:7373, 2015.

[34] BQ Lv, HM Weng, BB Fu, XP Wang, Hu Miao, Junzhang Ma, P Richard, XC Huang, LX Zhao, GF Chen, et al. Experimental discovery of Weyl semimetal TaAs. *Physical Review X*, 5(3):031013, 2015.

[35] Su-Yang Xu, Nasser Alidoust, Ilya Belopolski, Zhujun Yuan, Guang Bian, Tay-Rong Chang, Hao Zheng, Vladimir N Strocov, Daniel S Sanchez, Guoqing Chang, et al. Discovery of a Weyl fermion state with Fermi arcs in niobium arsenide. *Nature Physics*, 11(9):748, 2015.

[36] N Xu, HM Weng, BQ Lv, Christian E Matt, J Park, Federico Bisti, Vladimir N Strocov, D Gawryluk, E Pomjakushina, Kazimierz Conder, et al. Observation of Weyl nodes and Fermi arcs in tantalum phosphide. *Nature communications*, 7:11006, 2016.

[37] Xiangang Wan, Ari M Turner, Ashvin Vishwanath, and Sergey Y Savrasov. Topological semimetal and Fermi-arc surface states in the electronic structure of pyrochlore iridates. *Physical Review B*, 83(20):205101, 2011.

[38] Max Hirschberger, Satya Kushwaha, Zhijun Wang, Quinn Gibson, Sihang Liang, Carina A Belvin, BA Bernevig, RJ Cava, and NP Ong. The chiral anomaly and thermopower of Weyl fermions in the half-Heusler GdPtBi. *Nature materials*, 15(11):1161, 2016.

[39] Satoru Nakatsuji, Naoki Kiyohara, and Tomoya Higo. Large anomalous Hall effect in a non-collinear antiferromagnet at room temperature. *Nature*, 527(7577):212, 2015.

[40] Naoki Kiyohara, Takahiro Tomita, and Satoru Nakatsuji. Giant anomalous Hall effect in the chiral antiferromagnet Mn_3Ge. *Physical Review Applied*, 5(6):064009, 2016.

[41] Yew San Hor, Anthony J Williams, Joseph G Checkelsky, Pedram Roushan, Jungpil Seo, Qiang Xu, Henny W Zandbergen, A Yazdani, NP Ong, and Robert Joseph Cava. Superconductivity in $Cu_xBi_2Se_3$ and its implications for pairing in the undoped topological insulator. *Physical review letters*, 104(5):057001, 2010.

[42] L Andrew Wray, Su-Yang Xu, Yuqi Xia, Yew San Hor, Dong Qian, Alexei V Fedorov, Hsin Lin, Arun Bansil, Robert J Cava, and M Zahid Hasan. Observation of topological order in a superconducting doped topological insulator. *Nature Physics*, 6(11):855, 2010.

[43] M Kriener, Kouji Segawa, Zhi Ren, Satoshi Sasaki, Shohei Wada, Susumu Kuwabata, and Yoichi Ando. Electrochemical synthesis and superconducting phase diagram of $Cu_xBi_2Se_3$. *Physical Review B*, 84(5):054513, 2011.

[44] JA Schneeloch, RD Zhong, ZJ Xu, GD Gu, and JM Tranquada. Dependence of superconductivity in $Cu_xBi_2Se_3$ on quenching conditions. *Physical Review B*, 91(14):144506, 2015.

[45] Meng Wang, Yanru Song, Lixing You, Zhuojun Li, Bo Gao, Xiaoming Xie, and Mianheng Jiang. A combined method for synthesis of superconducting Cu doped Bi_2Se_3. *Scientific reports*, 6:22713, 2016.

[46] TV Bay, T Naka, YK Huang, H Luigjes, MS Golden, and A De Visser. Superconductivity in the doped topological insulator $Cu_xBi_2Se_3$ under high pressure. *Physical review letters*, 108(5):057001, 2012.

[47] Kazumi Maki. Effect of Pauli paramagnetism on magnetic properties of high-field superconductors. *Physical Review*, 148(1):362, 1966.

[48] Ben J Lawson, Yew San Hor, and Lu Li. Quantum oscillations in the topological superconductor candidate $Cu_{0.25}Bi_2Se_3$. *Physical review letters*, 109(22):226406, 2012.

[49] E Lahoud, E Maniv, M Shaviv Petrushevsky, M Naamneh, A Ribak, S Wiedmann, L Petaccia, Z Salman, KB Chashka, Y Dagan, et al. Evolution of the Fermi surface of a doped topological insulator with carrier concentration. *Physical Review B*, 88(19):195107, 2013.

[50] Benjamin J Lawson, Gang Li, Fan Yu, Tomoya Asaba, Colin Tinsman, T Gao, W Wang, Yew San Hor, and Lu Li. Quantum oscillations in $Cu_xBi_2Se_3$ in high magnetic fields. *Physical Review B*, 90(19):195141, 2014.

[51] Satoshi Sasaki, M Kriener, Kouji Segawa, Keiji Yada, Yukio Tanaka, Masatoshi Sato, and Yoichi Ando. Topological superconductivity in $Cu_xBi_2Se_3$. *Physical review letters*, 107(21):217001, 2011.

[52] Timothy H Hsieh and Liang Fu. Majorana fermions and exotic surface Andreev bound states in topological superconductors: application to $Cu_xBi_2Se_3$. *Physical review letters*, 108(10):107005, 2012.

[53] Ai Yamakage, Keiji Yada, Masatoshi Sato, and Yukio Tanaka. Theory of tunneling conductance and surface-state transition in superconducting topological insulators. *Physical Review B*, 85(18):180509, 2012.

[54] Niv Levy, Tong Zhang, Jeonghoon Ha, Fred Sharifi, A Alec Talin, Young Kuk, and Joseph A Stroscio. Experimental evidence for s-wave pairing symmetry in superconducting $Cu_xBi_2Se_3$ single crystals using a scanning tunneling microscope. *Physical review letters*, 110(11):117001, 2013.

[55] Ran Tao, Ya-Jun Yan, Xi Liu, Zhi-Wei Wang, Yoichi Ando, Tong Zhang, and Dong-Lai Feng. Direct visualization of the nematic superconductivity in $Cu_xBi_2Se_3$. *arXiv preprint arXiv:1804.09122*, 2018.

[56] Jin-Peng Xu, Mei-Xiao Wang, Zhi Long Liu, Jian-Feng Ge, Xiaojun Yang, Canhua Liu, Zhu An Xu, Dandan Guan, Chun Lei Gao, Dong Qian, et al. Experimental detection of a Majorana mode in the core of a magnetic vortex inside a topological insulator-superconductor $Bi_2Te_3/NbSe_2$ heterostructure. *Physical review letters*, 114(1):017001, 2015.

[57] Cihan Kurter, Aaron Finck, Erik Huemiller, Julia Medvedeva, Adam Weis, Juan Atkinson, Yunsheng Qiu, Li Shen, Seng Huat Lee, Thomas Vojta, et al. Andreev Reflection Spectroscopy of Topological Superconductor Candidate Nb _x Bi _2 Se _3. *arXiv preprint arXiv:1707.08516*, 2017.

[58] K Matano, M Kriener, K Segawa, Y Ando, and Guo-qing Zheng. Spin-rotation symmetry breaking in the superconducting state of $Cu_xBi_2Se_3$. *Nature Physics*, 12(9):852, 2016.

[59] Shingo Yonezawa, Kengo Tajiri, Suguru Nakata, Yuki Nagai, Zhiwei Wang, Kouji Segawa, Yoichi Ando, and Yoshiteru Maeno. Thermodynamic evidence for nematic superconductivity in $Cu_xBi_2Se_3$. *Nature Physics*, 13(2):123, 2017.

[60] Liang Fu. Odd-parity topological superconductor with nematic order: Application to $Cu_xBi_2Se_3$. *Physical Review B*, 90(10):100509, 2014.

[61] Zhongheng Liu, Xiong Yao, Jifeng Shao, Ming Zuo, Li Pi, Shun Tan, Changjin Zhang, and Yuheng Zhang. Superconductivity with Topological Surface State in $Sr_xBi_2Se_3$. *Journal of the American Chemical Society*, 137(33):10512–10515, 2015.

[62] H Leng, D Cherian, YK Huang, J-C Orain, A Amato, and A de Visser. Muon spin rotation study of the topological superconductor $Sr_xBi_2Se_3$. *Physical Review B*, 97(5):054503, 2018.

[63] VK Maurya, Prakriti Neha, Pankaj Srivastava, Satyabrata Patnaik, et al. Superconductivity by Sr intercalation in the layered topological insulator Bi_2Se_3. *Physical Review B*, 92(2):020506, 2015.

[64] CQ Han, H Li, WJ Chen, Fengfeng Zhu, Meng-Yu Yao, ZJ Li, M Wang, Bo F Gao, DD Guan, Canhua Liu, et al. Electronic structure of a superconducting topological insulator Sr-doped Bi_2Se_3. *Applied Physics Letters*, 107(17):171602, 2015.

[65] Madhab Neupane, Yukiaki Ishida, Raman Sankar, Jian-Xin Zhu, Daniel S Sanchez, Ilya Belopolski, Su-Yang Xu, Nasser Alidoust, M Mofazzel Hosen, Shik Shin, et al. Electronic structure and relaxation dynamics in a superconducting topological material. *Scientific reports*, 6:22557, 2016.

[66] Y Pan, AM Nikitin, GK Araizi, YK Huang, Y Matsushita, T Naka, and A De Visser. Rotational symmetry breaking in the topological superconductor $Sr_xBi_2Se_3$ probed by upper-critical field experiments. *Scientific reports*, 6:28632, 2016.

[67] Guan Du, YuFeng Li, John Schneeloch, RD Zhong, GenDa Gu, Huan Yang, Hai Lin, and Hai-Hu Wen. Superconductivity with two-fold symmetry in topological superconductor $Sr_xBi_2Se_3$. *Science China Physics, Mechanics & Astronomy*, 60(3):037411, 2017.

[68] AM Nikitin, Y Pan, YK Huang, T Naka, and A de Visser. High-pressure study of the basal-plane anisotropy of the upper critical field of the topological superconductor $Sr_xBi_2Se_3$. *Physical Review B*, 94(14):144516, 2016.

[69] Yonghui Zhou, Xuliang Chen, Ranran Zhang, Jifeng Shao, Xuefei Wang, Chao An, Ying Zhou, Changyong Park, Wei Tong, Li Pi, et al. Pressure-induced reemergence of superconductivity in topological insulator $Sr_{0.065}Bi_2Se_3$. *Physical Review B*, 93(14):144514, 2016.

[70] K Manikandan, P Neha, G Kalai Selvan, B Wang, Y Uwatoko, K Ishigaki, R Jha, VPS Awana, S Arumugam, S Patnaik, et al. Possibility for conventional superconductivity in $Sr_{0.1}Bi_2Se_3$ from high-pressure transport studies. *EPL (Europhysics Letters)*, 118(4):47008, 2017.

[71] Guan Du, Jifeng Shao, Xiong Yang, Zengyi Du, Delong Fang, Jinghui Wang, Kejing Ran, Jinsheng Wen, Changjin Zhang, Huan Yang, et al. Drive the Dirac electrons into cooper pairs in $Sr_xBi_2Se_3$. *Nature communications*, 8:14466, 2017.

[72] Meng Wang, Dejiong Zhang, Wenxiang Jiang, Zhuojun Li, Chaoqun Han, Jinfeng Jia, Jixue Li, Shan Qiao, Dong Qian, He Tian, et al. Growth and structural characterisation of Sr-doped Bi_2Se_3 thin films. *Scientific reports*, 8(1):2192, 2018.

[73] Yunsheng Qiu, Kyle Nocona Sanders, Jixia Dai, Julia E Medvedeva, Weida Wu, Pouyan Ghaemi, Thomas Vojta, and Yew San Hor. Time reversal symmetry breaking superconductivity in topological materials. *arXiv preprint arXiv:1512.03519*, 2015.

[74] Junying Shen, Wen-Yu He, Noah Fan Qi Yuan, Zengle Huang, Chang-woo Cho, Seng Huat Lee, Yew San Hor, Kam Tuen Law, and Rolf Lortz. Nematic topological superconducting phase in Nb-doped Bi_2Se_3. *npj Quantum Materials*, 2(1):59, 2017.

[75] BJ Lawson, Paul Corbae, Gang Li, Fan Yu, Tomoya Asaba, Colin Tinsman, Y Qiu, Julia E Medvedeva, Yew San Hor, and Lu Li. Multiple Fermi surfaces in superconducting Nb-doped Bi_2Se_3. *Physical Review B*, 94(4):041114, 2016.

[76] Tomoya Asaba, BJ Lawson, Colin Tinsman, Lu Chen, Paul Corbae, Gang Li, Yunsheng Qiu, Yew San Hor, Liang Fu, and Lu Li. Rotational Symmetry Breaking in a Trigonal Superconductor Nb-doped Bi_2Se_3. *Physical Review X*, 7(1):011009, 2017.

[77] Jörn WF Venderbos, Vladyslav Kozii, and Liang Fu. Identification of nematic superconductivity from the upper critical field. *Physical Review B*, 94(9):094522, 2016.

[78] MP Smylie, Helmut Claus, U Welp, W-K Kwok, Y Qiu, Yew San Hor, and A Snezhko. Evidence of nodes in the order parameter of the superconducting doped topological insulator nb x bi 2 se 3 via penetration depth measurements. *Physical Review B*, 94(18):180510, 2016.

[79] S Kasahara, HJ Shi, K Hashimoto, S Tonegawa, Y Mizukami, T Shibauchi, K Sugimoto, T Fukuda, T Terashima, Andriy H Nevidomskyy, et al. Electronic nematicity above the structural and superconducting transition in $BaFe_2(As_{1-x}P_x)_2$. *Nature*, 486(7403):382, 2012.

[80] R Okazaki, T Shibauchi, HJ Shi, Y Haga, TD Matsuda, E Yamamoto, Y Onuki, H Ikeda, and Y Matsuda. Rotational symmetry breaking in the hidden-order phase of URu_2Si_2. *Science*, 331(6016):439–442, 2011.

[81] JM Lu, O Zheliuk, I Leermakers, NFQ Yuan, U Zeitler, KT Law, and JT Ye. Evidence for two-dimensional Ising superconductivity in gated MoS_2. *Science*, 350(6266):1353–1357, 2015.

[82] Yu Saito, Yasuharu Nakamura, Mohammad Saeed Bahramy, Yoshimitsu Kohama, Jianting Ye, Yuichi Kasahara, Yuji Nakagawa, Masaru Onga, Masashi Tokunaga, Tsutomu Nojima, Youichi Yanase, and Yoshihiro Iwasa. Superconductivity protected by spin-valley locking in ion-gated MoS_2. *Nat Phys*, 12(2):144–149, Feb 2016. Letter.

[83] Xiaoxiang Xi, Zefang Wang, Weiwei Zhao, Ju-Hyun Park, Kam Tuen Law, Helmuth Berger, László Forró, Jie Shan, and Kin Fai Mak. Ising pairing in superconducting $NbSe_2$ atomic layers. *Nature Physics*, 12(2):139–143, 2016.

[84] Xiaoxiang Xi, Liang Zhao, Zefang Wang, Helmuth Berger, László Forró, Jie Shan, and Kin Fai Mak. Strongly enhanced charge-density-wave order in monolayer $NbSe_2$. *Nat Nano*, 10(9):765–769, Sep 2015. Letter.

[85] Miguel M Ugeda, Aaron J Bradley, Yi Zhang, Seita Onishi, Yi Chen, Wei Ruan, Claudia Ojeda-Aristizabal, Hyejin Ryu, Mark T Edmonds, Hsin-Zon Tsai, Alexander Riss, Sung-Kwan Mo, Dunghai Lee, Alex Zettl, Zahid Hussain, Zhi-Xun SHen, and Michael F. Crommie. Characterization of collective ground states in single-layer $NbSe_2$. *Nature Physics*, 12(1):92–97, 2016.

[86] A. W. Tsen, B. Hunt, Y. D. Kim, Z. J. Yuan, S. Jia, R. J. Cava, J. Hone, P. Kim, C. R. Dean, and A. N. Pasupathy. Nature of the quantum metal in a two-dimensional crystalline superconductor. *Nat Phys*, 12(3):208–212, Mar 2016. Letter.

[87] Alexey A Soluyanov, Dominik Gresch, Zhijun Wang, QuanSheng Wu, Matthias Troyer, Xi Dai, and B Andrei Bernevig. Type-II Weyl semimetals. *Nature*, 527(7579):495–498, 2015.

[88] Ilya Belopolski, Su-Yang Xu, Yukiaki Ishida, Xingchen Pan, Peng Yu, Daniel S. Sanchez, Hao Zheng, Madhab Neupane, Nasser Alidoust, Guoqing Chang, Tay-Rong Chang, Yun Wu, Guang Bian, Shin-Ming Huang, Chi-Cheng Lee, Daixiang Mou, Lunan Huang, You Song, Baigeng Wang, Guanghou Wang, Yao-Wen Yeh, Nan Yao, Julien E. Rault, Patrick Le Fèvre, Fran çois Bertran, Horng-Tay Jeng, Takeshi Kondo, Adam Kaminski, Hsin Lin, Zheng Liu, Fengqi Song, Shik Shin, and M. Zahid Hasan. Fermi arc electronic structure and Chern numbers in the type-II Weyl semimetal candidate $Mo_xW_{1-x}Te_2$. *Phys. Rev. B*, 94:085127, Aug 2016.

[89] Yun Wu, Daixiang Mou, Na Hyun Jo, Kewei Sun, Lunan Huang, S. L. Bud'ko, P. C. Canfield, and Adam Kaminski. Observation of Fermi arcs in the type-II Weyl semimetal candidate WTe_2. *Phys. Rev. B*, 94:121113, Sep 2016.

[90] Chenlu Wang, Yan Zhang, Jianwei Huang, Simin Nie, Guodong Liu, Aiji Liang, Yuxiao Zhang, Bing Shen, Jing Liu, Cheng Hu, Ying Ding, Defa Liu, Yong Hu, Shaolong He, Lin Zhao, Li Yu, Jin Hu, Jiang Wei, Zhiqiang Mao, Youguo Shi, Xiaowen Jia, Fengfeng Zhang, Shenjin Zhang, Feng Yang, Zhimin Wang, Qinjun Peng, Hongming Weng, Xi Dai, Zhong Fang, Zuyan Xu, Chuangtian Chen, and X. J. Zhou. Observation of Fermi arc and its connection with bulk states in the candidate type-II Weyl semimetal WTe_2. *Phys. Rev. B*, 94:241119, Dec 2016.

[91] Aiji Liang, Jianwei Huang, Simin Nie, Ying Ding, Qiang Gao, Cheng Hu, Shaolong He, Yuxiao Zhang, Chenlu Wang, Bing Shen, Jing Liu, Ping Ai, Li Yu, Xuan Sun, Wenjuan Zhao, Shoupeng Lv, Defa Liu, Cong Li, Yan Zhang, Yong Hu, Yu Xu, Lin Zhao, Guodong Liu, Zhiqiang Mao, Xiaowen Jia, Fengfeng Zhang, Shenjin Zhang, Feng Yang, Zhimin Wang, Qinjun Peng, Hongming Weng, Xi Dai, Zhong Fang, Zuyan Xu, Chuangtian Chen, and X. J. Zhou. Electronic Evidence for Type II Weyl Semimetal State in $MoTe_2$. *arXiv preprint arXiv:1604.01706*, 2016.

[92] J. Jiang, Z. K. Liu, Y. Sun, H. F. Yang, C. R. Rajamathi, Y. P. Qi, L. X. Yang, C. Chen, H. Peng, C.-C. Hwang, S. Z. Sun, S.-K. Mo, I. Vobornik, J. Fujii, S. S. P. Parkin, C. Felser, B. H. Yan, and Y. L. Chen. Signature of type-II Weyl semimetal phase in $MoTe_2$. *Nature Communications*, 8:13973 EP –, Jan 2017. Article.

[93] Ke Deng, Guoliang Wan, Peng Deng, Kenan Zhang, Shijie Ding, Eryin Wang, Mingzhe Yan, Huaqing Huang, Hongyun Zhang, Zhilin Xu, Jonathan Denlinger, Alexei Fedorov, Haitao Yang, Wenhui Duan, Hong Yao, Yang Wu, Shoushan Fan, Haijun Zhang, Xi Chen, and Shuyun Zhou. Experimental observation of topological Fermi arcs in type-II Weyl semimetal MoTe2. *Nat Phys*, 12(12):1105–1110, Dec 2016. Letter.

[94] Lunan Huang, Timothy M. McCormick, Masayuki Ochi, Zhiying Zhao, Michi-To Suzuki, Ryotaro Arita, Yun Wu, Daixiang Mou, Huibo Cao, Jiaqiang Yan, Nandini Trivedi, and Adam Kaminski. Spectroscopic evidence for a type II Weyl semimetallic state in $MoTe_2$. *Nat Mater*, 15(11):1155–1160, Nov 2016. Letter.

[95] Mazhar N. Ali, Jun Xiong, Steven Flynn, Jing Tao, Quinn D. Gibson, Leslie M. Schoop, Tian Liang, Neel Haldolaarachchige, Max Hirschberger, N. P. Ong, and R. J. Cava. Large, non-saturating magnetoresistance in WTe_2. *Nature*, 514(7521):205–208, 10 2014.

[96] Xing-Chen Pan, Xuliang Chen, Huimei Liu, Yanqing Feng, Zhongxia Wei, Yonghui Zhou, Zhenhua Chi, Li Pi, Fei Yen, Fengqi Song, Xiangang Wan,

Zhaorong Yang, Baigeng Wang, Guanghou Wang, and Yuheng Zhang. Pressure-driven dome-shaped superconductivity and electronic structural evolution in tungsten ditelluride. *Nature communications*, 6, 2015.

[97] Defen Kang, Yazhou Zhou, Wei Yi, Chongli Yang, Jing Guo, Youguo Shi, Shan Zhang, Zhe Wang, Chao Zhang, Sheng Jiang, Aiguo Li, Ke Yang, Qi Wu, Guangming Zhang, Liling Sun, and Zhongxian Zhao. Superconductivity emerging from a suppressed large magnetoresistant state in tungsten ditelluride. *Nature communications*, 6, 2015.

[98] Pengchao Lu, Joon-Seok Kim, Jing Yang, Hao Gao, Juefei Wu, Dexi Shao, Bin Li, Dawei Zhou, Jian Sun, Deji Akinwande, et al. Origin of superconductivity in the Weyl semimetal WTe_2 under pressure. *Physical Review B*, 94(22):224512, 2016.

[99] Yanpeng Qi, Pavel G. Naumov, Mazhar N. Ali, Catherine R. Rajamathi, Walter Schnelle, Oleg Barkalov, Michael Hanfland, Shu-Chun Wu, Chandra Shekhar, Yan Sun, Vicky Süß, Marcus Schmidt, Ulrich Schwarz, Eckhard Pippel, Peter Werner, Reinald Hillebrand, Tobias Förster, Erik Kampert, Stuart Parkin, R. J. Cava, Claudia Felser, Binghai Yan, and Sergey A. Medvedev. Superconductivity in Weyl semimetal candidate $MoTe_2$. *Nature Communications*, 7:11038 EP –, 03 2016.

[100] WL Bond, AS Cooper, K Andres, GW Hull, TH Geballe, and BT Matthias. Superconductivity in films of β tungsten and other transition metals. *Physical Review Letters*, 15(6):260, 1965.

[101] Minhao Liu, Jinsong Zhang, Cui-Zu Chang, Zuocheng Zhang, Xiao Feng, Kang Li, Ke He, Li-li Wang, Xi Chen, Xi Dai, Zhong Fang, Qi-Kun Xue, Xucun Ma, and Yayu Wang. Crossover between weak antilocalization and weak localization in a magnetically doped topological insulator. *Physical review letters*, 108(3):036805, 2012.

[102] Hong-Tao He, Gan Wang, Tao Zhang, Iam-Keong Sou, George KL Wong, Jian-Nong Wang, Hai-Zhou Lu, Shun-Qing Shen, and Fu-Chun Zhang. Impurity effect on weak antilocalization in the topological insulator Bi_2Te_3. *Physical review letters*, 106(16):166805, 2011.

[103] Shinobu Hikami, Anatoly I Larkin, and Yosuke Nagaoka. Spin-orbit interaction and magnetoresistance in the two dimensional random system. *Progress of Theoretical Physics*, 63(2):707–710, 1980.

[104] Lin Wang, Ignacio Gutiérrez-Lezama, Céline Barreteau, Nicolas Ubrig, Enrico Giannini, and Alberto F Morpurgo. Tuning magnetotransport in a compensated semimetal at the atomic scale. *Nature communications*, 6, 2015.

[105] EH Sondheimer and AH Wilson. The theory of the magneto-resistance effects in metals. In *Proceedings of the Royal Society of London A: Mathematical, Physical and Engineering Sciences*, volume 190, pages 435–455. The Royal Society, 1947.

[106] SS Murzin, SI Dorozhkin, G Landwehr, and AC Gossard. Effect of hole-hole scattering on the conductivity of the two-component 2D hole gas in GaAs/(AlGa) As heterostructures. *Journal of Experimental and Theoretical Physics Letters*, 67(2):113–119, 1998.

[107] VL Berezinskii. Destruction of long-range order in one-dimensional and two-dimensional systems having a continuous symmetry group I. classical systems. *Sov. Phys. JETP*, 32(3):493–500, 1971.

[108] John Michael Kosterlitz and David James Thouless. Ordering, metastability and phase transitions in two-dimensional systems. *Journal of Physics C: Solid State Physics*, 6(7):1181, 1973.

[109] MR Beasley, JE Mooij, and TP Orlando. Possibility of vortex-antivortex pair dissociation in two-dimensional superconductors. *Physical Review Letters*, 42(17):1165, 1979.

[110] Kateryna Medvedyeva, Beom Jun Kim, and Petter Minnhagen. Analysis of current-voltage characteristics of two-dimensional superconductors: Finite-size scaling behavior in the vicinity of the Kosterlitz-Thouless transition. *Physical Review B*, 62(21):14531, 2000.

[111] N. Reyren, S. Thiel, A. D. Caviglia, L. Fitting Kourkoutis, G. Hammerl, C. Richter, C. W. Schneider, T. Kopp, A.-S. Rüetschi, D. Jaccard, M. Gabay, D. A. Muller, J.-M. Triscone, and J. Mannhart. Superconducting interfaces between insulating oxides. *Science*, 317(5842):1196–1199, 2007.

[112] Lee A Walsh, Ruoyu Yue, Qingxiao Wang, Adam T Barton, Rafik Addou, Christopher M Smyth, Hui Zhu, Jiyoung Kim, Luigi Colombo, Moon J Kim, Robert M Wallace, and Christopher L Hinkle. WTe_2 thin films grown by beam-interrupted molecular beam epitaxy. *2D Materials*, 4(2):025044, 2017.

[113] Masatoshi Imada, Atsushi Fujimori, and Yoshinori Tokura. Metal-insulator transitions. *Rev. Mod. Phys.*, 70:1039–1263, Oct 1998.

[114] N. P. Armitage, P. Fournier, and R. L. Greene. Progress and perspectives on electron-doped cuprates. *Rev. Mod. Phys.*, 82:2421–2487, Sep 2010.

[115] Di Xiao, Wenguang Zhu, Ying Ran, Naoto Nagaosa, and Satoshi Okamoto. Interface engineering of quantum hall effects in digital transition metal oxide heterostructures. *Nature communications*, 2:596, 2011.

[116] JB Torrance, P Lacorre, AI Nazzal, EJ Ansaldo, and Ch Niedermayer. Systematic study of insulator-metal transitions in perovskites r nio 3 (r= pr, nd, sm, eu) due to closing of charge-transfer gap. *Physical Review B*, 45(14):8209, 1992.

[117] Jiří Chaloupka and Giniyat Khaliullin. Orbital order and possible superconductivity in lanio 3/lamo 3 superlattices. *Physical Review Letters*, 100(1):016404, 2008.

[118] PDC King, HI Wei, YF Nie, M Uchida, C Adamo, S Zhu, X He, I Božović, DG Schlom, and KM Shen. Atomic-scale control of competing electronic phases in ultrathin lanio3. *Nature nanotechnology*, 9(6):443–447, 2014.

[119] Kai-Yu Yang, Wenguang Zhu, Di Xiao, Satoshi Okamoto, Ziqiang Wang, and Ying Ran. Possible interaction-driven topological phases in (111) bilayers of lanio 3. *Physical Review B*, 84(20):201104, 2011.

[120] Andreas Rüegg and Gregory A. Fiete. Topological insulators from complex orbital order in transition-metal oxides heterostructures. *Phys. Rev. B*, 84:201103, Nov 2011.

[121] Andreas Rüegg, Chandrima Mitra, Alexander A. Demkov, and Gregory A. Fiete. Electronic structure of $(\mathrm{lanio}_3)_2/(\mathrm{laalo}_3)_N$ heterostructures grown along [111]. *Phys. Rev. B*, 85:245131, Jun 2012.

[122] Andreas Rüegg, Chandrima Mitra, Alexander A. Demkov, and Gregory A. Fiete. Lattice distortion effects on topological phases in $(\mathrm{lanio}_3)_2/(\mathrm{laalo}_3)_N$ heterostructures grown along the [111] direction. *Phys. Rev. B*, 88:115146, Sep 2013.

[123] David Doennig, Warren E Pickett, and Rossitza Pentcheva. Confinement-driven transitions between topological and mott phases in (la ni o 3) n/(la al o 3) m (111) superlattices. *Physical Review B*, 89(12):121110, 2014.

[124] JL Blok, X Wan, Gertjan Koster, David HA Blank, and G Rijnders. Epitaxial oxide growth on polar (111) surfaces. *Applied physics letters*, 99(15):151917, 2011.

[125] S Middey, D Meyers, M Kareev, EJ Moon, BA Gray, X Liu, JW Freeland, and J Chakhalian. Epitaxial growth of (111)-oriented laalo 3/lanio 3 ultra-thin superlattices. *Applied Physics Letters*, 101(26):261602, 2012.

[126] TH Kim, D Puggioni, Y Yuan, L Xie, H Zhou, N Campbell, PJ Ryan, Y Choi, J-W Kim, JR Patzner, et al. Polar metals by geometric design. *Nature*, 533(7601):68–72, 2016.

[127] Gaoyang Gou, Ilya Grinberg, Andrew M Rappe, and James M Rondinelli. Lattice normal modes and electronic properties of the correlated metal lanio 3. *Physical Review B*, 84(14):144101, 2011.

[128] Marta Gibert, Pavlo Zubko, Raoul Scherwitzl, Jorge Íñiguez, and Jean-Marc Triscone. Exchange bias in lanio3-lamno3 superlattices. *Nature materials*, 11(3):195, 2012.

[129] Alexander J Grutter, Hao Yang, Brian J Kirby, MR Fitzsimmons, Jeffery A Aguiar, Nigel D Browning, CA Jenkins, Elke Arenholz, VV Mehta, US Alaan, et al. Interfacial ferromagnetism in lanio 3/camno 3 superlattices. *Physical review letters*, 111(8):087202, 2013.

[130] Joseph G Checkelsky, Jianting Ye, Yoshinori Onose, Yoshihiro Iwasa, and Yoshinori Tokura. Dirac-fermion-mediated ferromagnetism in a topological insulator. *Nature Physics*, 8(10):729, 2012.

[131] Yasuyuki Nakajima, Paul Syers, Xiangfeng Wang, Renxiong Wang, and Johnpierre Paglione. One-dimensional edge state transport in a topological kondo insulator. *Nat Phys*, 12(3):213–217, Mar 2016. Letter.

[132] JG Checkelsky, Minhyea Lee, E Morosan, RJ Cava, and NP Ong. Anomalous hall effect and magnetoresistance in the layered ferromagnet fe 1/ 4 ta s 2: The inelastic regime. *Physical Review B*, 77(1):014433, 2008.

[133] Zuocheng Zhang, Xiao Feng, Minghua Guo, Kang Li, Jinsong Zhang, Yunbo Ou, Yang Feng, Lili Wang, Xi Chen, Ke He, et al. Electrically tuned magnetic order and magnetoresistance in a topological insulator. *Nature Communications*, 5, 2014.

[134] Jiun-Haw Chu, Scott Riggs, Maxwell Shapiro, Jian Liu, Claudy Ryan Serero, Di Yi, M Melissa, SJ Suresha, C Frontera, Ashvin Vishwanath, Xavi Marti, IR Fisher, and R Ramesh. Linear magnetoresistance and time reversal symmetry breaking of pyrochlore iridates bi _2 ir _2 o _7. *arXiv preprint arXiv:1309.4750*, 2013.

[135] Junwoo Son, Pouya Moetakef, James M LeBeau, Daniel Ouellette, Leon Balents, S James Allen, and Susanne Stemmer. Low-dimensional mott material: Transport in ultrathin epitaxial lanio 3 films. *Applied Physics Letters*, 96(6):062114, 2010.

[136] Jian Liu, Mehdi Kargarian, Mikhail Kareev, Ben Gray, Phil J Ryan, Alejandro Cruz, Nadeem Tahir, Yi-De Chuang, Jinghua Guo, James M Rondinelli, et al. Heterointerface engineered electronic and magnetic phases of ndnio3 thin films. *Nature communications*, 4:2714, 2013.

[137] Raoul Scherwitzl, Stefano Gariglio, M Gabay, Pavlo Zubko, M Gibert, and J-M Triscone. Metal-insulator transition in ultrathin lanio 3 films. *Physical Review Letters*, 106(24):246403, 2011.

[138] Ji Zhang, Wei-Jing Ji, Jie Xu, Xiao-Yu Geng, Jian Zhou, Zheng-Bin Gu, Shu-Hua Yao, and Shan-Tao Zhang. Giant positive magnetoresistance in half-metallic double-perovskite sr2crwo6 thin films. *Science advances*, 3(11):e1701473, 2017.

[139] PK Rout, I Agireen, E Maniv, M Goldstein, and Y Dagan. Six-fold crystalline anisotropic magnetoresistance in the (111) laalo 3/srtio 3 oxide interface. *Physical Review B*, 95(24):241107, 2017.

[140] A Gerber, I Kishon, I Ya Korenblit, O Riss, A Segal, M Karpovski, and B Raquet. Linear positive magnetoresistance and quantum interference in ferromagnetic metals. *Physical review letters*, 99(2):027201, 2007.

[141] Jiun-Haw Chu, James G Analytis, David Press, Kristiaan De Greve, Thaddeus D Ladd, Yoshihisa Yamamoto, and Ian R Fisher. In-plane electronic anisotropy in underdoped ba (fe 1- x co x) 2 as 2 revealed by partial detwinning in a magnetic field. *Physical Review B*, 81(21):214502, 2010.

[142] Y Xiao, Y Su, S Nandi, S Price, B Schmitz, CMN Kumar, R Mittal, T Chatterji, N Kumar, SK Dhar, A Thamizhavel, and Th Brückel. Anomalous in-plane magnetoresistance in a eufe 2 as 2 single crystal: Evidence of strong spin-charge-lattice coupling. *Physical Review B*, 85(9):094504, 2012.

[143] Youguo Shi, Yanfeng Guo, Xia Wang, Andrew J Princep, Dmitry Khalyavin, Pascal Manuel, Yuichi Michiue, Akira Sato, Kenji Tsuda, Shan Yu, Masao Arai, Yuichi Shirako, Masaki Akaogi, nanlin Wang, Kazunari Yamaura, and Andrew T. Boothroyd. A ferroelectric-like structural transition in a metal. *Nature materials*, 12(11):1024–1027, 2013.

[144] Liang Fu. Parity-breaking phases of spin-orbit-coupled metals with gyrotropic, ferroelectric, and multipolar orders. *Physical review letters*, 115(2):026401, 2015.

[145] Philip W Anderson. Resonating valence bonds: A new kind of insulator? *Materials Research Bulletin*, 8(2):153–160, 1973.

[146] Philip W Anderson. The resonating valence bond state in La_2CuO_4 and superconductivity. *science*, 235(4793):1196–1198, 1987.

[147] Leon Balents. Spin liquids in frustrated magnets. *Nature*, 464(7286):199, 2010.

[148] Matthew P Shores, Emily A Nytko, Bart M Bartlett, and Daniel G Nocera. A structurally perfect S= 1/2 kagome antiferromagnet. *Journal of the american chemical society*, 127(39):13462–13463, 2005.

[149] JS Helton, K Matan, MP Shores, EA Nytko, BM Bartlett, Y Yoshida, Y Takano, A Suslov, Y Qiu, J-H Chung, et al. Spin dynamics of the spin-1/2 kagome lattice antiferromagnet $ZnCu_3(OH)_6Cl_2$. *Physical review letters*, 98(10):107204, 2007.

[150] P Mendels, F Bert, MA De Vries, A Olariu, A Harrison, F Duc, JC Trombe, JS Lord, A Amato, and C Baines. Quantum magnetism in the paratacamite family: towards an ideal kagomé lattice. *Physical review letters*, 98(7):077204, 2007.

[151] Tian-Heng Han, Joel S Helton, Shaoyan Chu, Daniel G Nocera, Jose A Rodriguez-Rivera, Collin Broholm, and Young S Lee. Fractionalized excitations in the spin-liquid state of a kagome-lattice antiferromagnet. *Nature*, 492(7429):406, 2012.

[152] TH Han, Joel S Helton, Shaoyan Chu, Andrea Prodi, Deepak K Singh, Claudio Mazzoli, Peter Müller, Daniel G Nocera, and Young S Lee. Synthesis and characterization of single crystals of the spin-1 2 kagome-lattice antiferromagnets $Zn_xCu_{4-x}(OH)_6Cl_2$. *Physical Review B*, 83(10):100402, 2011.

[153] A Zorko, S Nellutla, J Van Tol, LC Brunel, F Bert, F Duc, J-C Trombe, MA De Vries, A Harrison, and P Mendels. Dzyaloshinsky-Moriya anisotropy in the spin-1/2 kagome compound $ZnCu_3(OH)_6Cl_2$. *Physical review letters*, 101(2):026405, 2008.

[154] M Hanawa, Y Muraoka, T Tayama, T Sakakibara, J Yamaura, and Z Hiroi. Superconductivity at 1 k in cd 2 re 2 o 7. *Physical Review Letters*, 87(18):187001, 2001.

[155] Zenji Hiroi, Jun-Ichi Yamaura, Yuji Muraoka, and Masafumi Hanawa. Second phase transition in pyrochlore oxide cd2re2o7. *Journal of the Physical Society of Japan*, 71(7):1634–1636, 2002.

[156] JW Harter, ZY Zhao, J-Q Yan, DG Mandrus, and D Hsieh. A parity-breaking electronic nematic phase transition in the spin-orbit coupled metal cd2re2o7. *Science*, 356(6335):295–299, 2017.

[157] S Ghannadzadeh, M Coak, I Franke, PA Goddard, J Singleton, and Jamie L Manson. Measurement of magnetic susceptibility in pulsed magnetic fields using a proximity detector oscillator. *Review of Scientific Instruments*, 82(11):113902, 2011.